AGH Faculty of Electrical Engineering, Automatics, Computer Science and Biomedical Engineering

Doctoral thesis

Nanosatellite attitude estimation

Paweł Zagórski

Supervisor:
prof. dr hab. inż. Wojciech Grega

Kraków, 14th Jan, 2017

Acknowledgements

There are many people, without whom, it would not be possible for me to complete the work on the following dissertation. Listing all of them is very difficult, but, I would like to give my special thanks to:

- My parents and brother, who were a source of constant help and encouragement.
- The supervisor of this thesis, prof. dr hab. inż. Wojciech Grega for his guidance in both the scientific and procedural matters. For his patience towards me, and for the suggestions and corrections he made after reading the drafts.
- My co-workers, especially Tomasz Dziwiński and dr. Andrzej Tutaj for countless hours of enriching discussions and enormous amount of time and dedication they spent on helping me with the simulation studies.
- The supervisor of my master thesis, dr Paweł Piątek who was there when my interest in this research subject was born. Without his support, I would not even thought of starting this work.
- The employees of the Space Research Centre of the Polish Academy of Sciences, especially dr. Karol Seweryn, dr. Roman Wawrzaszek and Grzegorz Juchnikowski. For their vast experience they shared with me during our meetings.
- My dear friends who supported me every step of the way.

Streszczenie

Niniejsza rozprawa doktorska ma na celu weryfikację następujących hipotez naukowych:

1. Możliwe jest opracowanie estymatora orientacji przestrzennej dedykowanego dla nanosatelitów, który może funkcjonować z wykorzystaniem niewielkiej liczby stosunkowo prostych czujników, bez wiedzy o momentach siły działających na satelitę.
2. Możliwe jest opracowanie obserwatora orientacji który radzi sobie z okresową niedostępnością pomiarów jednego z czujników orientacji.
3. Możliwe jest uzyskanie porównywalnego stopnia precyzji estymacji orientacji przestrzennej za pomocą systemu, który dokonuje każdego rodzaju pomiarów z inną częstotliwością, tak, by móc rzadziej używać bardziej energochłonnych czujników.

Prezentowana praca rozpoczyna się krótkim wprowadzeniem do niektórych pojęć z dziedziny inżynierii kosmicznej, które są istotne dla tematu, ale wykraczają poza sferę samej teorii sterowania. Należą do nich układy odniesienia, sposób pomiaru czasu i opisywania orbit i orientacji statków kosmicznych.
Następnie zostaje wprowadzony termin "nanosatelita". Problem kontroli orientacji dla tej klasy pojazdów kosmicznych przedstawiono wymieniając podstawowe zadania sterowania i krótko opisując najważniejsze części Systemu Odtwarzania i Kontroli Orientacji. Aby dać czytelnikowi dobry kontekst praca zawiera również przegląd literatury, wraz z opisem istniejących już rozwiązań służących do estymacji orientacji.
Każdy algorytm odtwarzania orientacji wymaga modeli referencyjnych mierzonych wartości wektorowych. W związku z tym praca zawiera również opis tych modeli. Oprócz pomiaru prędkości kątowej, w symulacjach brane są pod uwagę pomiary pola magnetycznego i kierunku Słońca.
Następnie opisany zostaje nowy algorytm SDQAE, zarówno w uogólnionej formie, jak i dla konkretnego przypadku trzech wybranych typów pomiarów. Estymator działa rozwiązując klasyczny problem Wahby w wersji z kwaternionową reprezentacją orientacji. Algorytm działa w oparciu o poszukiwanie minimum funkcji celu za pomocą metody najszybszego spadku. Jednak celem nie jest znalezienie optymalnego rozwiązania w każdym kroku, co byłoby podatne na błędy pomiarowe. Przeciwnie, wykorzystuje schemat predykcji i korekcji gdzie żyroskop MEMS dostarcza sposobu przewidywania orientacji, a pozostałe czujniki stanowią wejścia do bloku korekcji wykonującego jeden krok optymalizacji w jednym takcie. Jednocześnie SDQAE ma zdolność szacowania biasu żyroskopu. Algorytm posiada również dość rzadką cechę, ponieważ może pracować z różnymi częstotliwościami próbkowania dla każdego z czujników. Potencjalnie umożliwia to równoważenie zużycia energii i wydajności w bardziej wyrafinowany sposób. Praca zawiera także uwagi dotyczące strojenia algorytmu i właściwości jego zbieżności.
Istnieją trzy typy symulacji weryfikacyjnych przeprowadzonych w ramach prezentowanej pracy. Przede wszystkim estymator SDQAE jest testowany w realistycznym scenariuszu planowanej misji satelity Lithuanica Sat-2. Obejmuje on eksperyment Monte Carlo nieuwzględniający okresową niedostępność czujnika kierunku słońca ze względu na jego ograniczone pole widzenia (FOV) oraz fakt, że Słońce może zostać zaćmione przez Ziemię. Takie realistyczne badania nie są powszechne w literaturze przedmiotu. Ponadto, przeprowadzone zostało porównanie algorytmu z wybranymi znanymi rozwiązaniami. Eksperyment Monte Carlo jest w tym przypadku podobny, choć z uwagi na ograniczenia niektórych algorytmów zakłada pełne pole widzenia (FOV) czujników Słońca. Okazuje się, że przedstawiony estymator wypada bardzo dobrze w tym zestawieniu, a w szczególności wydaje się wyjątkowo odporny na zjawisko zaćmienia Słońca. Ostatni pracy przedstawiony scenariusz to taki, w którym SDQAE używa wszystkich czujników z różnymi okresami próbkowania. Okazuje się, że można w takim przypadku uzyskać porównywalną jakość estymacji.
Konkludując, udało się wykazać, że wszystkie trzy przedstawione hipotezy badawcze okazują się być prawdziwe. Dodatkowo, praca doktorska kończy się wskazaniem niektórych możliwych kierunków przyszłych badań.

Abstract

The doctoral thesis aims at verifying the following hypothesis:

1. It is possible to develop an attitude estimator dedicated for nanosatellites, which is able to function with small number of relatively simple attitude sensors without the knowledge of torques acting on the satellite.
2. It is possible to develop a single attitude estimator that is able to dynamically cope with periodic unavailability of the measurements from one of the attitude sensors.
3. It is possible to achieve comparable levels of precision of attitude estimation with a systems that samples each of the sensors at different rate to use the more energy consuming sensors less frequently.

The presented work begins with a short introduction to some aerospace science concepts that are essential for the subject matter, but lie outside the realm of control theory itself. Those include reference frames, way of measuring time and describing the orbits and attitude of spacecraft.
Afterwards, the term 'nanosatellite' is introduced and explained. Attitude control problem for this class of spacecraft is outlined by listing the basic control tasks and briefly describing the most important parts of the Attitude Determination and Control System (ADCS). To give a good background a literature review is given, and the existing solutions for satellite attitude estimation are outlined.
As any determination algorithm requires reference models of the measured attitude vectors, reference models used in further studies are described. Apart form a rate measurement, the magnetic field measurement and Sun direction measurement are base for the following simulations.
Next, the novel Steepest Descent Quaternion Attitude Estimator (SDQAE) is described, both in a generalized form, and for the particular case of three selected measurement types. Estimator aims at solving the classically defined Wahba attitude determination problem translated to quaternion reprezentation. However, the aim is not to find the optimal solution at each step, which is prone to the sensor measurement errors being represented in the solution. Rather, it uses a prediction-correction scheme where the MEMS gyroscope provides a way of predicting the attitude, and the remaining sensors constitute inputs to the correction terms. At the same time SDQAE possess the ability to estimate gyroscope bias. It is also unique, because it can work with different sampling rates for each of the sensors, which potentially enables balancing the performance and energy consumption in a more sophisticated way. Work also contains remarks on algorithm tuning and its convergence properties.
There are three types of verification simulations conducted as part of the work. First of all the SDQAE estimator is tested in a realistic scenario of a planned Lithuanica Sat-2 satellite. This includes Monte Carlo study taking into account periodical sensor unavailability due to the limited Field Of View (FOV) of the Sun sensors and the fact that Sun may be eclipsed by the Earth. Such realistic studies are not common in the literature of the subject. Furthermore, the algorithm is compared with other known estimators. Implemented observers are ran as part of another Monte Carlos study, this time assuming unlimited FOV of the Lithuanica Sat-2 Sun sensors. It turns out that the presented estimator compares very well with its counterparts, proving especially resilient to the Sun eclipsing phenomenon. The last study presents the scenario where SDQAE samples each of the sensors at different rates, proving that it can still provide comparable attitude estimation precision.
In the conclusion, all working hypothesis turn out to be true. Additionally, doctoral thesis ends with pointing at some possible directions of future research.

Contents

List of Figures

List of Tables

Glossary

albedo

The albedo of a surface is the ratio of radiation reflected from the surface to the incident radiation.

antumbra

Region from which an occulting body appears entirely contained within the disc of the light source.

aphelion

Point in the elliptical orbit of a planet where it is farthest from the Sun.

apoapsis

Point of a body's elliptical orbit about the system's centre of mass where the distance between the body and the centre of mass is at its maximum.

apogee

Point, in an orbit about the Earth, that is furthest from the Earth: the apoapsis of an Earth orbiter.

ascending node

For geocentric and heliocentric orbits, the ascending node (or north node) is where the orbiting object moves north through the plane of reference.

descending node

For geocentric and heliocentric orbits, the desending node (or south node) is where the orbiting object moves south through the plane of reference.

detumbling

When satellite leaves the launch vehicle in space it often has some initial angular rate. Often, the first phase of attitude control system operation employs a simple alorigthm to decrease this rate in a process called detumbling.

directon cosine matrix

One of the way of describing rotation in 3D space (and therefore orientation).

escape velocity

Escape velocity is the minimum speed needed for an object to escape from the gravitational attraction of a massive body, without the aid of thrust, or suffering the resistance from friction.

Euler angle

The Euler angles are three angles introduced by Leonhard Euler to describe the orientation of a rigid body with respect to a fixed coordinate system.

extrinsic rotation

Extrinsic rotations are defined about the axes xyz of the original coordinate system, which is assumed to remain motionless.

geocentric orbit

A geocentric orbit or Earth orbit involves any object orbiting the Earth, such as the Moon or artificial satellites.

gimbal lock

Gimbal lock is the loss of one degree of freedom in a three-dimensional, three-gimbal mechanism that occurs when the axes of two of the three gimbals are driven into a parallel configuration, "locking" the system into rotation in a degenerate two-dimensional space.

heliocentric orbit

A heliocentric orbit (also called circumsolar orbit) is an orbit around the barycenter of the Solar System, which is usually located within or very near the surface of the Sun.

intrinsic rotation

Intrinsic rotations are defined about the axes of the rotating coordinate system XYZ, solidary with the moving body, which changes its orientation after each elemental rotation.

leap second

A leap second is a one-second adjustment that is occasionally applied to Coordinated Universal Time (UTC) in order to keep its time of day close to the mean solar time, or UT1.

leap year

A leap year (also known as an intercalary year or a bissextile year) is a year containing one additional day (or, in the case of lunisolar calendars, a month) added to keep the calendar year synchronized with the astronomical or seasonal year.

line of apsides

An apse line, or line of apsides, is an imaginary line defined by an orbit's eccentricity vector. It is strictly defined for elliptic, parabolic, and hyperbolic orbits. For elliptical orbits it connects the orbit's periapsis and apoapsis.

line of nodes

The line of nodes is the intersection of the object's orbital plane with the plane of reference. It passes through the two nodes (ascending and descending).

meridian

Imaginary circle in a plane perpendicular to the planes of the celestial equator and horizon.

nadir

At a given point nadir is the local vertical direction pointing in the direction of the force of gravity at that location.

parallax

Parallax is a displacement or difference in the apparent position of an object viewed along two different lines of sight, and is measured by the angle or semi-angle of inclination between those two lines.

penumbra

The penumbra (from the Latin paene "almost, nearly") is the region in which only a portion of the light source is obscured by the occluding body. An observer in the penumbra experiences a partial eclipse.

periapsis

Point of a body's elliptical orbit about the system's centre of mass where the distance between the body and the centre of mass is at its minimum.

perigee

Point, in an orbit about the Earth, that is closest to the Earth: the periapsis of an Earth orbiter.

perihelion

Point in the elliptical orbit of a planet or comet etc. where it is nearest to the Sun.

prime meridian

A prime meridian is a meridian (a line of longitude) in a geographical coordinate system at which longitude is defined to be 0°.

sidereal day

A mean sidereal day is 23 hours, 56 minutes, 4.0916 seconds (23.9344699 hours or 0.99726958 mean solar days), the time it takes Earth to make one rotation relative to the vernal equinox.

sidereal time

Sidereal time is a time-keeping system that astronomers use to locate celestial objects.

solar time

Solar time is a calculation of the passage of time based on the Sun's position in the sky. The fundamental unit of solar time is the day.

Tait-Bryan angles

Tait–Bryan angles are also called Cardan angles; nautical angles; heading, elevation, and bank; or yaw, pitch, and roll. Sometimes, both kinds of sequences are called "Euler angles". In that case, the sequences of the first group are called proper or classic Euler angles.

umbra

The umbra (Latin for "shadow") is the innermost and darkest part of a shadow, where the light source is completely blocked by the occluding body.

Vernal equinox

Vernal equinox is the equinox on the Earth when the Sun appears to leave the southern hemisphere and cross the celestial equator, heading northward as seen from Earth.

List of Symbols

B	attitude profile matrix
C_d	drag coefficient
E_{rot}	kinetic energy of the rotational motion
F	EKF state transition matrix
G_{lp}	Low pass filter transfer function
G	gravitational constant $(6.673\,84(80) \times 10^{-11}\,\mathrm{N\,m^2\,kg^{-2}})$
I	identity matrix
K_ω	SDQAE algorithm bias estimation gain
K_d	B-dot detumbler constant gain
K_{ref}	magnetometer gain matrix at reference temperature
K_{temp}	magnetometer gain temperature coefficient matrix
K	EKF Kalman gain matrix
K	magnetometer gain matrix
K	SDQAE algorithm gain
L_m	objective function of the magnetometer calibration problem
M_E	mass of the Earth $(5.972\,19 \times 10^{24}\,\mathrm{kg})$
M	magnetometer sensor axis misalignment matrix
P	EKF covariance estimate matrix
Q	direction cosine matrix
Q	EKF process noise covariance matrix
R_E	mean radius of the Earth $(6\,371\,009\,\mathrm{km})$
R_S	mean radius of the Sun $(6.96 \times 10^8\,\mathrm{m})$
R	EKF sensor noise covariance matrix
S_0	solar radiation flux density
V	scalar potential of the magnetic field
Γ	angle between the the magnetic vector and satellite velocity vector
Ω	longitude of ascending node
Φ	Euler principal angle
Θ	co-latitude
α_p	vertex semiangle of the penumbra cone in Sun-Earth system (0.264°)
α	precession angle
β_S	Sun beta angle
β_u	vertex semiangle of the umbra cone in Sun-Earth system (0.269°)
β	nutation angle
γ	spin angle
λ	longitude positive East
I	inertia matrix

μ	Lagrange multiplier
ν_m	mean anomaly
ν_t	true anomaly
ω	argument of periapsis
ψ	yaw angle
ρ	atmospheric density
τ	scalar value of external disturbances torque
$\mathtt{t}_{ref}$	reference temperature
$\mathtt{t}_{sens}$	sensor temperature
θ	pitch angle
φ	roll angle
$\boldsymbol{S}$	solar radiation incidence vector
$\hat{\boldsymbol{x}}$	EKF state estimate vector
$\boldsymbol{\tau_a}$	aerodynamic drag torque vector
$\boldsymbol{\tau_g}$	gravity gradient torque vector
$\boldsymbol{\tau_m}$	magnetic torque vector
$\boldsymbol{a}$	Euler axis
$\boldsymbol{b}_{ref}$	magnetometer sensor bias vector at reference temperature
$\boldsymbol{b}_{temp}$	magnetometer sensor bias temperature coefficient vector
$\boldsymbol{b}$	magnetometer sensor bias vector
$\boldsymbol{f_a}$	atmospheric drag force
$\boldsymbol{r_E}$	Earth position vector (origin point in the Sun centre)
$\boldsymbol{r_s}$	satellite position vector (origin point in the Earth centre)
$\boldsymbol{v_s}$	vector of the velocity of the satellite
$\boldsymbol{x}$	EKF state vector
$\boldsymbol{z}$	EKF measurement vector vector
$\boldsymbol{l_{cm,cp}}$	vector from centre of mass to center of atmospheric pressure
$\boldsymbol{l_{cm,cr}}$	vector from centre of mass to center of radiation pressure
a	semimajor axis of the orbit elipse
c	speed of light $299\,792\,458\,\mathrm{m\,s^{-1}}$
e	orbit eccentricity, describes shape of the orbit ellipse
i	orbital inclination
m_{ref}	magnetometer sensor axis misalignment matrix
m	mass of the satellite
r_E	distance between the Sun and the Earth
r_s	satellite distance from the Earth centre
t_0	epoch, initial time used as a reference for determining satellite position
t_{jd}	julian day
t_{mc0}	epoch of Meeus Sun model expressed in Julian days, equals $2\,451\,545.0$
t_{mc}	number of centuries since Meeus Sun model epoch
v_s	scalar value of the velocity of the satellite
$\delta\eta_{MC}$	mean angule of attack error between all runs of Monte Carlo study
$\delta_i^b\hat{q}$	multiplicative quaternion error of the attitude estimate
$\delta\theta_{MC}$	mean angular error between all runs of Monte Carlo study
$\delta\theta_{RMS}$	Root Mean Square error of the attitude estimation
$\delta\theta$	angular error of the attitude estimate
$\mathcal{F}_b$	BCF reference frame
$\mathcal{F}_e$	EOD reference frame

$\mathcal{F}_f$	ECF reference frame
$\mathcal{F}_i$	ECI reference frame
$\mathcal{F}_n$	NED reference frame
$\mathcal{F}_o$	OF reference frame
c_m	SDQAE weight coefficient for the magnetic correction term
c_s	SDQAE weight coefficient for the Sun vector correction term
${}^b\omega$	scalar value of angular rate in BCF frame
${}^b\dot{\boldsymbol{\omega}}_{\boldsymbol{B}}$	angular rate bias time derivative in BCF frame
${}^b\hat{\boldsymbol{\omega}}_{\boldsymbol{B}}$	angular rate bias estimate in BCF frame
${}^b\boldsymbol{\omega}_{\boldsymbol{B}}$	angular rate bias in BCF frame
${}^b\boldsymbol{\omega}$	angular rate vector in BCF frame
${}^b\boldsymbol{\omega}$	angular velocity of a spacecraft measured in BCF frame
${}^b\overline{\boldsymbol{\omega}}_{\boldsymbol{B}}$	angular rate bias in BCF frame (extended to quaternion)
${}^b\overline{\boldsymbol{\omega}}$	angular rate vector in BCF frame (extended to quaternion)
${}^b\overline{\boldsymbol{s}}$	measured Sun vector in BCF frame (extended to quaternion)
${}^b\widehat{\boldsymbol{\omega}}_{\boldsymbol{B}}$	angular rate bias estimate in BCF frame (extended to quaternion)
${}^b\widehat{\boldsymbol{\omega}}_{\boldsymbol{E}}$	angular rate estimation error in BCF frame (extended to quaternion)
${}^b\widehat{\boldsymbol{\omega}}$	angular rate estimate in BCF frame (extended to quaternion)
${}^b\boldsymbol{s}$	measured Sun vector in BCF frame
${}^i\boldsymbol{m}$	modelled magnetic field vector in ECI frame
${}^i\overline{\boldsymbol{s}}$	modelled Sun vector in ECI frame (extended to quaternion)
${}^i\boldsymbol{s}$	modelled Sun vector in ECI frame
${}^b\boldsymbol{B}$	magnetic B vector expressed in BCF reference frame
${}^b\boldsymbol{\mu}$	magnetic dipole moment in BCF reference frame
${}^b\overline{\boldsymbol{m}}$	measured magnetic field vector in BCF frame (extended to quaternion)
${}^b\boldsymbol{\tau_c}$	attitude control torque
${}^b\boldsymbol{m}$	measured magnetic field vector in BCF frame
${}^b_i\hat{q}$	estimated orientation quaternion
${}^b_i\overline{q}$	attitude quaternion
${}^f\boldsymbol{B}$	magnetic B vector expressed in ECF reference frame
${}^i\boldsymbol{B}$	magnetic B vector expressed in ECI reference frame
${}^i\overline{\boldsymbol{m}}$	modelled magnetic field vector in ECI frame (extended to quaternion)
${}^i_bA$	attitude matrix
${}^s\boldsymbol{m}$	raw sensor measurement of the magnetic field vector
${}^\perp\boldsymbol{B}$	magnetic B vector expressed in NED reference frame

List of Acronyms

AB	Aerospace Blockset
ACS	Automatic Control System
AEKF	Additive Extended Kalman Filter
AMR	Anizotropic MagnetoResitive
BCF	Body-Centred Reference Frame
BSEKF	Backward-Smoothing Extended Kalman Filter
CCD	Charge Coupled Device
CMOS	Complementary Metal Oxide Semiconductor
CSLI	CubeSat Launch Initiative
DCM	Direction Cosine Matrix
ECF	Earth-Centred, Earth-Fixed
ECI	Earth-Centred, Earth-Inertial
ECSS	European Cooperation for Space Standardization
EKF	Extended Kalman Filter
EOD	Ecliptic of the Date
EQUEST	Extended QUaternion ESTimator
ESOQ	EStimator of Optimal Quaternion
ESOQ2	second EStimator of Optimal Quaternion
FFT	Fast Fourier Transform
FOAM	Fast Optimal Attitude Matrix
FOG	Fiber Optic Gyro
GEO	Geostationary Earth's orbit
GNSS	Global Navigation Satellite System
GPS	Global Positioning System
IAGA	International Association of Geomagnetism and Aeronomy
IGRF	International Geomagnetic Reference Field model
ISS	International Space Station

JD	Julian Day
LEO	Low Earth's orbit
LQR	Linear Quadratic Regulator
MEKF	Multiplicative Extended Kalman Filter
MEMS	Micro Electro-Mechanical System
MKF	Matrix Kalman Filter
MSISE	Mass Spectrometer - Incoherent Scatter
NASA	National Aeronautics and Space Administration
NED	North-East-Down
OPREQ	OPtimal REQuest
QUEST	QUaternion ESTimator
REQUEST	REcursive QUaternion ESTimator
RLG	Ring Laser Gyro
RMS	Root Mean Square error
SDQAE	Steepest Descent Quaternion Attitude Estimator
SVD	Singular Value Decomposition
TRIAD	TRIaxial Attitude Determination
ULS	Unconstrained Least-Squares
UT	Universal Time

Chapter 1

Problem statement and main thesis

This chapter introduces the scientific problem under consideration. Sec. 1.1 of this chapter contains its short description Main thesis are given in Sec. 1.2. To help the reader a structure of the following document is outlined in Sec. 1.3.

1.1 Problem statement

In recent years more and more small satellites are reaching the orbit. Their design poses a significant challenge due to severe mass, volume, electrical power and budgetary constraints. Very often it is necessary to achieve attitude determination of such satellites while utilizing very simple, off-the-shelf sensors instead of complex attitude determination devices such as star trackers. Many attitude estimation algorithms exist, but the author believes that nanosatellite platforms require a modified approach. In this thesis an algorithm for attitude estimation is proposed. The assumption is made that only the angular rate, magnetometer and Sun sensors are used for attitude estimation. A dedicated simulation environment is developed in which effects such as unavailability of the data (for example due to the eclipse condition), limited field of view of the Sun sensors and partial unobservability due to the measured vectors being close to collinear is taken into account during the performed studies. They call for a simple, computationally efficient scheme that is robust enough to cope with all the unfavourable conditions. The new attitude estimator is not only tested for a newly designed Lithuanica SAT-2 case, but also compared to the existing solutions.

1.2 Main thesis

The main thesis of this work can be summarised as follows:

1. It is possible to develop an attitude estimator dedicated for nanosatellites, which is

able to function with small number of relatively simple attitude sensors without the knowledge of torques acting on the satellite.

2. It is possible to develop a single attitude estimator that is able to dynamically cope with periodic unavailability of the measurements from one of the attitude sensors.

3. It is possible to achieve comparable levels of precision of attitude estimation with a systems that samples each of the sensors at different rate to use the more energy consuming sensors less frequently.

1.3 Thesis structure

The structure of this thesis is as follows.

In Ch. 2 a brief introduction is given on several topics regarding the satellite movement. Reference frames used in spacecraft engineering are described in Sec. 2.1 and the typical way of measuring time is outlined in Sec. 2.2. Orbital elements used to describe satellite orbits are briefly outlined in Sec. 2.3. Finally, classical ways of parametrically describing satellite attitude are mentioned in Sec. 2.4.

Ch. 3 describes the satellite attitude control problems. Sec. 3.1 describes the nanosatellite segment and outlines how it differs from traditional 'big satellite' approach. In the next section the essential constituents of attitude control systems are described including its basic tasks, sources of disturbances, classification of actuators and sensors, outline of attitude dynamics and introduction to the classical formulation of attitude estimation problem. Finally, state of the art in attitude estimation is given in Sec. 3.3.

Reference models used in further simulations are given in Ch. 4.

Ch. 5 describes the proposed Steepest Descent Quaternion Attitude Estimator (SDQAE) attitude estimator in a generalized form, and provides a case study of a small nanosatellite with three types of vector sensors (angular rate, magnetic field and the Sun vector). Remarks on estimator tuning and convergence properties are given as well.

Proposed estimator structure is then tested and results are given in Ch. 6 with the best and worst case scenario Monte-Carlo study for Lithuanica SAT-2 satellite. Further in the chapter the selected attitude estimators known from the literature are compared against the SDQAE, and a multi-rate scheme for the proposed solution is given.

Finally, Ch. 7 contains the summary of the thesis and points at some possible subjects for further study.

Chapter 2

Parametrization of the satellite orbit and orientation

In this chapter a basic background information on the ways of describing satellite position and orientation are given. Essential reference frames are explained in Sec. 2.1. Sec. 2.2 contains information on sidereal time, which is commonly used as a time measure in astronomical and aerospace applications. Parametrization of the orbit shape, size and position of the satellite is given in Sec. 2.3. Most of this information is based on a monograph [18]. Additionally, short outline of common spacecraft attitude representations together with required algebra and conventions are presented in Sec. 2.4 according to [69].

2.1 Reference frames

The reference frames useful for describing spacecraft motion are generally composed of a triad of orthonormal (orthogonal and of unit length) base vectors. If we label those vectors $\hat{\boldsymbol{i}}$, $\hat{\boldsymbol{j}}$ and $\hat{\boldsymbol{k}}$ the reference frame can be represented in form of a matrix:

$$\mathcal{F} \equiv \begin{bmatrix} \hat{\boldsymbol{i}} \\ \hat{\boldsymbol{j}} \\ \hat{\boldsymbol{k}} \end{bmatrix}. \tag{2.1}$$

Notice that this is not conventional matrix, as it is composed of vectors. This type of matrices is called vectrices and its properties are described in [28]. Only dextral (i.e. right-handed, where $\hat{\boldsymbol{i}} \times \hat{\boldsymbol{j}} = \hat{\boldsymbol{k}}$) reference frames will be used in this thesis.

Let us now consider a vector $\vec{v}$ in Euclidean space, label by $\mathcal{F}_a$ a reference frame consisting of base vectors $\hat{\boldsymbol{i}}_{\boldsymbol{a}}$, $\hat{\boldsymbol{j}}_{\boldsymbol{a}}$ and $\hat{\boldsymbol{k}}_{\boldsymbol{a}}$, and denote by c_1, c_2 and c_3 the direction cosines of $\vec{v}$ with respect to reference frame $\mathcal{F}_a$. Then, we can write:

$$\vec{v} = v(c_1\hat{\boldsymbol{i}}_{\boldsymbol{a}} + c_2\hat{\boldsymbol{j}}_{\boldsymbol{a}} + c_3\hat{\boldsymbol{k}}_{\boldsymbol{a}}), \tag{2.2}$$

where v is the length of $\boldsymbol{v}$. Defining coordinates of the vector $\vec{v}$ in the reference frame $\mathcal{F}_a$:

$$v_i \equiv vc_i, \tag{2.3}$$

$$\boldsymbol{v} \equiv \begin{bmatrix} v_1 \\ v_2 \\ v_3 \end{bmatrix}, \tag{2.4}$$

we can formulate the alternative form:

$$\vec{v} = \boldsymbol{v}^T \mathcal{F}_a = \mathcal{F}_a^T \boldsymbol{v}. \tag{2.5}$$

It is also possible to write $\boldsymbol{v}$ in terms of $\vec{v}$ and $\mathcal{F}_a$:

$$\boldsymbol{v} = \mathcal{F}_a \cdot \vec{v} \equiv \vec{v} \cdot \mathcal{F}_a. \tag{2.6}$$

To summarize, each reference frame $\mathcal{F}_a$ can be represented in terms of a vectrice. This allows for compactly writing coordinates of any vector $\vec{v}$ with respect to any reference frame $\mathcal{F}_a$.

2.1.1 Earth-Centred, Earth-Fixed reference frame (ECF)

Earth-Centred, Earth-Fixed reference frame (ECF) is a Cartesian system. Centre of the frame coincides with the Earth's centre of mass. Axis of the frame will be denoted in the following way:

$$\mathcal{F}_f \equiv \begin{bmatrix} \hat{\boldsymbol{i}}_{\boldsymbol{f}} \\ \hat{\boldsymbol{j}}_{\boldsymbol{f}} \\ \hat{\boldsymbol{k}}_{\boldsymbol{f}} \end{bmatrix}, \tag{2.7}$$

where $\hat{\boldsymbol{k}}_{\boldsymbol{f}}$ axis is in the direction of Conventional International Origin, $\hat{\boldsymbol{i}}_{\boldsymbol{f}}$ is orthogonal to $\hat{\boldsymbol{k}}_{\boldsymbol{f}}$ an oriented in the direction to mean Greenwich meridian, and $\hat{\boldsymbol{j}}_{\boldsymbol{f}}$ completes the triad as shown in Fig. 2.1.

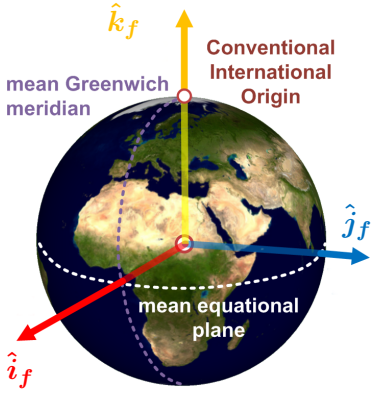

Figure 2.1: Earth-Centred, Earth-Fixed reference frame (source: wikimedia commons)

2.1.2 Earth-Centred, Earth-Inertial reference frame (ECI)

Earth-Centred, Earth-Inertial reference frame (ECI) origin is located in the centre of mass of the Earth. Unlike ECF the ECI frame does not rotate with the Earth, but is inertial

instead and points towards stationary stars. Coordinates are denoted as follows:

$$\mathcal{F}_i \equiv \begin{bmatrix} \hat{\boldsymbol{i}}_{\boldsymbol{i}} \\ \hat{\boldsymbol{j}}_{\boldsymbol{i}} \\ \hat{\boldsymbol{k}}_{\boldsymbol{i}} \end{bmatrix}, \tag{2.8}$$

where $\hat{\boldsymbol{i}}_{\boldsymbol{i}}$ axis points towards Vernal equinox[1], the $\hat{\boldsymbol{k}}_{\boldsymbol{i}}$ axis is Earth's rotation axis positive north, and $\hat{\boldsymbol{j}}_{\boldsymbol{i}}$ axis lies in the equatorial plane and completes the triad. This configuration is depicted in Fig. 2.2.

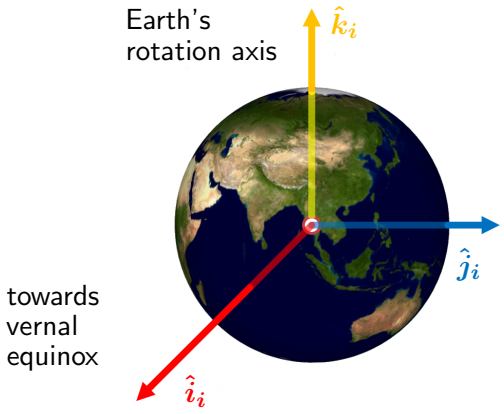

Figure 2.2: Earth-Centred, Earth-Inertial reference frame (source: wikimedia commons)

2.1.3 Body-Centred Reference Frame (BCF)

This reference frame is tied to a spacecraft itself. It is convenient for correlating vector measurements of the attitude sensors, because most often they do not change their position and orientation on board of the craft. Body-Centred Reference Frame (BCF) frame origin is defined as the centre of mass of the spacecraft. Three axis are defined as triad in the directions that are most natural for the particular spaceship where:

$$\mathcal{F}_b \equiv \begin{bmatrix} \hat{\boldsymbol{i}}_{\boldsymbol{b}} \\ \hat{\boldsymbol{j}}_{\boldsymbol{b}} \\ \hat{\boldsymbol{k}}_{\boldsymbol{b}} \end{bmatrix}. \tag{2.9}$$

Example of such a frame can be seen in Fig. 2.3.

[1]Vernal equinox is defined by the position of the Sun at time instant when the noontime Sun crosses the equator from South to the North. This happens only once a year, on one of two days when the number of hours of daylight and darkness is equal. On the second of those days other equinox occurs, when the Sun makes the opposite equator crossing. Currently the Vernal equinox lies in the constellation Pisces, which is visible in the night sky in the fall.

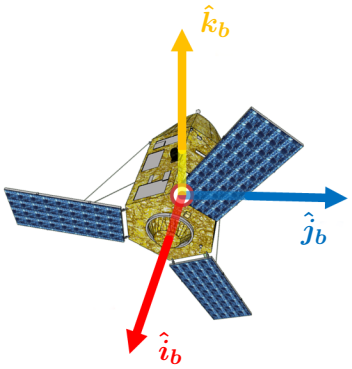

Figure 2.3: Body-Centred Reference Frame

2.1.4 Orbital Frame (OF)

Orbital reference frame is often called 'roll-pitch-yaw' frame. Origin of the frame is placed in the centre of mass of the spacecraft, similarly to BCF. However, directions:

$$\mathcal{F}_o \equiv \begin{bmatrix} \hat{\boldsymbol{i}}_{\boldsymbol{o}} \\ \hat{\boldsymbol{j}}_{\boldsymbol{o}} \\ \hat{\boldsymbol{k}}_{\boldsymbol{o}} \end{bmatrix}, \tag{2.10}$$

are defined in such a way, that $\hat{\boldsymbol{k}}_{\boldsymbol{o}}$ axis is in the nadir direction, pointing to mass centre of the Earth. Axis $\hat{\boldsymbol{j}}_{\boldsymbol{o}}$ is in the negative orbit normal direction, and $\hat{\boldsymbol{i}}_{\boldsymbol{o}}$ completes the triad. For circular orbits $\hat{\boldsymbol{i}}_{\boldsymbol{o}}$ is in the same direction as satellite velocity vector. Graphical depiction of this frame can be seen in Fig. 2.4.

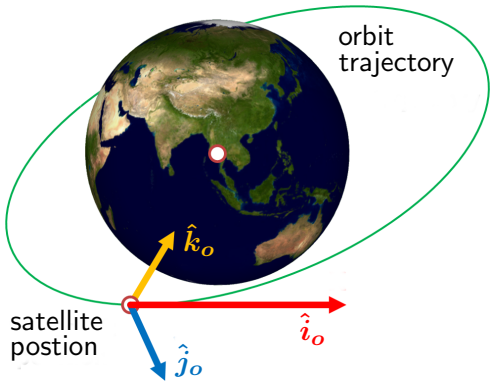

Figure 2.4: Orbital reference frame (source: wikimedia commons)

2.1.5 Ecliptic of the Date reference frame (EOD)

Ecliptic of the Date (EOD) reference frame has its origin at the barycentre of the solar system. Axes defined as

$$\mathcal{F}_e \equiv \begin{bmatrix} \hat{\boldsymbol{i}}_{\boldsymbol{e}} \\ \hat{\boldsymbol{j}}_{\boldsymbol{e}} \\ \hat{\boldsymbol{k}}_{\boldsymbol{e}} \end{bmatrix}, \tag{2.11}$$

are oriented as shown in Fig. 2.5. The $\hat{\boldsymbol{i}}_{\boldsymbol{e}}$ is directed towards the Vernal equinox, and together with $\hat{\boldsymbol{j}}_{\boldsymbol{e}}$ lies in the ecliptic plane. Last axis, $\hat{\boldsymbol{k}}_{\boldsymbol{e}}$ completes the right-handed Cartesian frame.

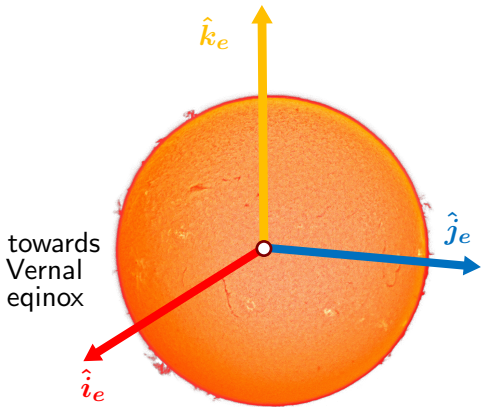

Figure 2.5: Ecliptic of the Date reference frame (source: wikimedia commons)

2.1.6 North-East-Down reference frame (NED)

The North-East-Down (NED) reference frame is defined differently in all the points in the vicinity of the Earth. It is used in geomagnetic field models, therefore it is always oriented the same way in relation to surface osculating the planet surface. The frame consists of three vectors, as noted in (2.12)

$$\mathcal{F}_n \equiv \begin{bmatrix} \hat{\boldsymbol{i}}_{\boldsymbol{n}} \\ \hat{\boldsymbol{j}}_{\boldsymbol{n}} \\ \hat{\boldsymbol{k}}_{\boldsymbol{n}} \end{bmatrix} . \tag{2.12}$$

For any point in space that is selected for the frame origin the $\hat{\boldsymbol{i}}_{\boldsymbol{n}}$ axis points in the direction from the South towards the North. The $\hat{\boldsymbol{k}}_{\boldsymbol{n}}$ axis points down in the direction of Earth centre. Axis $\hat{\boldsymbol{j}}_{\boldsymbol{n}}$ completes the Cartesian frame pointing along the east geographical direction, thus the frame name. Graphical depiction of the NED frame is shown in Fig. 2.6.

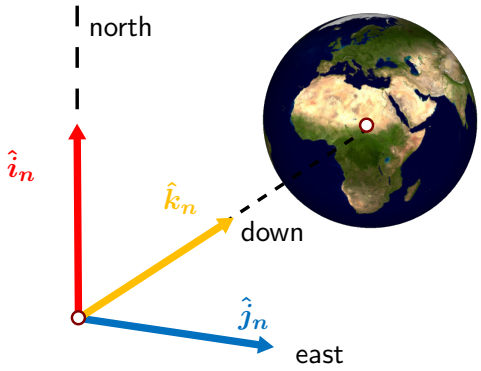

Figure 2.6: North-East-Down reference frame (source: wikimedia commons)

2.2 Sidereal time

To describe motion of a satellite around a central body it is essential to establish a way of measuring time. In everyday life we most often use solar time. It is dictated by the motion of the Sun across the sky. For one full 24-hour day to pass it is needed for the Sun to return to the same position overhead[2] as depicted in 2.7b and 2.7d. It is convenient, because it relates to night-day cycle which is the most important time cycle determining human activities. As solar time varies with longitude we also define time zones, in relation to Universal Time (UT) which is a solar time measured by the observer located on Prime meridian (terrestrial longitude equal to 0°).

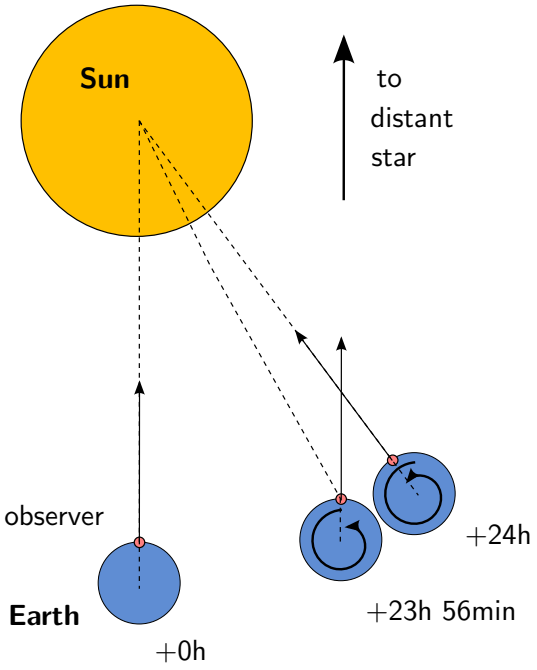

(a) Sidereal time and the Sun

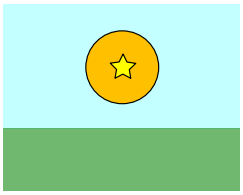

(b) View at +0h

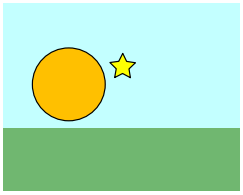

(c) View at +23h 56min

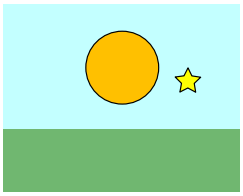

(d) View at +24h

Figure 2.7: Diagram explaining sidereal time

It is easy to imagine that such a time measure would not make sense for astronautical or astronomical applications. Although, for terrestrial observer, every day at the same time the Sun is visible at the same azimuth angle, it is not true for others stars. Day-night cycle comes mainly from the Earth spinning motion around its own axis, but the planet also revolves slowly around the Sun. Therefore, our star escapes a bit every day. Distant stars (all stars except for the Sun) are far enough from the Earth to assume that each of them is located at constant inertial direction in relationship with spinning Earth. In other words after full revolution of the Earth around its axis any of the distant star

[2]More precisely to pass over the same meridian, as the Sun elevation differs slightly from day to day for the observer occupying the same point on the surface of the Earth.

would appear in the same place for the Earth based observer[3], in contrast to Sun that moved a bit over this time. Therefore, for astronomical and aeronautical applications we commonly use sidereal day measuring 23 hours and 56 minutes. This is the amount of time allowing the Earth to perform single 360° rotation (whereas in 24 hours Earth rotates by 360.986°) as seen in 2.7a.

It also does not usually make much sense to use sidereal hours, minutes or seconds for astronomical calculations. Instead, the decimal fractions of sidereal days are commonly used. To give a way to represent time in absolute terms Julian Day (JD)[4] was introduced. It is time in sidereal days measured since noon UT on January 1^{st}, 4713 B.C. Such an ancient date was used to avoid the necessity to operate on negative dates. Day starts at noon, because for astronomers making their observations at night it is more convenient to avoid changing the date during their shift. JD system does not account for leap years and leap seconds. Also, to enable representing time with a single number years and months are not used. For example calendar date of July 18^{th} 2013 16:19:53 UT represented in JD would be:

$$t_{jd} = 2456492.180475. \tag{2.13}$$

Satellites orbiting the Earth move with maximal velocities on the order of $8\,\mathrm{km\,s^{-1}}$, which are significantly smaller than the speed of light (almost $300\,000\,\mathrm{km\,s^{-1}}$). Gravitational field surrounding the Earth is also negligible on the cosmic scale. Therefore, for the purpose of this thesis an assumption of non-relativistic case is made[5]. Namely, a single clock related to terrestrial observer is used.

More thorough explanation of sidereal time, together with example on how to obtain JD from data and UT can be found in [18], chapter 5.4.

2.3 Orbital elements

Thanks to extensive observations of planet paths performed by Tycho Brahe (1546–1601) Johannes Kepler (1571–1630) was able to discover theoretical laws governing the move-

[3]Actually, there is slight yearly oscillation of the position of distant stars. It is called parallax and comes from Earth changing its position in space over the year. When around 200 B.C. Aristarchus of Samos first proposed heliocentric system to explain planet movements, lack of observed parallax was one valid argument against it. It is however easy to explain knowing that distance to stars is much larger that ancient Greeks could reasonably expect. Proxima Centauri, the closest star other than the Sun is in the distance of over 4.2 light years ($3.97 \times 10^{13}\,\mathrm{km}$) from the Earth. At this distance parallax measures only $768.8\,\mathrm{m''}$.

[4]Julian day should not be confused with Julian calendar that was introduced by Julius Caesar in 46 B.C. and was predominant calendar used throughout the Europe until it was replaced by Georgian calendar.

[5]There are some applications in space engineering where this assumption is not justified. One example of such an application would be any Global Navigation Satellite System (GNSS), which relies on extremely precise time measurements.

ment of celestial bodies First law 2.1 describes shape of the orbits, second 2.2 describes the relationship between planet velocity and it's position on the orbit, and third law 2.3 allows the calculation of orbital period.

Law 2.1 (First law of planetary motion) *The orbits of the planets are ellipses, with the Sun at one focus of the ellipse.*

Law 2.2 (Second law of planetary motion) *The line joining the planet to the Sun sweeps out equal areas in equal times as the planet travels around the ellipse.*

Law 2.3 (Third law of planetary motion) *The ratio of the squares of the revolutionary periods for two planets is equal to the ratio of the cubes of their semi-major axes.*

To describe shape of the orbit we need to define some geometric properties of a two body system. Let us assume that one body (central body) is significantly heavier than the other (satellite)[6]. Then we can say that the second body orbits the central one[7]. In this thesis only two central bodies, the Earth and the Sun, will be considered. If a satellite (e.g. a planet) orbits the Sun it's trajectory is called heliocentric orbit. If satellite revolves around the Earth we can talk about a geocentric orbit. As stated by Kepler's first law of planetary motion 2.1 orbits (paths of the small body with respect to the large one) have a shape of an ellipse[8]. The longest possible axis of the orbit ellipse is called line of apsides. Points where the line of apsides crosses orbit ellipse are called apsides. As central body lies in one of the orbit foci one of the apsides becomes the closest point on the orbit (periapsis) and the other is the farthest point (apoapsis). For heliocentric orbits periapsis and apoapsis are usually called perihelion and aphelion, respectively. For geocentric orbits terms perigee and apogee are usually used. We need two parameters to describe shape of the orbit. Eccentricity e describes shape of the ellipse ($e = 0$ for circular and $0 < e < 1$ for elliptical orbits). Semi-major axis a represents size of the orbit and it is defined as half of the distance between apsides. Pinpointing position of the orbital ellipse in space needs additional three orbital elements. This position is described in relationship to an inertial reference frame originating in the centre of central body. Description of such a frame for the Earth can be found in Sec. 2.1.2 and for the Sun in section Sec. 2.1.5 on page 6. First two base vectors of the reference frame $\hat{\boldsymbol{i}}$ and $\hat{\boldsymbol{j}}$ define reference plane. Intersection of this plane with orbital plane is called line of nodes. On this line lie two points of particular interest. Ascending node is a point on the orbit where satellite crosses the reference plane[9]

[6]This assumption is of course true in most cases. For example the Sun is six orders of magnitude heavier than the Earth, and a all man-made satellites are at least nineteen orders of magnitude lighter than our home planet. The heaviest artificial satellite orbiting Earth, the International Space Station (ISS) weights 417 289 kg as of 2013.

[7]There are known examples of binary star systems where two stars orbit their common centre of mass and multiple star systems where more than two stars follow more complicated trajectories.

[8]In reality orbits shape can be any of the conical sections (circle, ellipse, parabola or hyperbola). Hyperbolic and parabolic orbits occur when orbiting body has reached escape velocity and orbit eccentricity became greater than (hyperbolic) or equal (parabolic) to one. However, in this thesis only circular and elliptical orbits are taken into account.

[9]This plane is often called the equatorial plane, because it contains the Earth's equator.

Table 2.1: Keplerian orbital elements summary

Symbol	Unit	Name	Range
e	[n/a]	orbit eccentricity	0 to ∞
i	[rad]	orbital i	0 to π
a	[km]	semi-major axis	greater than central body radius
ν_t	[rad]	true anomaly	0 to ∞
Ω	[rad]	longitude of ascending node	0 to 2π
ω	[rad]	argument of periapsis	0 to 2π

from below, as indicated by the $\hat{\boldsymbol{k}}$ vector of the reference frame. Similarly descending node is the point where satellite crosses the plane from above. Angle Ω measured according to the right hand rule between $\hat{\boldsymbol{i}}$ vector (pointing towards Vernal equinox) and the line connecting reference frame origin with ascending node is called longitude of ascending node. Analogically, orbital element describing orbit orientation is an angle ω between the latter and the direction of periapsis is called argument of periapsis. Third of the orbit Euler angles i is called i. It can be measured between the plane of reference and orbital plane[10], or between vector $\hat{\boldsymbol{k}}$ and a vector normal to the plane of the orbit. Finally, there is one additional Keplerian element that is necessary to calculate position of a satellite on the orbital ellipse. True anomaly ν_t is an angle between vector of perigee and satellite position vector $\boldsymbol{r_s}$.

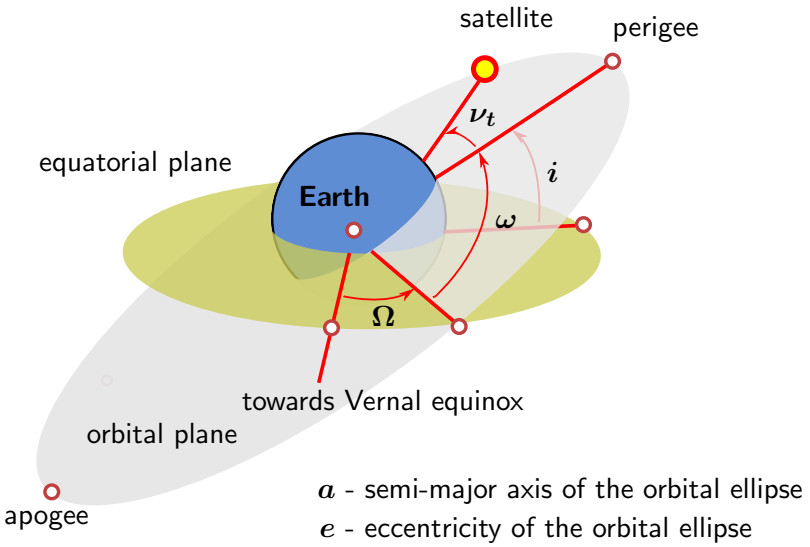

Figure 2.8: Keplerian orbital elements for geocentric orbit

In all, 6 orbital elements (also known as Keplerian elements) are needed to describe satellite's position on a defined orbit. Summary in Tab. 2.1 defines their symbols, names and units and Fig. 2.8 depicts them (except of eccentricity and semi-major axis) for a geocentric orbit. Orbital elements are often used to describe the initial condition for a model that allows calculating position of a particular satellite in a defined moment in time. To make that possible one must also known the time at which this initial condition

[10]The plane containing the orbital ellipse.

occurred. Such moment in time t_0 is often given in Julian days (see Sec. 2.2, page 8 on sidereal time) and called epoch. Additionally, mean anomaly of the ellipse ν_m is often used in this context. It is a position of a fictional body moving around the ellipse at the constant angular rate. The relationship between mean anomaly and true anomaly is precisely described in Section 3.3 of [18].

2.4 Attitude Parametrization

In this section a short outline of a commonly used attitude parametrizations is given. More comprehensive description can be found in [69].

2.4.1 Direction cosine matrix

Let us consider two reference frames sharing single origin point represented by vectrices $\mathcal{F}_a$ and $\mathcal{F}_b$ respectively. To represent orientation of $\mathcal{F}_b$ in terms of $\mathcal{F}_a$ we can use relationship (2.2) for each of the $\mathcal{F}_b$ vectors, as seen in (2.14):

$$\begin{aligned}\hat{\boldsymbol{i}}_{\boldsymbol{b}} &= c_{11}\hat{\boldsymbol{i}}_{\boldsymbol{a}} + c_{12}\hat{\boldsymbol{j}}_{\boldsymbol{a}} + c_{13}\hat{\boldsymbol{k}}_{\boldsymbol{a}} \\ \hat{\boldsymbol{j}}_{\boldsymbol{b}} &= c_{21}\hat{\boldsymbol{i}}_{\boldsymbol{a}} + c_{22}\hat{\boldsymbol{j}}_{\boldsymbol{a}} + c_{23}\hat{\boldsymbol{k}}_{\boldsymbol{a}}. \\ \hat{\boldsymbol{k}}_{\boldsymbol{b}} &= c_{31}\hat{\boldsymbol{i}}_{\boldsymbol{a}} + c_{32}\hat{\boldsymbol{j}}_{\boldsymbol{a}} + c_{33}\hat{\boldsymbol{k}}_{\boldsymbol{a}}\end{aligned} \tag{2.14}$$

Coefficients c_{xx} seen in (2.14) are direction cosines between $\mathcal{F}_b$ and $\mathcal{F}_a$ base vectors. This reference frame transformation can be therefore easily represented in matrix form as seen in (2.15):

$$\mathcal{F}_b = Q_a^b \mathcal{F}_a, \tag{2.15}$$

where:

$$Q_a^b = \begin{bmatrix} c_{11} & c_{12} & c_{13} \\ c_{21} & c_{22} & c_{23} \\ c_{31} & c_{32} & c_{33} \end{bmatrix} = \begin{bmatrix} \hat{\boldsymbol{i}}_{\boldsymbol{b}} \cdot \hat{\boldsymbol{i}}_{\boldsymbol{a}} & \hat{\boldsymbol{i}}_{\boldsymbol{b}} \cdot \hat{\boldsymbol{j}}_{\boldsymbol{a}} & \hat{\boldsymbol{i}}_{\boldsymbol{b}} \cdot \hat{\boldsymbol{k}}_{\boldsymbol{a}} \\ \hat{\boldsymbol{j}}_{\boldsymbol{b}} \cdot \hat{\boldsymbol{i}}_{\boldsymbol{a}} & \hat{\boldsymbol{j}}_{\boldsymbol{b}} \cdot \hat{\boldsymbol{j}}_{\boldsymbol{a}} & \hat{\boldsymbol{j}}_{\boldsymbol{b}} \cdot \hat{\boldsymbol{k}}_{\boldsymbol{a}} \\ \hat{\boldsymbol{k}}_{\boldsymbol{b}} \cdot \hat{\boldsymbol{i}}_{\boldsymbol{a}} & \hat{\boldsymbol{k}}_{\boldsymbol{b}} \cdot \hat{\boldsymbol{j}}_{\boldsymbol{a}} & \hat{\boldsymbol{k}}_{\boldsymbol{b}} \cdot \hat{\boldsymbol{k}}_{\boldsymbol{a}} \end{bmatrix}. \tag{2.16}$$

Q is often called the *Direction Cosine Matrix* or *rotation matrix*. It is easy to prove that such a matrix needs to be orthonormal (see [28] chapter 2.1), which means that it satisfies the following condition (2.17):

$$QQ^\top = Q^\top Q = I. \tag{2.17}$$

It is important because orthonormal matrices also have some convenient properties. For example determinant of orthonormal matrix is always equal ± 1 and it is easy to inverse such a matrix due to $Q^{-1} = Q^\top$.

2.4.2 Euler angles and Tait-Bryan angles

The Euler angles are three angles introduced by Leonhard Euler to describe the orientation of a rigid body. According to theorem 2.1 in the form taken from [81] attitude of a rigid

Table 2.2: Possible sequences of intrinsic rotations

Euler sequences	Tait-Brian sequences
$R_{\hat{\boldsymbol{i}}}(\alpha)R_{\hat{\boldsymbol{j}}}(\beta)R_{\hat{\boldsymbol{i}}}(\gamma)$	$R_{\hat{\boldsymbol{i}}}(\alpha)R_{\hat{\boldsymbol{j}}}(\beta)R_{\hat{\boldsymbol{k}}}(\gamma)$
$R_{\hat{\boldsymbol{i}}}(\alpha)R_{\hat{\boldsymbol{k}}}(\beta)R_{\hat{\boldsymbol{i}}}(\gamma)$	$R_{\hat{\boldsymbol{i}}}(\alpha)R_{\hat{\boldsymbol{k}}}(\beta)R_{\hat{\boldsymbol{j}}}(\gamma)$
$R_{\hat{\boldsymbol{j}}}(\alpha)R_{\hat{\boldsymbol{i}}}(\beta)R_{\hat{\boldsymbol{j}}}(\gamma)$	$R_{\hat{\boldsymbol{j}}}(\alpha)R_{\hat{\boldsymbol{k}}}(\beta)R_{\hat{\boldsymbol{i}}}(\gamma)$
$R_{\hat{\boldsymbol{j}}}(\alpha)R_{\hat{\boldsymbol{k}}}(\beta)R_{\hat{\boldsymbol{j}}}(\gamma)$	$R_{\hat{\boldsymbol{j}}}(\alpha)R_{\hat{\boldsymbol{i}}}(\beta)R_{\hat{\boldsymbol{k}}}(\gamma)$
$R_{\hat{\boldsymbol{k}}}(\alpha)R_{\hat{\boldsymbol{i}}}(\beta)R_{\hat{\boldsymbol{k}}}(\gamma)$	$R_{\hat{\boldsymbol{k}}}(\alpha)R_{\hat{\boldsymbol{i}}}(\beta)R_{\hat{\boldsymbol{j}}}(\gamma)$
$R_{\hat{\boldsymbol{k}}}(\alpha)R_{\hat{\boldsymbol{j}}}(\beta)R_{\hat{\boldsymbol{k}}}(\gamma)$	$R_{\hat{\boldsymbol{k}}}(\alpha)R_{\hat{\boldsymbol{j}}}(\beta)R_{\hat{\boldsymbol{i}}}(\gamma)$

body can be described in terms of three simple rotations about the body base vectors. oints to

Theorem 2.1 (Euler's Rotation Theorem) *An arbitrary rotation may be described by only three parameters.*

Let us consider a motionless reference frame $\mathcal{F}$ as in (2.1) and a rotating reference frame $\mathcal{F}_b$ tied to a rigid body (e.g. a satellite). Three elemental Euler angles can either be measured around the axes of the fixed $\mathcal{F}$ frame or around the axes of local $\mathcal{F}_b$ frame that changes orientation after each individual rotation. In the former case we call such rotations extrinsic rotations and in the later intrinsic rotations.

Term 'Euler angles' is usually used to call set of three angles of rotation around the three consecutive elemental rotation axes. Sometimes a distinction is made where this term is used only to describe sequences of rotations in which last intrinsic rotation is made along the same axis of the moving coordinate system as the first one, for example: $(\hat{\boldsymbol{k}}_{\boldsymbol{b}}, \hat{\boldsymbol{i}}_{\boldsymbol{b}}, \hat{\boldsymbol{k}}_{\boldsymbol{b}})$. Then, for rotations around three different axes (either extrinsic or intrinsic) we use the term Tait-Bryan angles.

Each set of Euler rotations can be represented by directon cosine matrix which is the product of three elementary rotation matrices $R_{\hat{\boldsymbol{i}}}$, $R_{\hat{\boldsymbol{j}}}$ and $R_{\hat{\boldsymbol{k}}}$. There are in total twelve possible sequences for intrinsic rotations. Summary of those sequences can be found in Tab. 2.2, where α, β and γ represent angle values for consecutive transformations. Angles meet the following constraints: ($0 \leq \alpha < 360°$, $0 \leq \beta \leq 180°$, $0 \leq \gamma < 360°$). Several commonly used conventions about the rotation sequence exist. Classical Euler angle sequence, which directon cosine matrix is given by (2.18):

$$Q = R_{\hat{\boldsymbol{k}}}(\alpha)R_{\hat{\boldsymbol{i}}}(\beta)R_{\hat{\boldsymbol{k}}}(\gamma), \tag{2.18}$$

and is depicted in Fig. 2.9. First rotation happens about the $\hat{\boldsymbol{k}}_{\boldsymbol{b}}$ axis tied to a rotating body that is equivalent to $\hat{\boldsymbol{k}}$ axis of the global reference frame. Second rotation happens around the new $\hat{\boldsymbol{i}}_{\boldsymbol{b}}$ axis. Finally, rotation around the final $\hat{\boldsymbol{k}}_{\boldsymbol{b}}$ happens (which is now a different vector than one that defined the first rotation direction). In the case of this particular sequence angle α is called the precession angle, β is called the nutation angle,

and γ is referred to as the spin angle. Taking into account (2.19):

$$
\begin{aligned}
R_{\hat{\boldsymbol{k}}}(\alpha) &= \begin{bmatrix} \cos\alpha & \sin\alpha & 0 \\ -\sin\alpha & \cos\alpha & 0 \\ 0 & 0 & 1 \end{bmatrix}, \\
R_{\hat{\boldsymbol{i}}}(\beta) &= \begin{bmatrix} 1 & 0 & 0 \\ 0 & \cos\beta & \sin\beta \\ 0 & -\sin\beta & \cos\beta \end{bmatrix}, \\
R_{\hat{\boldsymbol{k}}}(\gamma) &= \begin{bmatrix} \cos\gamma & \sin\gamma & 0 \\ -\sin\gamma & \cos\gamma & 0 \\ 0 & 0 & 1 \end{bmatrix},
\end{aligned}
\tag{2.19}
$$

and (2.18) we can obtain the final form of Direction Cosine Matrix for classical Euler sequence represented by (2.20):

$$
Q = \begin{bmatrix} -\sin\alpha\cos\beta\sin\gamma + \cos\alpha\cos\gamma & \cos\alpha\cos\beta\sin\gamma + \sin\alpha\cos\gamma & \sin\beta\sin\gamma \\ -\sin\alpha\cos\beta\cos\gamma - \cos\alpha\sin\gamma & \cos\alpha\cos\beta\cos\gamma - \sin\alpha\sin\gamma & \sin\beta\cos\gamma \\ \sin\alpha\sin\beta & -\cos\alpha\sin\beta & \cos\beta \end{bmatrix}. \tag{2.20}
$$

Notice from Fig. 2.9 that when nutation angle $\beta = 0^\circ$ one degree of freedom is lost. This condition, called gimbal lock[11], causes singularities in angular velocity equations based on classical Euler angle sequence (see section 9.9 of [18]). Gimbal lock is possible in any Euler sequence with different critical angles. However, for particular application a sequence can be chosen for which occurrence of gimbal lock is least likely. In space engineering it is common to parametrize rotation of $\mathcal{F}_b$ with respect to $\mathcal{F}_o$ in terms of three Tait-Bryan angles[12]: yaw ψ, pitch, θ, and roll[13] φ. According to [76] this sequence is often used to analyse attitude of space vehicles. Angles are defined in BCF as shown in Fig. 2.10. In this sequence first rotation (by yaw angle) occurs around the $\hat{\boldsymbol{k}}$ axis which is, in the beginning, equal to $\hat{\boldsymbol{k}}_{\boldsymbol{b}}$. Secondly, a body is rotated around the new $\hat{\boldsymbol{j}}_{\boldsymbol{b}}$ axis by the pitch angle. Finally, a roll rotation around the final $\hat{\boldsymbol{i}}_{\boldsymbol{b}}$ axis is made. Analogically to (2.18), (2.19) and (2.20) similar equations (2.21), (2.22) and (2.23) can be written for Tait-Bryan angles:

$$
Q = R_{\hat{\boldsymbol{i}}}(\psi) R_{\hat{\boldsymbol{j}}}(\theta) R_{\hat{\boldsymbol{k}}}(\varphi), \tag{2.21}
$$

[11] Gimbal lock does not only prove troublesome from mathematical stand point, but also has its mechanical effects. Michael Collins, astronaut, who was command module pilot for the Apollo 11 spacecraft that took first people to the Moon, has written on this subject in his popular book "Carrying the fire". Inertial Measurement Unit that allowed for navigation in space included three high-precision mechanical gyroscopes. Those basketball-sized devices consisted of three rings mounted to each other by bearings in such a way that the innermost, containing the gyroscopes rotor, could revolve freely in three axes. However, gimbal lock of such a setup was possible when outer and inner rings became aligned in a single plane. In such a case gyroscope would loose one degree of freedom, and could in result become misaligned. Astronauts had to be careful, and at all times manoeuvre the entire spacecraft in such a way, that neither of the gyroscopes experienced gimbal lock.

[12] Named after Peter Guthrie Tait and George H. Bryan. Some authors call them Cardan angles or nautical angles.

[13] Also called heading, elevation, and bank.

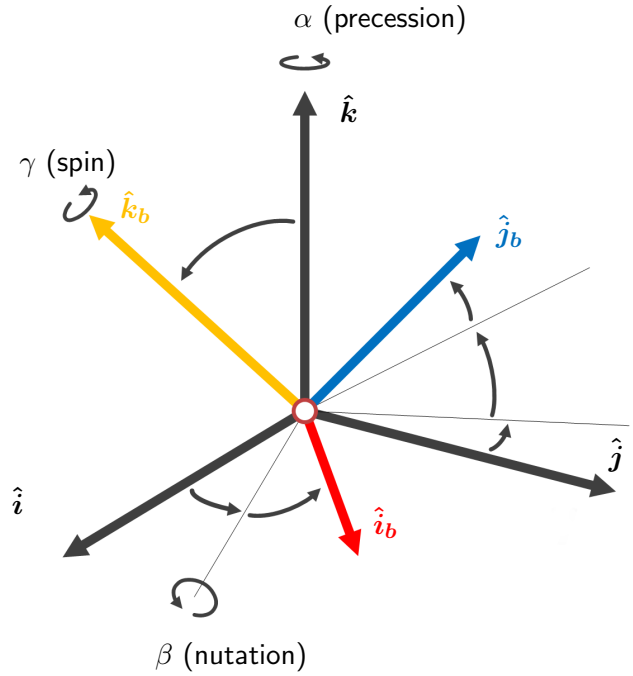

Figure 2.9: Euler angles

where

$$R_{\hat{i}}(\varphi) = \begin{bmatrix} 1 & 0 & 0 \\ 0 & \cos\varphi & \sin\varphi \\ 0 & -\sin\varphi & \cos\varphi \end{bmatrix},$$
$$R_{\hat{j}}(\theta) = \begin{bmatrix} \cos\theta & 0 & -\sin\theta \\ 0 & 1 & 0 \\ \sin\theta & 0 & \cos\theta \end{bmatrix}, \tag{2.22}$$
$$R_{\hat{k}}(\psi) = \begin{bmatrix} \cos\psi & \sin\psi & 0 \\ -\sin\psi & \cos\psi & 0 \\ 0 & 0 & 1 \end{bmatrix},$$

which can be expanded to

$$Q = \begin{bmatrix} \cos\psi\cos\theta & \sin\psi\cos\theta & -\sin\theta \\ \cos\psi\sin\theta\sin\varphi - \sin\psi\cos\varphi & \sin\psi\sin\theta\sin\varphi + \cos\psi\cos\varphi & \cos\theta\sin\varphi \\ \cos\psi\sin\theta\cos\varphi + \sin\psi\sin\varphi & \sin\psi\sin\theta\cos\varphi - \cos\psi\sin\varphi & \cos\theta\cos\varphi \end{bmatrix}. \tag{2.23}$$

Notice that this system experiences gimbal lock when pitch angle $\theta = \pm 90°$.

2.4.3 Quaternions

After discovery of complex numbers $\mathbb{C}$ many mathematicians wondered if similar number systems of even higher dimension exist. It turned out that such a structure exists in four dimensions [14]. It was discovered by Irish physicist and mathematician Sir William Rowan

[14] Precisely speaking Frobenius theorem, proved by Ferdinand Georg Frobenius in 1877, characterizes the finite-dimensional associative division algebras over the real numbers. According to the theorem,

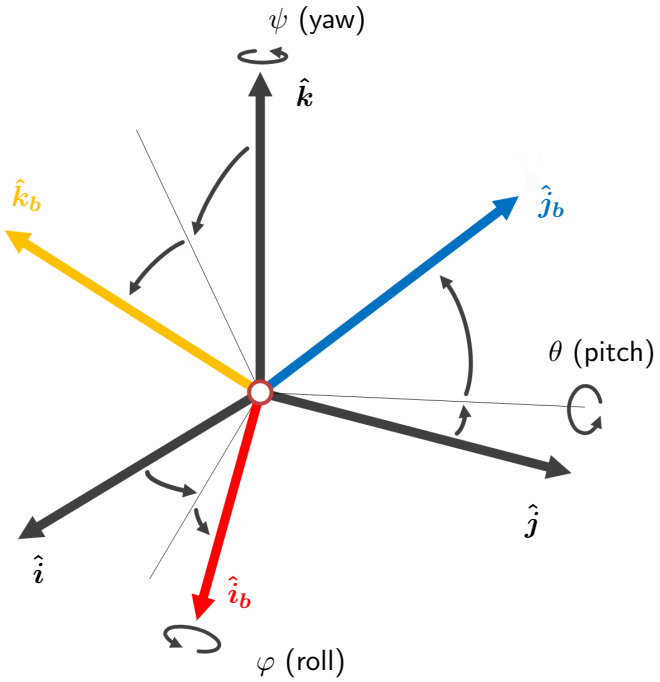

Figure 2.10: Tait-Bryan angles

Hamilton[15] [35]. He famously carved his sudden discovery in a stone of the Brougham Bridge over the Royal Canal in Dublin. In his memory set of numbers known as quaternions is often labeled by $\mathbb{H}$.

Fundamental quaternions equations can be expressed in the following way:

$$q = q_1 \cdot i + q_2 \cdot j + q_3 \cdot k + q_4, \tag{2.24}$$

where: q_1, q_2, q_3 and q_4 are real numbers and i, j, k are imaginary numbers that fulfil the following relations:

$$\begin{aligned} i^2 = j^2 = k^2 = -1, \\ ij = k, \\ ji = -k. \end{aligned} \tag{2.25}$$

According to Euler's Rotation Theorem 2.2 the most general motion of a rigid body with a fixed point is a rotation about a fixed axis (in other words for any such rotation an axis exists that remains fixed). Formulation and one of many proofs of this theorem can be found in [61]. Two parameters: Euler angle (Φ) and Euler axis ($\boldsymbol{a}$) suffice to describe that transformation.

every such algebra is isomorphic to one of three algebras: the real numbers, the complex numbers, or the quaternions. Additionally, there are octonions, which are nonassociative, but satisfy a weaker form of associativity, namely they are alternative.

[15] Although Sir W.R. Hamilton (1805 – 1865) is considered as the one who discovered quaternions it is known from Gauss notes that he probably knew them in 1819, but never bothered to publish. Much credit is also given to Benjamin Olinde Rodrigues who published a paper that addressed vectorial representations of rotations of $\mathbb{R}^3$ back in 1840.

Theorem 2.2 (Euler's Rotation Axis Theorem) *If $R(\Phi)$ is a 3×3 matrix satisfying: $R(\Phi)^\top R(\Phi) = R(\Phi)R(\Phi)^\top = I$, and: $det(R(\Phi)) = 1$, then there is a non-zero normalized vector $\boldsymbol{a}$ satisfying $R(\Phi)\boldsymbol{a} = \boldsymbol{a}$.*

It turns out that elements of the quaternionic number are in close relationship with Euler parameters and therefore provide an excellent representation of the orientation of a body in Euclidean space. Following relationships noted in (2.26) allow calculating quaternionic number value:

$$\begin{aligned} q_1 &= a_1 \cdot \sin\frac{\Phi}{2}, \\ q_2 &= a_2 \cdot \sin\frac{\Phi}{2}, \\ q_3 &= a_3 \cdot \sin\frac{\Phi}{2}, \\ q_4 &= \cos\frac{\Phi}{2}, \end{aligned} \tag{2.26}$$

where $[a_1 a_2 a_3[^\top$ are the coordinates of $\boldsymbol{a}$. It is worth noting that due to the fact that $\boldsymbol{a}$ is normalized by definition the resulting rotation quaternion also has this property. Because of relationship (2.26) it is common to refer to the purely imaginary part of the quaternion as the vector part $\boldsymbol{q_v}$ and to the real part q_4 as the scalar part, where:

$$\boldsymbol{q_v} = \begin{bmatrix} q_1 \\ q_2 \\ q_3 \end{bmatrix}. \tag{2.27}$$

Given a rotation quaternion it is fairly simple to calculate rotation matrix, following the (2.28):

$$Q = \begin{bmatrix} q_1^2 - q_2^2 - q_3^2 + q_4^2 & 2(q_1q_2 + q_3q_4) & 2(q_1q_3 - q_2q_4) \\ 2(q_1q_2 - q_3q_4) & -q_1^2 + q_2^2 - q_3^2 + q_4^2 & 2(q_2q_3 + q_1q_4) \\ 2(q_1q_3 + q_2q_4) & 2(q_2q_3 - q_1q_4) & -q_1^2 - q_2^2 + q_3^2 + q_4^2 \end{bmatrix}. \tag{2.28}$$

When talking about the quaternion attitude representation is also be useful to define basic operations on quaternions such as: product, norm and conjugate. It follows from (2.25) that:

$$\begin{aligned} jk &= -kj = i, \\ ki &= -ik = j, \\ ij &= -ji = k. \end{aligned} \tag{2.29}$$

Taking that into account consider two quaternions q and p. Their product (called Hamilton product) is equal (2.30):

$$\begin{aligned} \overline{q} \otimes \overline{p} &= (q_1 i + q_2 j + q_3 k + q_4)(p_1 i + p_2 j + p_3 k + p_4) \\ &= (q_1p_4 + q_2p_3 - q_3p_2 + q_4p_1)i \\ &+ (-q_1p_3 + q_2p_4 + q_3p_1 + q_4p_2)j \\ &+ (q_1p_2 - q_2p_1 + q_3p_4 + q_4p_3)k \\ &+ (-q_1p_1 - q_2p_2 - q_3p_3 + q_4p_4). \end{aligned} \tag{2.30}$$

By definition quaternion norm is represented by (2.31):

$$\|\overline{q}\| = \sqrt{q_1^2 + q_2^2 + q_3^2 + q_4^2}. \tag{2.31}$$

Quaternion conjugate (analogically to complex numbers) is represented by (2.32):

$$\overline{q}^* = -q_1 i - q_2 j - q_3 k + q_4. \tag{2.32}$$

Let us assume unit quaternion ${}^p_r\overline{q}$ describing orientation of frame $\mathcal{F}_r$ relative to frame $\mathcal{F}_p$. Quaternion ${}^r_p\overline{q}$ representing opposite relationship is equal to conjugate of ${}^p_r\overline{q}$:

$${}^p_r\overline{q}^* = {}^r_p\overline{q} = [-q_1 \; -q_2 \; -q_3 \; q_4]^\top. \tag{2.33}$$

Quaternion product (also known as Hamilton product) can be used to express transformation superposition:

$${}^p_r\overline{q} = {}^s_r\overline{q} \otimes {}^p_s\overline{q}. \tag{2.34}$$

It is also possible to describe a vector ${}^r\boldsymbol{v}$ defined in reference frame $\mathcal{F}_r$ in the other reference frame $\mathcal{F}_p$ using quaternion product. This calculation requires converting 3×1 vector ${}^r\boldsymbol{v}$ to 4×1 quaternion ${}^r\overline{\boldsymbol{v}}$ by adding 0 as the scalar element. Then the frame change can be calculated according to the following equation:

$${}^p\overline{\boldsymbol{v}} = {}^r_p\overline{q} \otimes {}^r\overline{\boldsymbol{v}} \otimes {}^r_p\overline{q}^*. \tag{2.35}$$

While applying orientation quaternion algebra it is often necessary to perform normalisation operation. Let us then define normalization operator to simplify the notation:

$$\nparallel \overline{q} \nparallel = \frac{\overline{q}}{\|\overline{q}\|}. \tag{2.36}$$

Chapter 3

Control and modelling problems concerning nanosatellites

The following chapter is a brief introduction to some of the control and modelling problems concerning nanosatellites. First, the nanosatellite term itself is explained in Sec. 3.1 together with short historical introduction, data on the growing utilization and specific constraints of this satellite class. Sec. 3.2 contains short description of the nanosatellite attitude determination and control system, followed by explanation basic attitude control tasks, the detumbling and pointing. Afterwards, the most importnt disturbance torques are listed. Section ends with short description of each of the basic parts of the attitude control system. The last section of this chapter (Sec. 3.3), is dedicated to literature review outlining some of the existing attitude estimation techniques.

Of course, there are also other control tasks important for nanostatellites, such as the thermal control of its subsystems. They however, lie well outside the scope of this work and are, therefore, omitted

3.1 Introduction to nanosatellites

First really small satellites of mass lower than 20 kg appeared in early '90s. Four *Oscar* class satellites built by *Amsat-North America* and *Webber State University* were launched on board *Ariane 40* rocket. Their main purpose was amateur satellite communication, but they also carried limited Earth imaging capabilities. Until year 2000 as many as 21 satellites not heavier than 20 kg where launched. Since then even smaller satellites where developed every year at ever increasing rate. Informal size classification of satellites shown in Tab. 3.1 has been established as a result of this miniaturization.

Publication of CubeSat standard [36] by Cal Poly State University was one of the main factors facilitating a quick raise in numbers of nano and pico satellites. As designing and certification a satellite interface with launch vehicle is very expensive, standardization

Table 3.1: Satellite size classes depending on initial launch mass

Size class	Mass
Large satellite	1000 kg
Medium satellite	500 kg to 1000 kg
Minisatellite	100 kg to 500 kg
Microsatellite	10 kg to 100 kg
Nanosatellite	1 kg to 10 kg
Picosatellite	100 g to 1000 g
Femtosatellite	1 g to 100 g

allowed to use a common P-Pod device for CubeSats deployment. Even smaller femtosatellites have been proposed since then [6], but so far they did not attracted wider attention. Another reason for the popularity of CubeSats was the fact that the launch providers introduced initiatives allowing for easier access to the rockets for small satellite developers. In 2010, National Aeronautics and Space Administration (NASA) began the CubeSat Launch Initiative (CSLI)), providing a method to launch auxiliary payloads on planned launches. The initiative is open to NASA centres, U.S. non-profit organizations, and accredited U.S. educational organizations. Selected CubeSats launch in missions called ELaNa. CSLI is partly responsible for the increase in the number of projected science and engineering payloads between 2012 and 2014. ELaNa-1 launched aboard a failed non-commercial Taurus XL flight in 2009. ELaNa-2, originally scheduled for a non-commercial Taurus XL launch in 2013, was postponed. ELaNA-3 launched aboard a non-commercial Delta II flight in 2011, and ELaNA-4 was carried by US Air Force Minotaur-1 rocket from Wallops Flight Facility in Virginia. Several nanosatellites of various sizes were launched each time. Since then a nanosatellite segment experiences a steady growth. Bar plot in Fig. 3.1 shows the successful, unsuccessful and projected nanosatellite mission numbers as of May 2016. The distribution of nanosatellite amongst different sizes of platforms is shown in Fig. 3.2. Interestingly, a three unit[1] CubeSat standard satellites seem to be in a sweet spot with being a cheap and reliable platform, with enough potential to actually perform meaningful research and services.

Constraints of the nanosatellites

It is important to note that all satellites have limited volume and mass, as the cost of launch is determined by both the size and weight of the spacecraft. This is especially true for nanosatellites. Limited size also translates in a smaller surface area available solar arrays, and much less space for batteries. This severely limits the satellites power production and storage capabilities. Due to those factors several techniques are used:

Limited subsystem redundancy Due to the small size the total cost of a nanosatellite mission is low when compared to bigger spacecraft. This changes the balance of risk management. Rather than having lots of redundant components in a single

[1] 3U CubeSat has around three times the mass and volume as the 1U standard. See [36] for details on CubeSat sizes and masses.

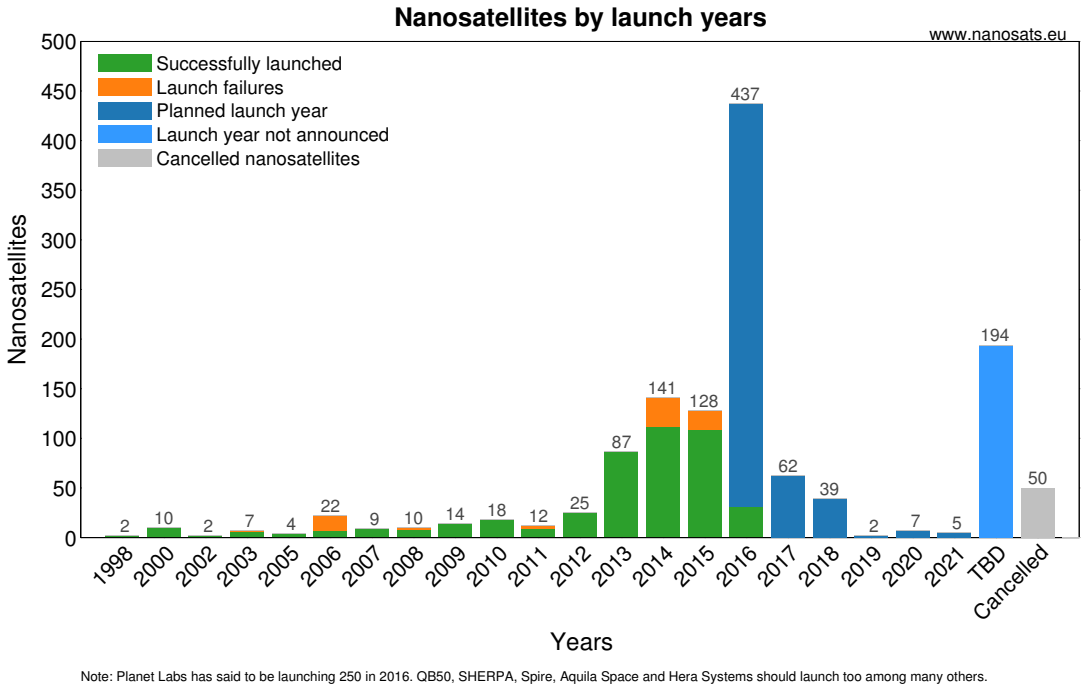

Figure 3.1: Actual and planned nanosatellite launches (source: [33])

satellite, a higher risk of mission failure is accepted. Also, due to the fact than the satellite itself becomes relatively cheap to manufacture more satellites can be used in a constellation with an assumption that some of them can fail (e.g. QB50 project [26]).

Simple sensors Nanosatellites need to use relatively cheap and simple sensors for attitude determination, guidance and navigation, science operations and internal platform functions. This is one of the reasons for developing new attitude determination methods, taking into account the sensor type and possibility of their periodic data loss. This underlines the significance of thesis 1 and 2 of this study proposed in Sec. 1.2.

Limited thermal control It is often not possible to actively stabilize the temperature of the equipment aboard the satellite mainly due to the required weight of radiators, heaters and other related equipment. This leads to accepting less efficient scheme of passive temperature control. As internal electronics, batteries and structure materials are subjected to harsh temperature cycles nanosatellite missions are usually considerably shorter than those of bigger spacecraft. Temperature variations also cause some problems with measurements, as described in Sec. 6.3.1 and Sec. 6.3.2.

Lack of delta V capability Although introducing thrusters for nanosatellites orbit control has been proposed [32], achieved capabilities where rather low. Commonly, it is accepted that if due to the error in the satellite orbital insertion spacecraft ends up on an incorrect orbit it will not be able to correct it. This enforces the paradigm of accepting the higher risk of mission failure to significantly decrease the complexity and cost of a satellite.

Limited power Solar arrays of such a small satellite have, by necessity, small surface area. This leads to very stringent electrical power production limitation. Due to this

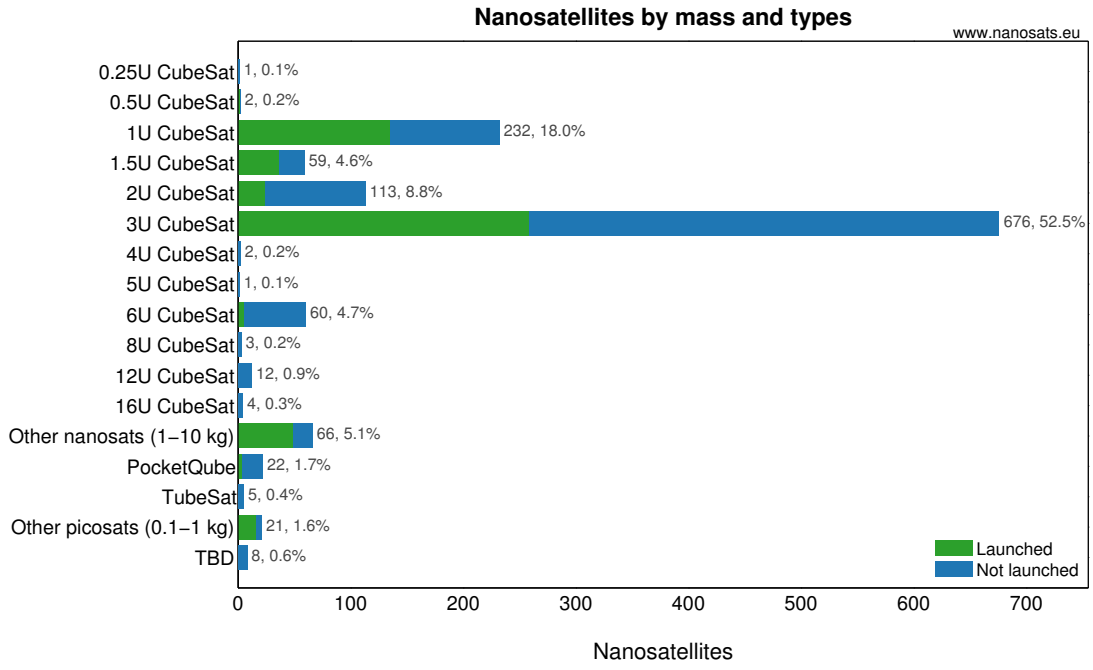

Figure 3.2: Nanosatellite size distribution (source: [33]). The 1U CubeSat is a satellite of the internal volume of $1000\,\mathrm{cm}^3$. The number before the "U" letter represents factor by which this volume is multiplied. See [36] for a specific information of CubeSat sizes defined by the standard.

fact it is important to select components which utilize it efficiently and limit their selection to only the most essential ones for a particular mission. It is also important to use less powerful onboard computer, which in turn demands less computationally expensive algorithms. Thesis 3 of this work (see Sec. 1.2) also proposes interesting concept of using more energy consuming sensor with lower sampling rates, and at the same time compensating with the more efficient ones.

3.2 Spacecraft Attitude Control

Spacecraft attitude can be controlled with utilization of classical Automatic Control System (ACS) approach shown in Fig. 3.3. This control system generally consists of attitude sensors, attitude controller and a set of actuators. Spacecraft attitude cannot be directly measured, so it is also necessary to include attitude estimation algorithm that filters and interprets measured attitude indicators. Desired attitude usually comes from the mission requirements. It usually aims at orienting a scientific instrument at its target: communication antenna at the ground station or the solar panels in an optimal alignment in relation to to the Sun. This mode, sometimes referred to as spacecraft pointing, is outlined in Sec. 3.2.2. There are also instances, when attitude control works in a limited fashion, only by maintaining the angular rate within the desired limits. This process, called detumbling usually takes place to de-spin the satellite after the release from the launch vehicle or to recover from a failure and is briefly described in Sec. 3.2.1.

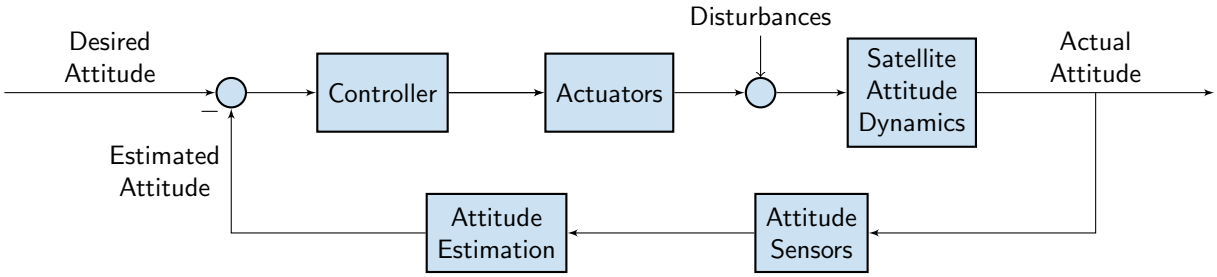

Figure 3.3: Attitude determination and control system

Attitude controller is producing control signals for the actuators, based on a desired attitude and current attitude estimate. It needs to balance high pointing precision, quick slew of the spacecraft to the desired orientation and conservation of energy and fuel. There are many types of attitude actuators, briefly described in Sec. 3.2.4.

Of course, in addition to the torque produced by the actuators there are also attitude disturbances at play. Most important ones are outlined in Sec. 3.2.3. All those torques influence the rotational movement of the spacecraft. Brief comment on the attitude dynamics can be found in Sec. 3.2.5.

Classical formulation of attitude estimation problem can be found in Sec. 3.2.8. Many ways of estimating the satellite's attitude have been developed. A summary of several methods can be found in Sec. 3.3 and comparison of their performance for a proposed case study is given in Sec. 6.4.2. They rely on models of the measured values (some of which are described in Ch. 4) and compare them with measurements of the onboard sensors (see Sec. 3.2.7).

3.2.1 Detumbling

After release of the satellite from launch pod it often acquires relatively high angular velocity. This condition is known as tumbling. It can also occur due to disturbance torques[2] when attitude control of the spacecraft is disabled or faulty. It is necessary for the attitude control system to counteract tumbling and bring the satellite's angular velocities to the acceptable levels. This control task is often referred to as detumbling. It can be done either by designing satellite to achieve stable, low spin condition with passive utilization of existing disturbance torques, or by actively transferring away the kinetic Energy by the means of a control torque. For small Low Earth's orbit (LEO) satellites it is most often done by transferring the momentum to Earth via magnetic field with magnetorquers (see Sec. 3.2.4.

[2]This happened for CubeSat class AAUSAT-II satellite, which started to tumble for unknown reason. It became very difficult to acquire link with the satellite, and ground controllers were able to save the spacecraft by carefully studying the available data to uncover the cause and using the spacecraft magnetic coils to gradually slow the rotation.

B-Dot detumbler

Control law designed to detumble satellite by means of magnetic control, the B-Dot detumbler, was first introduced by Stickler and Alfriend [72]. It is a simple and reliable solution, because it requires no moving parts, only a 3-axis magnetic field sensor and three orthogonal[3] configuration of magnetic torquers. Control law can be derived from the assumption that kinetic energy of rotation should decrease monotonically:

$$\frac{dE_{rot}}{dt} = \frac{d}{dt}\left(\frac{1}{2}{}^{b}\boldsymbol{\omega}^{\top}\mathrm{I}^{b}\boldsymbol{\omega}\right) < 0, \tag{3.1}$$

where I is the inertia matrix and ${}^{b}\boldsymbol{\omega}$ is an angular velocity of BCF body frame with respect to inertial Earth-Centred, Earth-Inertial (ECI) frame expressed in BCF frame tied to a spacecraft. As this derivative can be estimated with

$$\frac{dE_{rot}}{dt} = \mathrm{I}^{b}\dot{\boldsymbol{\omega}} \approx {}^{b}\boldsymbol{\omega} \cdot {}^{b}\boldsymbol{\tau_c}, \tag{3.2}$$

one can approximate condition (3.1) with

$${}^{b}\boldsymbol{\omega} \cdot {}^{b}\boldsymbol{\tau_c} < 0. \tag{3.3}$$

Knowing that scalar and vector products are interchangeable:

$$\boldsymbol{a} \cdot (\boldsymbol{b} \times \boldsymbol{c}) = \boldsymbol{c} \cdot (\boldsymbol{a} \times \boldsymbol{b}), \tag{3.4}$$

and

$${}^{b}\boldsymbol{\tau_c} = {}^{b}\boldsymbol{\mu} \times {}^{b}\boldsymbol{B} = -{}^{b}\boldsymbol{B} \times {}^{b}\boldsymbol{\mu}, \tag{3.5}$$

one can write (3.3) as:

$$-{}^{b}\boldsymbol{\mu} \cdot ({}^{b}\boldsymbol{B} \times {}^{b}\boldsymbol{\omega}) < 0, \tag{3.6}$$

or

$${}^{b}\boldsymbol{\mu} \cdot ({}^{b}\boldsymbol{\omega} \times {}^{b}\boldsymbol{B}) < 0, \tag{3.7}$$

Note, that for the scalar product in (3.7) to be negative the angle between ${}^{b}\boldsymbol{\mu}$ and ${}^{b}\boldsymbol{\omega} \times {}^{b}\boldsymbol{B}$ needs to be greater than $\frac{\pi}{2}$ rad. Maximum efficiency is achieved when angle equals π rad, namely:

$${}^{b}\boldsymbol{\mu} = -K_d({}^{b}\boldsymbol{\omega} \times {}^{b}\boldsymbol{B}), \tag{3.8}$$

where K_d is a negative constant gain. B-dot control law is then expressed by (3.9):

$${}^{b}\boldsymbol{\mu} = -K_d{}^{b}\dot{\boldsymbol{B}}, \tag{3.9}$$

with assumption that change in the magnetic field vector ${}^{b}\boldsymbol{B}$ direction is only due to spacecraft rotation, meaning:

$${}^{b}\dot{\boldsymbol{B}} = {}^{b}\boldsymbol{\omega} \times {}^{b}\boldsymbol{B}. \tag{3.10}$$

Of course it is not always fulfilled, because of two facts. Firstly, the satellite moves around the Earth, which generates magnetic field shape similar to that of a magnetic dipole. If

[3]Precisely speaking orthogonality is only desired for simplicity and maximum effectiveness, in theory any linearly independent configuration works. This can be leveraged, by using four or more magnetic coils for redundancy.

a satellite travels on the polar orbit, passing over magnetic north and south poles it will experience one full rotation of the magnetic filed vector every orbit. So even when satellite detumbles, until the change in magnetic vector direction in body frame is non-existent it still revolves in the inertial frame. However, as one orbit even on LEO takes in the vicinity of 100 min[4] this residual angular velocity can be safely neglected. Secondly, if a satellite travels around the Earth following near equatorial orbit the magnetic field vector does not change its direction significantly in the inertial frame. This in turn means that rotation around the vector of direction of magnetic field vector is impossible to dump by the means of magnetic actuation. Furthermore, it is also impossible to measure its rate with magnetometers alone. Diagram showing the basic detumbling principle is shown in Fig. 3.4.

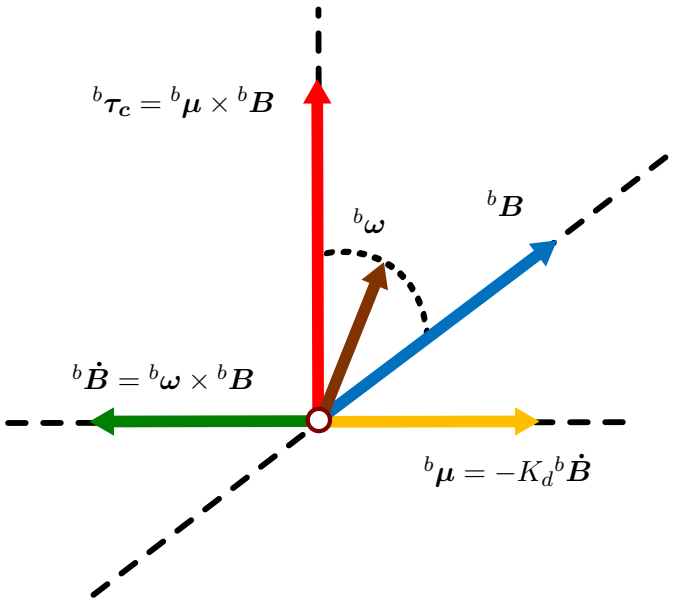

Figure 3.4: B-dot detumbling principle

3.2.2 Spacecraft pointing

Earth orbiting satellites are usually logically (and often also physically) divided into platform and payload. Payload is determined by the primary function of the satellite. For example for communication satellites it includes all antennas and radio equipment, for GNSS satellite includes essential communication equipment and precise clock while remote sensing satellites carry remote sensors. On the other hand platform of the satellite is designed to provide conditions vital for functioning of the payload such as: electrical power, thermal control, data link with ground control, correct position and orientation of the instruments. For most satellites it is vital that payload sensors and communication

[4] LEO orbits are defined as having altitude between 160 km (orbital period of about 88 min), and 2.000 km (about 127 min).

antennas are pointing in the right direction. Satellite that is to take a picture of a predefined target needs to actively detect and control its orientation in space to point the instrument. Earth observing satellite can use process symbolically depicted on diagram

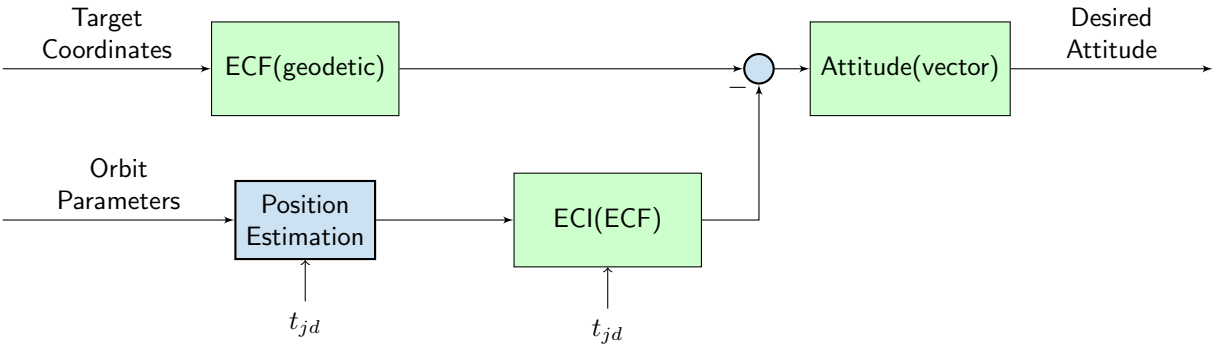

Figure 3.5: Determination of the desired attitude for Earth observing satelites

in Fig. 3.5. It is first necessary to know position of the target of interest on Earth surface, which is often expressed in geodetic coordinates, like longitude, latitude and altitude. Then it is necessary to determine position of the satellite on the orbit. This can be done for example by propagating position described by orbital elements from epoch time to the current Julian Day t_{jd} (see Sec. 2.2). Position of the satellite is usually expressed in the inertial frame like ECI and the target rotates with Earth-Centred, Earth-Fixed (ECF) frame tied to the Earth (see Sec. 2.1.1). So it is necessary to bring both of those two position to a single frame of reference, for example by transforming satellite position from ECI to ECF. Then it is easy to calculate directional vector from the satellite to the desired object, transform it to the attitude representation form used by the control system (attitude matrix, attitude quaternion, etc.). Knowing the desired attitude a spacecraft needs to be able to estimate its current attitude, and use actuators to change it.

3.2.3 Attitude disturbance torques

One could expect that with absence of air and therefore no external friction there are no disturbances acting upon a spacecraft in Earth orbit. Even on close examination there are no sources that can be intuitively classified as "large". However, a typical satellite is designed to point its instruments in a very precise manner for relatively long periods of time[5]. This kind of requirement makes it necessary to analyse even smallest disturbance sources, to make sure that control authority is maintained even in worst-case scenario.

Disturbances acting upon a satellite can be divided into external and internal as depicted on diagram shown in Fig. 3.6. External effects are those characterizing the Space environment. They would act event if a spacecraft itself was a rigid body. Internal disturbances are closely related to spacecraft structure, in particular: internal moving parts and mass or radiation being emitted.

[5]For example each nanosatellite of BRITE constellation was initially designed to maintain pointing accuracy of at least $60''$.

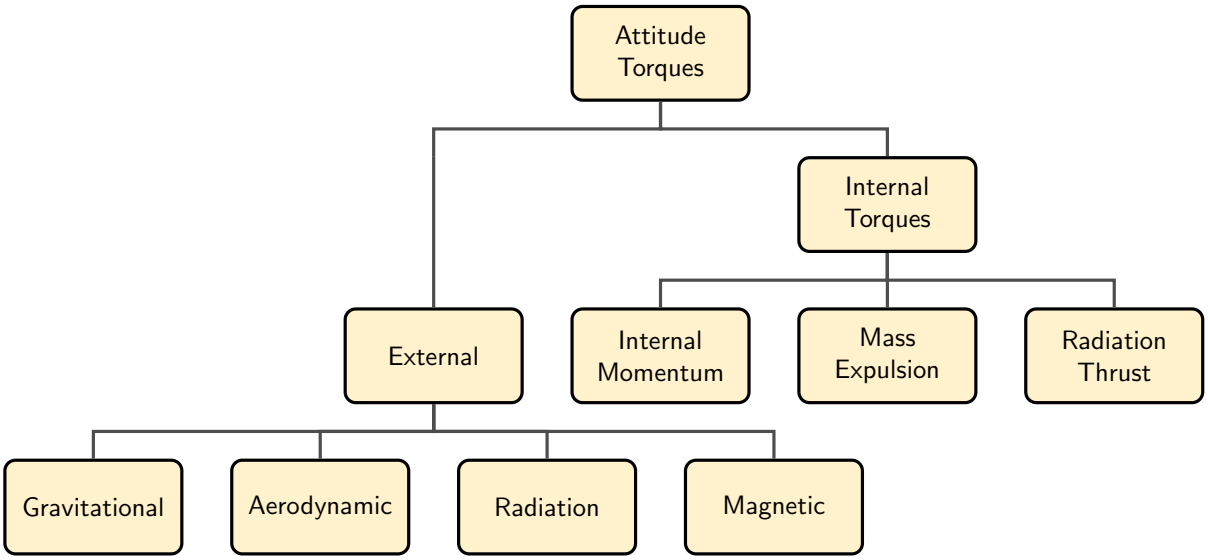

Figure 3.6: Sources of torques affecting satellite attitude

Diagram in Fig. 3.7 shows comparison of common torque values on a example spacecraft vs. attitude. Analysis is based on [28] and it should only be treated as an example. Each torque is heavily dependent on a satellite's shape, design and designated orbit. However, it is worth noticing that gravity gradient torque varies as r_s^3, where r_s is the distance to the Earth's gravitational centre. This is also to some extent true for magnetic torque, although it is additionally heavily dependent on orbit inclination and local anomalies. Aerodynamic torque is dependent on atmosphere density and decreases approximately exponentially with altitude. Because of their nature torques from meteoroidal impacts and solar pressure are almost constant with altitude and do not depend on the distance from the Earth.

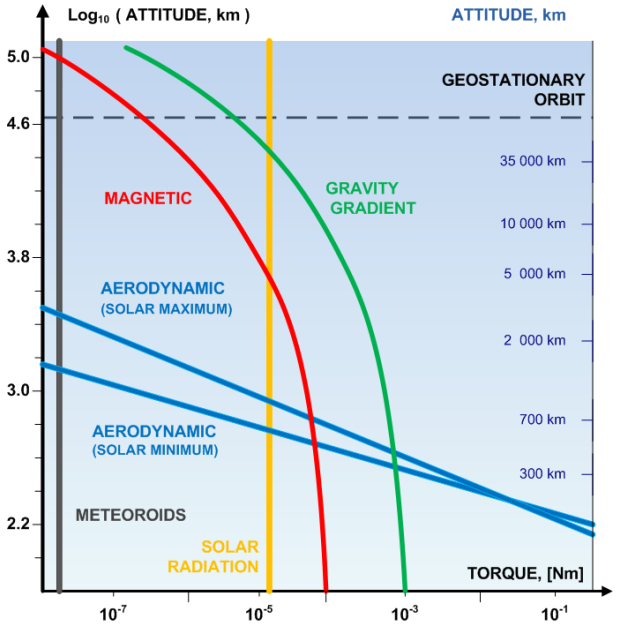

Figure 3.7: Influence of several common torques on an example spacecraft vs. altitude (plot based on [28])

Gravitational Torque

Gravitational force between the Earth and a satellite in orbit is obviously the dominant interaction. It causes spacecraft to obey Keppler's laws of planetary motion. Irregularities of mass distribution in Earth's crust, impact of gravitational attraction by Sun and Moon and tidal movements of oceans cause deviations from ideal elliptical orbit. Those irregularities usually do not need to be corrected by spacecraft's propulsion but rather their effects are taken into account while interpreting scientific measurements or performing other satellite's tasks. However, there is another meaningful effect caused by non-uniformity of gravitational field around the Earth's centre of mass. In uniform field satellites centre of mass would become a centre of gravity as well. In case of Earth gravitational field, which is not uniform, if a spacecraft's mass distribution is not spherically symmetrical this results in a non-zero torque about the centre of mass. Because of this torque stable attitude equilibria (up to 24 according to [28]) may emerge[6]. A simplistic

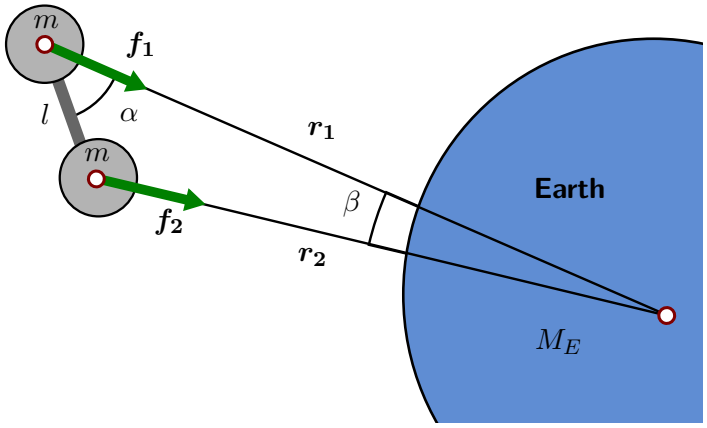

Figure 3.8: Gravity gradient torque example

model shown in Fig. 3.8 represents a satellite immersed in the Earth's inverse square gravitational field. Satellite consists of two identical balls of fixed mass m. They are connected with rod of negligible mass and with length equal l. Satellite is oriented in such a way that second ball lies in a distance $\boldsymbol{r_2}$ from the Earth's mass centre which is greater than the corresponding distance $\boldsymbol{r_1}$ of a first ball. As size of the balls is very small in comparison to those distances they can be treated as point masses. Therefore, we can describe forces acting on those two parts as:

$$\begin{aligned} \boldsymbol{f_1} &= -G\frac{mM_E}{\|\boldsymbol{r_1}\|^2}\frac{\boldsymbol{r_1}}{\|\boldsymbol{r_1}\|} \\ \boldsymbol{f_2} &= -G\frac{mM_E}{\|\boldsymbol{r_2}\|^2}\frac{\boldsymbol{r_2}}{\|\boldsymbol{r_2}\|} \end{aligned}, \tag{3.11}$$

[6]This phenomenon was used by Lagrange in 1780 to explain why the Moon always faces the Earth with the same hemisphere. Some satellites use this principle for passive attitude stabilization. By deploying gravity gradient booms and somehow dumping initial post-launch angular momentum those spacecraft can maintain Earth-oriented position through their orbit [28]. Usually additional spin stabilization is employed by forcing space vehicle to slowly spin around the axis passing through both it's centre of mass and centre of gravity. This approach has a limited precision, but does not require any fuel to maintain stable attitude. This configuration was for instance used by series of Transit satellites that were part of positioning system that preceded the Global Positioning System (GPS).

where G is gravitational constant and M_E is the mass of the Earth. Assuming that angle β is very small due to $\boldsymbol{r_1} \gg l$ and $\boldsymbol{r_2} \gg l$ value of the resulting torque $\boldsymbol{\tau_g}$ along satellite's centre of mass will be described by following approximate relationship:

$$\|\boldsymbol{\tau_g}\| = \frac{l}{2} \|\boldsymbol{f_2} - \boldsymbol{f_1}\| \sin\alpha. \tag{3.12}$$

From (3.11) and the fact that $\boldsymbol{r_1} > \boldsymbol{r_2}$ it becomes clear that $\|\boldsymbol{f_1}\| < \|\boldsymbol{f_2}\|$. Therefore, as long as $\sin\alpha$ does not equal zero (which happens in equilibria) there will be a non zero torque along the centre of the rod. Similar principle can be used to determine torque acting on a more complex satellite, by dividing it into small components analytically or with utilization of computer simulation.

Aerodynamic Torque

Intuitive assumption of ideal vacuum being one of the characteristics of space environment is not precise. The boundary of space is defined in several ways. Kármán line 100 km above sea level is often used because roughly at this altitude a vehicle would have to travel faster than orbital velocity in order to derive sufficient aerodynamic lift from the atmosphere to support itself [19]. In USA every person who flew higher than 80 km is considered an astronaut. At the same time altitude of 122 km was recognized as the space shuttle re-entry boundary because at this point atmospheric drag becomes a dominant force.

At the altitude of 700 km the average air density is on the order of $10\,\mathrm{g\,cm^{-3}}$ to $16\,\mathrm{g\,cm^{-3}}$. There are two main reasons why such a small amount of air can have impact on satellite attitude and trajectory. First of all air drag effects accumulate for the whole lifetime of a spacecraft. Secondly, it is crucial to understand that objects orbiting the Earth need to be travelling with very large velocities. High relative speed causes significant momentum transfer between spacecraft and colliding air particles.

Value of orbital velocity of a satellite in circular orbit $\boldsymbol{v_s}$ is represented by following relationship

$$\|\boldsymbol{v_s}\| \simeq \sqrt{\frac{GM^2}{(m+M)R}}, \tag{3.13}$$

where M is a mass of the Earth, m is a mass of satellite, G is a gravitational constant and R is a distance between centres of mass. For a spacecraft of negligible mass orbiting the Earth at altitude of 700 km (plus the Earth's radius) this velocity[7] will be approximately $7.5\,\mathrm{km\,s^{-1}}$.

[7] Air drag causes low altitude satellites orbits to decay. Notice that from equation (3.13) square of orbital velocity is reverse proportional to orbit's altitude. This means that contrary to common misconception satellites are not slowed down by atmospheric drag but rather they gain velocity with decreasing orbit altitude. This is of course true only until atmospheric density becomes high enough. At certain altitude orbital mechanics equations cease to be a good estimation and satellite breaks up in atmosphere or deorbits. Classical fluid dynamics drag equation gives an estimation of an atmospheric drag force acting upon a satellite.

The aerodynamic force $\boldsymbol{f_a}$ will act in the opposite direction to a velocity vector with a value approximated by relationship

$$\|\boldsymbol{f_a}\| = \frac{\rho C_d S v_s^2}{2}, \tag{3.14}$$

where ρ is an atmospheric density, C_d is a drag coefficient of the satellite, S is the reference area and v_s is the velocity of a satellite. Apart from decaying orbit of the spacecraft it is also observed that atmospheric drag can influence spacecraft's attitude. If a spacecraft's centre of pressure lies far from centre of mass, as shown in Fig. 3.9, drag force will introduce torque[8] accordingly to following equation:

$$\boldsymbol{\tau_a} = \boldsymbol{l_{cm,cp}} \times \boldsymbol{f_a}, \tag{3.15}$$

where $\boldsymbol{l_{cm,cp}}$ is a distance vector between centre of mass and drag force application point.

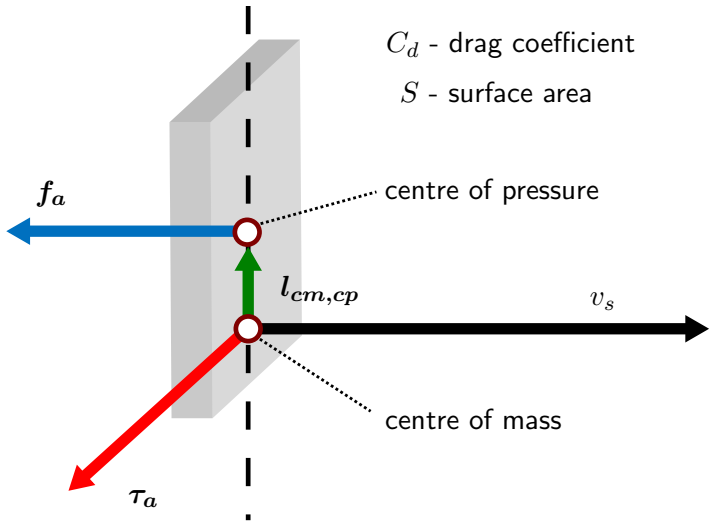

Figure 3.9: Simplistic example of atmospheric drag torque

Unfortunately this model is in many cases to simple to provide precise enough estimation. For greater precision at orbital altitudes atmosphere should be modelled as individual particles colliding witch spacecraft because mean free path (average distance travelled by gas particle before hitting other particle) is on the order of kilometres. This approach is known as free-molecular flow model [73] and in this case is more precise than conventional continuum flow model.

At typical LEO attitude of 700 km the difference in atmospheric density between solar minimum and solar maximum[9] can be as large as two orders of magnitude [40] ranging from $1 \times 10^{-15}\,\mathrm{g\,cm^{-3}}$ to $1 \times 10^{-17}\,\mathrm{g\,cm^{-3}}$.

[8]This is one of the reasons why low orbit spacecraft are very often symmetrical. Designers seek to avoid creating aerodynamically stable orientations and thus minimize the atmospheric drag torques.

[9]Day-Night cycle and local weather conditions also have a major impact on atmosphere. Many atmosphere density profile models have been constructed [52]. Mass Spectrometer - Incoherent Scatter (MSISE)-90 is the one recommended by European Cooperation for Space Standardization (ECSS) [94]. Unfortunately, the biggest difficulty lies in predicting solar activity. This uncertainty makes it very hard to precisely predict impact of the atmospheric drag on a satellite.

Environmental Radiation Torque

Environmental radiation in near Earth space comes from three main sources. First of all it is direct radiation from Sun of average 1371 $\mathrm{W\,m^{-2}}$. This amount varies seasonally by about $\pm 3\,\%$ due to Earth's orbit eccentricity. Secondly, about $30\,\%$ of sunlight gets reflected from the Earth due to the albedo effect. Rest of the solar radiation hitting Earth is absorbed and emitted back with some delay in form of infrared radiation. This process is schematically shown on diagram in Fig. 3.10.

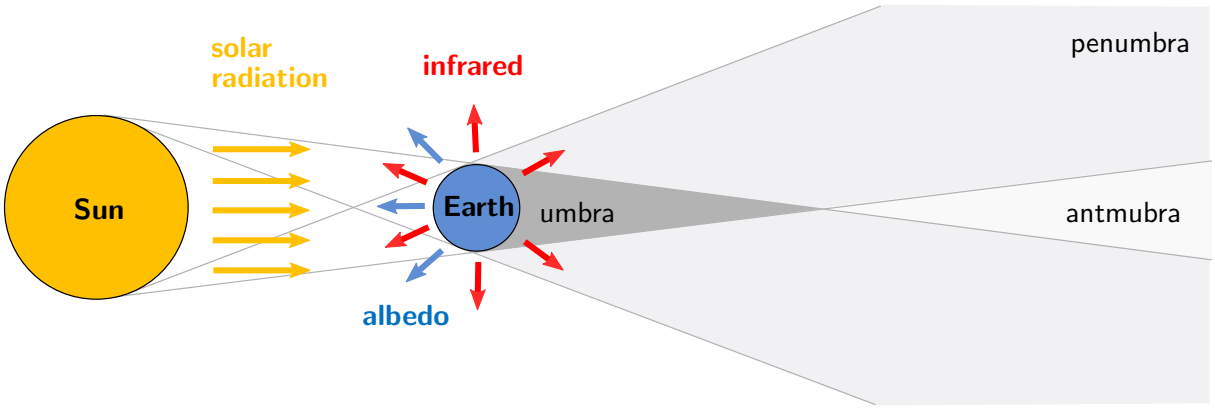

Figure 3.10: Earth energy balance. The planet is illuminated by the solar radiation. Some of it is reflected from the surface thanks to the albedo effect. Some inferred radiation is also emited from the Earth, both on the illuminated sided and the night side.

It is important to note that satellites are not always subjected to direct sunlight due to shadow casted by the planet. Region where they are experiencing a full eclipsing of the Sun by the Earth is called umbra. Another zone, where only part of the Sun is visible from behind the Earth is called penumbra. If the satellite is on a sufficiently high altitude orbit full eclipsing of the Sun by the Earth becomes impossible, as the star footprint is larger than that of a planet. This region is often called an antumbra.

Since Nichols invented his radiometer in 1901, it is known that radiation causes a pressure on surfaces. This pressure can be easily explained in terms of corpuscular nature of radiation. Each photon carries some momentum that is partially transferred on impact. Efficiency of this transfer depends on surface's absorption, reflection, and transmission characteristics. Depending on those values proper statistical analysis of absorbed, diffusely reflected and secularly reflected photons should be performed. If high precision is not needed rough approximation of radiation torque can be calculated in a similar fashion as in case of atmospheric drag. Assuming non-transparent surface with area S, unit normal vector n, reflectance r, normal radiation energy flux onto unit of area per unit of time S_0, speed of light c, normalized solar radiation incidence vector $\boldsymbol{S}$, and distance between centre of mass and radiation pressure $\boldsymbol{l_{cm,cr}}$ approximation of torque can be given by relationship:

$$\boldsymbol{\tau_a} = \boldsymbol{l_{cm,cr}} \times \frac{S S_0}{c}(1+r)(\boldsymbol{S}\cdot\boldsymbol{S})\boldsymbol{S}. \tag{3.16}$$

This method was used for estimating the worst case scenario solar pressure affecting Compass 1 satellite [25].

One of the first observed examples of solar pressure affecting spacecraft attitude was Alouette 1 satellite. This spin-stabilized spacecraft was equipped with exceptionally long (45.7 m) dipole antennas. It turned out that antennas were flexible enough to be slightly bent away from the Sun by solar pressure (Fig. 3.11). As satellite was spinning around it's centre of mass deforming antennas stayed a little longer under solar pressure's influence while swinging toward the sun and shorter while moving away. Over the course of two years spin ratio of Alouette decreased from 1.4 to 0.3 revolutions per minute significantly undermining attitude stabilization efficiency (Fig. 3.11).

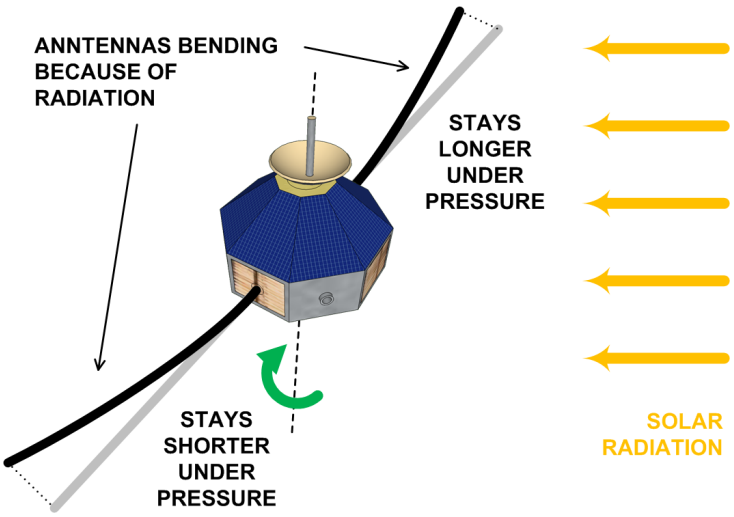

Figure 3.11: Alouette 1 satellite with solar pressure affecting flexible antennas

Often engineers can take advantage of this otherwise harmful effect. Solar radiation torque was used to stabilize Mariner 4 probe attitude on its way to Mars [28]. Four adjustable solar vanes were added at the top of spacecraft's solar panels. Those black plates where positioned in such a way that point of application of solar radiation force was moved behind the spacecraft's centre of mass. This made Mariner 4 statically stable in terms of attitude.

Magnetic Torque

There are several mechanisms that can affect attitude of a spacecraft immersed in magnetic field. Unarguably most important interaction occurs when spacecraft has non-zero net magnetic moment ${}^b\boldsymbol{\mu}$. Given the external magnetic field has magnetic flux density ${}^b\boldsymbol{B}$, the torque affecting satellite can be calculated from a simple formula:

$$\boldsymbol{\tau_m} = {}^b\boldsymbol{\mu} \times {}^b\boldsymbol{B}. \tag{3.17}$$

The same phenomenon occurs in compass and forces its needle to always point towards the magnetic north.

Earth is surrounded with magnetic field that can be approximated by the field of magnetic dipole. Magnetic potential satisfies Laplace equation and can be expanded

into series of spherical harmonics. International Geomagnetic Reference Field model (IGRF) model (see Sec. 4.1) does exactly that and provides periodically updated spherical coefficients that allow calculating value of magnetic flux density ${}^{b}\boldsymbol{B}$ for a specific point in time and space in the vicinity of the Earth. However, the Earth's magnetic field is very vulnerable to the randomly occurring solar magnetic storms which undermines practical applicability of this and similar models. Fortunately, in case of magnetic torque engineers have full control authority over satellites magnetic moment ${}^{b}\boldsymbol{\mu}$. As seen from (3.17), this allows eliminating the problem by adding permanent magnet to trim the net moment to zero. Some spacecraft are even designed to take advantage of this torque. Other worth mentioning influences on a spacecraft's attitude resulting from presence of external magnetic field are torque resulting from Eddy currents and magnetic-hysteresis torque[10]. The former is result of electrical currents being induced by the movement of conducting parts of satellite in magnetic field. As those conductors have less than infinite conductivity the rotational energy is slowly dissipated in form of resistive hating. The latter influence occurs when high-hysteresis materials inside spacecraft have their magnetic domains shifted because of the spinning flux vector. This process dissipates kinetic energy of satellite spin in form of heat due to the friction created when domains rotate inside the material[11].

Internal Momentum Torque

According to the principle of conservation the angular momentum around the centre of satellite's mass is constant. This is of course true when no propulsion is used and there are no external torques present. However, it is worth noting that scientific instruments and communication antennas that require precise attitude control are usually mounted on the external structure of a satellite. Any non-uniformly moving, especially spinning, parts of satellite can cause their misalignment despite the fact that net momentum of the whole spacecraft does not change. Because space inside rocket fairing is limited satellites very often have some deployable elements. Those may include solar panels, communication antennas and gravity gradient booms. Extending those devices causes force opposite to the one used for deployment and applied to the structure of the satellite. Moreover, satellite effectively changes its shape which affects position of centre of mass and changes spacecraft's moment of inertia[12]. Every spinning element of a spacecraft contributes to the net spin ratio. When spin rate of an element changes, the rest of the spacecraft also changes its angular velocity to preserve net momentum.

[10] Both of them can act as momentum damping factors in spin-stabilized satellites.

[11] Hysteretic materials are sometimes intentionally used in form of custom shaped hysteresis rods to provide passive momentum damping [31, 21]. It serves the purpose of detumbling spacecraft at the beginning of mission just after it has been ejected from the rocket payload compartment.

[12] Part of spacecraft that obviously needs to move around is fuel. It rapidly travels inside fuel system when propulsion is needed. It also moves inside fuel tank. Because of the state of weightlessness it does not simply settle inside the tank, but rather sticks to its inner walls and moves in a complicated fashion stimulated by every move of the spacecraft. Navier-Stokes equation are nearly impossible to solve analogically for real life boundary conditions. For this reason fuel sloshing is currently often modelled with finite-element methodology [65].

Mass Expulsion Torque

Perhaps most obvious source of trajectory and attitude change is mass expulsion. Cold gas thrusters are commonly used to propel and stabilize larger spacecraft. There are, however, other cases where mass expulsion might occur.

Unintentional mass expulsion may happen when spacecraft experiences a leak or venting. Hole in a spacecraft fuel or life support system can cause gas or liquid to rapidly leave the spacecraft providing unwanted thrust[13]. This problem rarely affects nanosatellites, as few of them carry liquid fuel on board.

Radiation Thrust Torque

Radiation torque is not a significant factor for nanosatellites. Some large satellites carry high power radio transmitters. Energy radiated away by typical communication satellite is on the order of several kilowatts. This radiation creates reaction force of approximately $0.33 \times 10^{-5}\,\mathrm{N\,kW^{-1}}$. Such satellites typically have long lifespan between 10 and 20 years, and therefore effects of this radiation trust need to be taken into account. With recent developments in field of high power lasers a Photonic Laser Thruster has been proposed. Basic idea assumes repeatedly bouncing high energy laser beam between two spacecraft It is theoretically possible to achieve thrust levels comparable to current chemical propellers, but with significantly higher specific impulse. Feasibility of this solution was demonstrated by Dr. Young K. Bae in December 2006.

3.2.4 Attitude control actuators

Some torque sources that contribute to satellite attitude disturbances can also be used in a controlled way to affect attitude of the spacecraft. Classification of most commonly used attitude actuators is shown in Fig. 3.12. For nanosatellites it is most common to utilize some combination of magnetic actuation and inertial sources of momentum (with the exception of control-moment gyros which are able to generate very high torques, but are heavy and cumbersome to use in small satellites). Attitude thrusters are less common, because they require fuel to be carried on board. Gravity gradient is sometimes used, for passively nadir pointing spacecraft. It is also impractical to utilize aerodynamic drag and solar radiation for attitude control.

[13]This happened during the famous Apollo 13 moon mission, when explosion caused a leak in oxygen tank of Service Module. Entire oxygen stored there vented into outer space over the course of the next 130 minutes. Fortunately, there was enough supplies left in spacecraft lunar module to bring the crew safely back to the Earth.

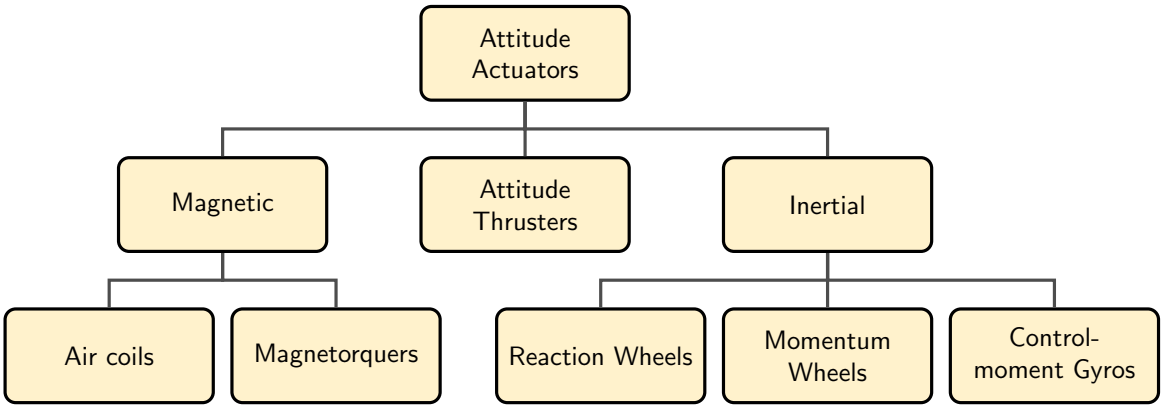

Figure 3.12: Classification of attitude control actuators

Magnetic actuators

Magnetic actuators are simple and reliable, because they do not require any moving parts. They use electrical power to interact with the Earth's magnetic field. Because torque is a cross product of magnetic dipole moment and ${}^{f}\boldsymbol{B}$ vector (3.17) it is only possible to provide two components of control torque (it is impossible to apply torque around the axis parallel to ${}^{f}\boldsymbol{B}$). This phenomenon is sometimes known as underactuation. Fortunately, for non-equatorial orbits magnetic ${}^{f}\boldsymbol{B}$ vector changes its direction as the satellite travels along the orbit. Therefore, with some limitations control over all three axes is possible [84].

Magnetorquers can be constructed as coils[14] of wire around the core. For smaller satellites coreless coils can be used. In the example shown in Fig. 3.13 it is clearly visible how the electric current generates the torque. Lorentz force is expressed by the

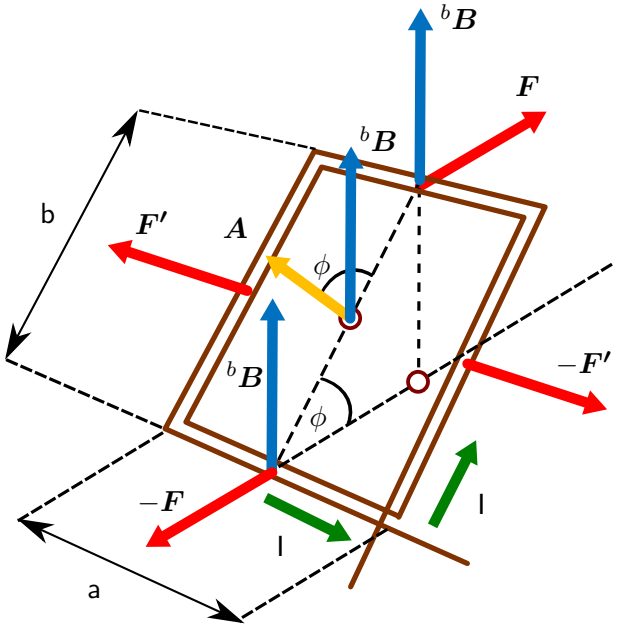

Figure 3.13: Lorentz forces acting upon the sides of a rectangular coil

[14] Usually two coils around the single core are used for redundancy.

relationship:

$$\boldsymbol{F} = L\boldsymbol{I} \times \boldsymbol{B}, \tag{3.18}$$

where $\boldsymbol{I}$ is the total electric current vector, L is length of the conductor, and $\boldsymbol{B}$ is the magnetic field vector. Coil in this example can be divided into four sides, two of length a, and two of length b. Vector $\boldsymbol{A}$ is a normal vector of the surface of the coil, and angle ϕ is the one between $\boldsymbol{B}$ and $\boldsymbol{A}$. As seen from Fig. 3.13 forces $\boldsymbol{F'}$ and $-\boldsymbol{F'}$ are balancing each other and forces $\boldsymbol{F}$ and $-\boldsymbol{F}$ equally contribute to the torque $\boldsymbol{T_1}$, which can be expressed with:

$$\boldsymbol{T_1} = 2F\frac{b}{2}\sin(\phi), \tag{3.19}$$

and equation (3.18) after applying to this situation takes the form:

$$\boldsymbol{F} = IaB. \tag{3.20}$$

Combining (3.19) and (3.20) gives:

$$\boldsymbol{T_1} = IabB\sin\phi = IAB\sin\phi, \tag{3.21}$$

or

$$\boldsymbol{T_N} = N\boldsymbol{I}\boldsymbol{A} \times \boldsymbol{B}, \tag{3.22}$$

for set of three identical orthogonally placed coils consisting of N loops of wire each. It is clearly seen that vector I consisting of three current values of each coil becomes the control variable.

Reaction and momentum wheels

Reaction and momentum wheels are used to exchange the momentum within the satellite. They cannot influence the net momentum of the spacecraft. In the present of non-zero-average external torques momentum exchange inside the spacecraft is not sufficient to control attitude, because momentum storages will eventually saturate. Therefore, some way of exchanging momentum with the environment is needed. Because of that many of the nanosatellites that need to actively control their attitude use reaction and/or momentum wheels together with magnetorquers. Momentum wheels enable three-axis attitude control and compensate for magnetic underactuation, and magnetorquers enable to desaturate the wheels.

3.2.5 Sattelite Attitude dynamics

The simplest possible model for attitude dynamics of a satellite is one assuming that the satellite is a rigid body. It is rarely a case, because most spacecraft contain moving or flexible parts. Also, larger satellites are usually equipped with thrusters for attitude or orbit control, and a liquefied fuel stored in tanks introduces a very complex dynamical properties. However, this simplification is justified for many small satellites. CubeSat specification prohibits the satellite to contain any pressurized gasses or liquids. Additionally some of the satellites lack moving parts, and are sufficiently small to assume that

structure of the satellite itself is not flexing significantly. Assuming that the body frame $\mathcal{F}_b$ is a principal axis frame attitude motion equations devised by Euler take form

$$I_{\hat{i}}{}^b\dot{\omega}_{\hat{i}} = (I_{\hat{j}} - I_{\hat{k}})^b\omega_{\hat{j}}{}^b\omega_{\hat{k}} + {}^b\tau_{\hat{i}}, \tag{3.23a}$$

$$I_{\hat{j}}{}^b\dot{\omega}_{\hat{j}} = (I_{\hat{k}} - I_{\hat{i}})^b\omega_{\hat{k}}{}^b\omega_{\hat{i}} + {}^b\tau_{\hat{j}}, \tag{3.23b}$$

$$I_{\hat{k}}{}^b\dot{\omega}_{\hat{k}} = (I_{\hat{i}} - I_{\hat{j}})^b\omega_{\hat{i}}{}^b\omega_{\hat{j}} + {}^b\tau_{\hat{k}}. \tag{3.23c}$$

Values of inertia along consecutive principal axes are represented with $I_{\hat{i}}$,$I_{\hat{j}}$, and $I_{\hat{k}}$. External torques are ${}^b\tau_{\hat{i}}$, ${}^b\tau_{\hat{j}}$, and ${}^b\tau_{\hat{k}}$ while the angular rates are ${}^b\omega_{\hat{i}}$, ${}^b\omega_{\hat{j}}$ and ${}^b\omega_{\hat{k}}$. If the attitude actuators do not expel fuel from the satellite they are not changing its inertia (e.g. see Sec. 3.2.4, the control torque can simply be included in the external torque values in (3.23). If actuation relies on momentum or reaction wheels (see Sec. 3.2.4, it is necessary to apply multi-spin model. It is also the case for some satellites that angular rate damping is present in the system[15]. Complete and thorough analysis of those, and even more complicated cases of attitude dynamics can be found in [28].

3.2.6 Attitude controllers

Various strategies of the satellite attitude control exist. First, it is worth mentioning that there is a possibility to make a satellite passively asymptotically stable in terms of orientation with utilization of external attitude torques. Various approaches are extensively described in [28]. In such a case a devices like passive magnets, aerodynamic stabilizers or gravity gradient booms are used to maximize selected torques and make a spacecraft pointed in the desired direction. Such a scheme requires a way of dissipating the torsional oscillations of the spacecraft, for which various damping devices are used. Those include magnetic hysteresis dampers (see [60]), or viscous fluid dampers (see [1]). One example design of a passive system based on a bar magnet and magnetic hysteresis rod is given in [24]. It is also possible, and often used in practice, to spin-stabilize a spacecraft [28]. Those and similar approaches eliminate the necessity of having an attitude controller altogether.

So far, for active attitude control of nanosatellites only magnetorquers and reaction wheels (see Sec. 3.2.4) have been used successfully. It is not possible to design a control system that solely uses the reaction wheels, as they only provide a way of exchanging the momentum between themselves and the satellite. Therefore, any integrating disturbance torque can eventually drive the wheels to their momentum storage limit. Designing a control system where the minimum of three reaction wheels are used for control of the attitude and three magnetorquers only to desaturate them is relatively simple[16], but the mass and volume needed for such a solution becomes quite significant in case of a nanosatellite. A configuration with single wheel and two magnetorquers was formulated in [13] utilizing a sliding mode controller. Solely magnetic approach has an obvious problem of one of the axis, collinear with the local magnetic field vector orientation, being uncontrollable. However, the direction of the magnetic field fortunatelly changes nearly periodically as the

[15] It is especially important for passively stabilised satellites.

[16] This can for example be done by using the reaction wheels as a primary attitude actuators, and the magnetorquers only to desaturate them.

satellite moves around the orbit[17]. First solution of the attitude control with three magnetorquers was proposed in [59] and was based on a infinite-time horizon Linear Quadratic Regulator (LQR). An energy optimal solution with use of Ricati periodic equation was formulated by Wisniewski in [83]. This problem has also been approached with Fuzzy controller in [71].

3.2.7 Attitude sensors

Attitude sensors provide measurements of the current attitude status. They can be divided into absolute sensors, that measure direction vectors, and relative ones, that measure rate of change of the attitude independently of external sources. External vectors that can be measured on board the satellite include Earth magnetic field vector, direction towards the Sun, stars, the Earth and other satellites. At least of two linearly independent direction vectors are needed to determine spacecraft attitude. Relative sensors are various types of rate gyroscopes. Classification of the attitude sensors is shown in Fig. 3.14. Accuracy

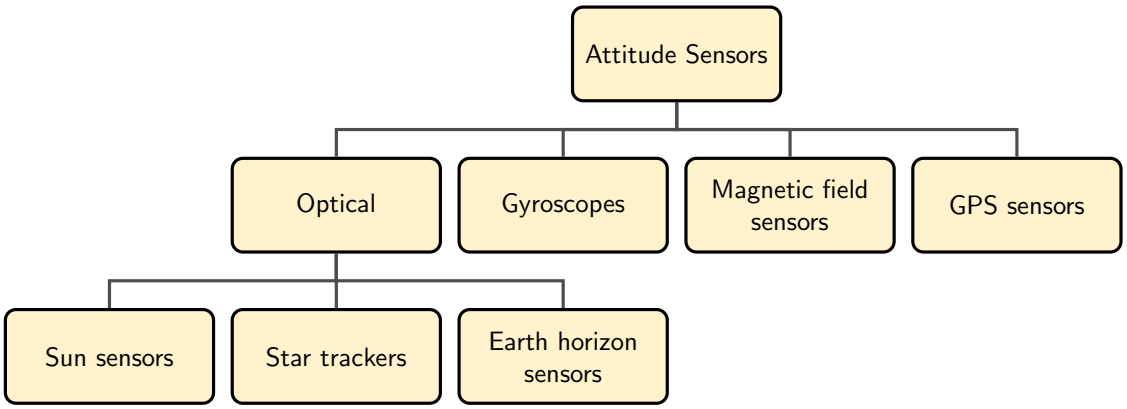

Figure 3.14: Classification of attitude sensors

of the attitude measurements is determined by precision of the sensors themselves, and on relative orientation of the measured vectors from absolute measurements. Sensor errors are subjected to systematic and random errors. The former class of errors is due to manufacturing offsets, imperfect calibration and secondary effects[18]. Random errors come from measurement noise and data representation errors.

Sun sensors

Sun sensors are designed to measure the Sun vector, which is a unit vector in BCF frame pointing in the direction of the Sun. Sun sensors can be divided into coarse (e.g. [54]) and fine (e.g. [100]) Sun sensors. According to [2] Sun sensors can measure Sun vector with high accuracy (0.01°), are reliable, stable at high rotation rates, and mainly applicable for sun pointing satellites because of limited field-of-view. On the other hand coarse

[17]This change is rather small for orbits with low inclination, which renders magnetic only attitude control extremely hard. Fortunately, nanosatellites rarely occupy this kind of orbit.

[18]E.g.: temperature.

Sun sensors are not very accurate (errors reaching even 15°!), however their simplicity, robustness negligible mass and power requirements make it ideal as emergency attitude sensor. Of course there is a lot of solutions that lie in between that are often used for small satellites.

Star trackers

Star sensors (see [91]) are dominant technology for spacecraft attitude determination. Star sensor consists of an optical telescope, a Charge Coupled Device (CCD) or Complementary Metal Oxide Semiconductor (CMOS) camera and sensor computer. Sensor works by comparing static image of the sky with an internal database of known stars. Initially, four star pattern is required to acquire the attitude information[19]. From that point sensor is able to measure the attitude in real time by tracking the star movements between consecutive frames. Main advantage of the sensor is that it provides three axis attitude knowledge with tremendous precision. Accuracy is determined by focal length (typically 30 mm to 50 mm), pixel resolution (around 0.02°), signal strength and number of processed stars [2]. It is, however, sophisticated and expensive piece of hardware. Some small devices of this kind exists, that can be used on board nanosatellites when high pointing precision is essential.

Earth horizon sensors

Earth horizon sensors (e.g. [104, 95, 96]) detect horizon of the Earth in the thermal infrared at around 15 µm. They can be divided into static sensors that are designed to have Earth permanently in the field of view[20], or scanning sensors that constantly look for the horizon. Main sources of error for this type of sensor is the fact that radiation distribution is irregular, and line between the horizon and outer space is fuzzy because of the atmosphere. This is particularly seen on low orbits, where most of the small satellites operate. Secondly, Earth oblateness makes it more difficult to recreate true direction towards centre of the planet based only on the partial picture of its contour. Also, as for all optical sensors thermal vibration is an issue. Earth horizon sensors are not very commonly employed on for nanosatellites, although some solutions of this kind have been proposed (see [43]).

Gyroscopes

Main principle behind gyroscopes is the measurement of rotation in the inertial frame of reference. Depending on the construction and underlying principle they can provide relatively high resolution measurements. However, as any relative measurement they are subjected to drift over time. Main classes of gyroscopes include mechanical gyroscopes,

[19] This is sometimes referred to as "lost in space" scenario.

[20] For example for satellites placed on Geostationary Earth's orbit (GEO), which often point at the Earth.

Fiber Optic Gyro (FOG) [105, 103], Ring Laser Gyro (RLG) [89] and Micro Electro-Mechanical System (MEMS) [75].

GPS sensors (for attitude)

GPS sensors (see [101, 98]) are not commonly used for attitude determination of small spacecraft. The main reason is that they require at least three GPS antennas (with Low Noise Amplifiers) placed relatively far away from each other[21]. Furthermore, antennas need to have unobstructed view of the same GPS satellites without shadowing or reflection. Those conditions are not easy to meet on board a small satellites.

3.2.8 Attitude estimation

Vector measurements taken on board the satellite are related to the reference values of those vectors expressed in the inertial frame with

$$^{\boldsymbol{b}}\boldsymbol{b_n} = {}^{i}_{b}A\,{}^{\boldsymbol{i}}\boldsymbol{r_n} + \boldsymbol{\delta b_n}, \tag{3.24}$$

where $^{\boldsymbol{b}}\boldsymbol{b_n}$ is a n-th measured normalized vector in the body frame, $\boldsymbol{\delta b_n}$ is the vector measurement error, and $^{\boldsymbol{i}}\boldsymbol{r_n}$ is n-th normalized reference vector. Approximated values of reference vectors are known from pertinent models, tables or almanacs. When the measurements and models of the corresponding pairs of vectors $\boldsymbol{\delta b_n}$ and $^{\boldsymbol{i}}\boldsymbol{r_n}$ at the same moment of time are available[22] it is possible to estimate the attitude matrix. This is of course provided that two of the available pairs are not collinear in relationship with each other.

Least squares estimate of satellite attitude

As proposed by Wahba [79] problem of estimating attitude of the spacecraft can be formulated as computation of the least squares attitude matrix ${}^{i}_{b}A$ with $\det({}^{i}_{b}A) = 1$, which minimizes the following cost function:

$$L({}^{i}_{b}A) = \frac{1}{2}\sum_{n=1}^{n_{max}} c_n \left\| {}^{\boldsymbol{b}}\boldsymbol{b_n} - {}^{i}_{b}A\,{}^{\boldsymbol{i}}\boldsymbol{r_n} \right\|_2^2, \tag{3.25}$$

where $^{\boldsymbol{b}}\boldsymbol{b_n}$ for $n = 1, .., n_{max}$ is a set of unit vector observations in reference frame tied to the spacecraft (e.g. BCF), and $^{\boldsymbol{i}}\boldsymbol{r_n}$ for $n = 1, .., n_{max}$ is a set of actual (modelled) values of those unit vectors with respect to the primary reference frame, to which the attitude is referred (e.g. ECF). The coefficients denoted by c_n are positive weights. A necessary and sufficient condition for a unique minimizing attitude matrix to exist is that at least

[21] On the order of 1.5 m according to [2].

[22] The minimum of two such pairs are needed to estimate the orientation in a 3D space.

two of the measured vectors are not parallel (or anti-parallel). It is often convenient to write the loss function $L({}^i_bA)$ as:

$$L({}^i_bA) = \lambda_0 - \mathrm{tr}({}^i_bAB^\top), \tag{3.26}$$

where:

$$\lambda_0 = \sum_{n=1}^{n_{max}} c_n, \tag{3.27}$$

and attitude profile matrix B:

$$B = \sum_{n=1}^{n_{max}} c_n {}^{\boldsymbol{b}}\boldsymbol{b_n}\,{}^{\boldsymbol{i}}\boldsymbol{r_n}^\top. \tag{3.28}$$

This form of the equation can be derived by transforming (3.25). Let us substitute formula under the sum in (3.25) by a scalar w_n, equal to:

$$w_n = c_n \left\| {}^{\boldsymbol{b}}\boldsymbol{b_n} - {}^i_bA\,{}^{\boldsymbol{i}}\boldsymbol{r_n} \right\|_2^2. \tag{3.29}$$

Knowing that:

$${}^{\boldsymbol{b}}\boldsymbol{b_n} - {}^i_bA\,{}^{\boldsymbol{i}}\boldsymbol{r_n} = \begin{bmatrix} b_{n,1} - a_{11}r_{n,1} - a_{12}r_{n,2} - a_{13}r_{n,3} \\ b_{n,2} - a_{21}r_{n,1} - a_{22}r_{n,2} - a_{23}r_{n,3} \\ b_{n,3} - a_{31}r_{n,1} - a_{32}r_{n,2} - a_{33}r_{n,3} \end{bmatrix}, \tag{3.30}$$

one can write:

$$\begin{aligned} w_n = c_n[&(b_{n,1} - a_{11}r_{n,1} - a_{12}r_{n,2} - a_{13}r_{n,3})^2 \\ &+(b_{n,2} - a_{21}r_{n,1} - a_{22}r_{n,2} - a_{23}r_{n,3})^2 \\ &+(b_{n,3} - a_{31}r_{n,1} - a_{32}r_{n,2} - a_{33}r_{n,3})^2]. \end{aligned} \tag{3.31}$$

By expanding the squares and rearranging the formula from (3.31) we get:

$$\begin{aligned} w_n = c_n[&(b_{n,1})^2 + (b_{n,2})^2 + (b_{n,3})^2 \\ &-2b_{n,1}(a_{11}r_{n,1} + a_{12}r_{n,2} + a_{13}r_{n,3}) \\ &-2b_{n,2}(a_{21}r_{n,1} + a_{22}r_{n,2} + a_{23}r_{n,3}) \\ &-2b_{n,3}(a_{31}r_{n,1} + a_{32}r_{n,2} + a_{33}r_{n,3}) \\ &+(a_{11}r_{n,1})^2 + (a_{21}r_{n,1})^2 + (a_{31}r_{n,1})^2 \\ &+(a_{12}r_{n,2})^2 + (a_{22}r_{n,2})^2 + (a_{32}r_{n,2})^2 \\ &+(a_{13}r_{n,3})^2 + (a_{23}r_{n,3})^2 + (a_{33}r_{n,3})^2 \\ &-2r_{n,1}r_{n,2}(a_{11}a_{12} + a_{21}a_{22} + a_{31}a_{32}) \\ &-2r_{n,1}r_{n,3}(a_{11}a_{13} + a_{21}a_{23} + a_{31}a_{33}) \\ &-2r_{n,2}r_{n,3}(a_{12}a_{13} + a_{22}a_{23} + a_{32}a_{33})]. \end{aligned} \tag{3.32}$$

As ${}^{\boldsymbol{b}}\boldsymbol{b_n}$ is a unit vector the following equality holds:

$$(b_{n,1})^2 + (b_{n,2})^2 + (b_{n,3})^2 = {}^{\boldsymbol{b}}\boldsymbol{b_n}^\top {}^{\boldsymbol{b}}\boldsymbol{b_n} = 1. \tag{3.33}$$

It is also possible to rearrange another part of (3.32) that is dependent on ${}^{\boldsymbol{b}}\boldsymbol{b_n}$ by using the following formula:

$$\begin{aligned} 2\,\mathrm{tr}(A{}^{\boldsymbol{b}}\boldsymbol{b_n}{}^{\boldsymbol{i}}\boldsymbol{r_n}{}^{\top}) =& 2\,\mathrm{tr}\Big({}^{i}_{b}A \begin{bmatrix} b_{n,1}r_{n,1} & b_{n,1}r_{n,1} & b_{n,1}r_{n,1} \\ b_{n,2}r_{n,2} & b_{n,2}r_{n,2} & b_{n,2}r_{n,2} \\ b_{n,2}r_{n,3} & b_{n,2}r_{n,3} & b_{n,2}r_{n,3} \end{bmatrix}\Big) = \\ =& 2b_{n,1}(a_{11}r_{n,1} + a_{12}r_{n,2} + a_{13}r_{n,3}) \\ &+ 2b_{n,2}(a_{21}r_{n,1} + a_{22}r_{n,2} + a_{23}r_{n,3}) \\ &+ 2b_{n,3}(a_{31}r_{n,1} + a_{32}r_{n,2} + a_{33}r_{n,3}) \end{aligned} \tag{3.34}$$

Finally, the part of (3.32) independent of ${}^{\boldsymbol{b}}\boldsymbol{b_n}$ can be simplified into:

$$\left({}^{i}_{b}A{}^{\boldsymbol{i}}\boldsymbol{r_n}\right)^{\top}\left({}^{i}_{b}A{}^{\boldsymbol{i}}\boldsymbol{r_n}\right) = \begin{bmatrix} a_{11}r_{n,1} + a_{12}r_{n,2} + a_{13}r_{n,3} \\ a_{21}r_{n,1} + a_{22}r_{n,2} + a_{23}r_{n,3} \\ a_{31}r_{n,1} + a_{32}r_{n,2} + a_{33}r_{n,3} \end{bmatrix}^{\top} \begin{bmatrix} a_{11}r_{n,1} + a_{12}r_{n,2} + a_{13}r_{n,3} \\ a_{21}r_{n,1} + a_{22}r_{n,2} + a_{23}r_{n,3} \\ a_{31}r_{n,1} + a_{32}r_{n,2} + a_{33}r_{n,3} \end{bmatrix}. \tag{3.35}$$

As ${}^{\boldsymbol{i}}\boldsymbol{r_n}$ is by definition an unit vector and ${}^{i}_{b}A$ is the orientation matrix expression (3.35) equals to 1. Combining (3.32) with (3.33), (3.34), and (3.35) results in:

$$\begin{aligned} L({}^{i}_{b}A) &= c_n\left({}^{\boldsymbol{b}}\boldsymbol{b_n}{}^{\top}\cdot{}^{\boldsymbol{b}}\boldsymbol{b_n} - 2\,\mathrm{tr}({}^{i}_{b}A{}^{\boldsymbol{b}}\boldsymbol{b_n}{}^{\boldsymbol{i}}\boldsymbol{r_n}{}^{\top}) + ({}^{i}_{b}A{}^{\boldsymbol{i}}\boldsymbol{r_n})^{\top}({}^{i}_{b}A{}^{\boldsymbol{i}}\boldsymbol{r_n})\right) = \\ &= 2c_n\left(1 - \mathrm{tr}({}^{i}_{b}A{}^{\boldsymbol{b}}\boldsymbol{b_n}{}^{\boldsymbol{i}}\boldsymbol{r_n}{}^{\top})\right). \end{aligned} \tag{3.36}$$

This can be then used to substitute (3.29) in (3.25) to form:

$$w_n = \sum_{n=1}^{n_{max}} c_n\left(1 - \mathrm{tr}({}^{i}_{b}A{}^{\boldsymbol{b}}\boldsymbol{b_n}{}^{\boldsymbol{i}}\boldsymbol{r_n}{}^{\top})\right) = \sum_{n=1}^{n_{max}} c_n - \mathrm{tr}\left({}^{i}_{b}A\sum_{n=1}^{n_{max}} c_n{}^{\boldsymbol{b}}\boldsymbol{b_n}{}^{\boldsymbol{i}}\boldsymbol{r_n}{}^{\top}\right), \tag{3.37}$$

and combined with (3.27) and (3.28) finally gives (3.26). It is worth noting that minimizing cost function $L({}^{i}_{b}A)$ is equivalent to maximizing value of the matrix trace from (3.26).

Q-Method

Davenport suggested the first practical method for solving the Wahba's problem and determining the spacecraft attitude [30, 38, 82, 50]. This idea includes combining equation (2.26) and (2.27) into:

$$\begin{aligned} \boldsymbol{q_v} &= \boldsymbol{a}\sin\frac{\Phi}{2}, \\ q_4 &= \cos\frac{\Phi}{2}. \end{aligned} \tag{3.38}$$

That representation is then used to parametrize attitude matrix A by a unit quaternion [44]:

$${}^{i}_{b}A(q) = (q_4^2 - |\boldsymbol{q_v}|^2)I + 2\boldsymbol{q_v}\boldsymbol{q_v}{}^{\top} - 2q_4[\boldsymbol{q_v}\times], \tag{3.39}$$

where $[\boldsymbol{q_v}\times]$ is a cross product matrix:

$$[\boldsymbol{q_v}\times] = \begin{bmatrix} 0 & -q_3 & q_2 \\ q_3 & 0 & -q_1 \\ -q_2 & q_1 & 0 \end{bmatrix}, \tag{3.40}$$

and (3.39) is another form of (2.28) from page 17. By additionally defining 3×1 vectors $\boldsymbol{z}$ and $\boldsymbol{\sigma}$, and square 3×3 matrix S:

$$\begin{aligned} S &= B + B^\top, \\ \boldsymbol{z} &= \sum_{n=1}^{n_{max}} c_n({}^{\boldsymbol{b}}\boldsymbol{b_n} \times {}^{\boldsymbol{i}}\boldsymbol{r_n}), \\ \boldsymbol{\sigma} &= \mathrm{tr}(B), \end{aligned} \tag{3.41}$$

it is possible to form a 4×4 matrix K:

$$K = \begin{bmatrix} S - \boldsymbol{\sigma} I & \boldsymbol{z} \\ \boldsymbol{z}^\top & \boldsymbol{\sigma} \end{bmatrix}. \tag{3.42}$$

As shown in [30], with additional assumption (without loss of generality) of sum of c_n for $n = 1, .., n_{max}$ equal to 1, matrix K and (3.39) can be used to obtain another form of weighted Wahba problem from (3.25):

$$L(q) = \frac{1}{2} \sum_{n=1}^{n_{max}} c_n \left\| {}^{\boldsymbol{b}}\boldsymbol{b_n} - {}^{i}_{b}A {}^{\boldsymbol{i}}\boldsymbol{r_n} \right\|^2 = 1 - q^\top K q, \tag{3.43}$$

which is dependent on attitude quaternion q instead of attitude matrix ${}^{i}_{b}A$. Problem of minimizing weighted Wahba loss function $L(q)$ is therefore equivalent to maximizing the quadratic form of q quaternion[23]. Problem of finding stationary values of that quadratic form on the unit sphere[24] can be solved using the Lagrange's method [66, pp. 276-278], namely by finding values of q that satisfy the necessary Kuhn-Tucker conditions for Lagrange function

$$\mathcal{L}(q, \mu) = q^\top K q + \mu q^\top q, \tag{3.44}$$

where μ is a Lagrange multiplier. It turns out that this is equivalent to the eigenvalue problem, and eigenvector of K associated with the largest eigenvalue is optimal, and minimizes $L(q)$ given by (3.43).

Outline of the current state of the art in attitude estimation is given in Sec. 3.3

[23] Treated as a 4×1 vector.

[24] When $\|q\|_2 = 1 \Leftrightarrow q^\top q = 1$.

3.3 Existing solutions of estimating the orientation

Over the years many algorithms have been proposed. Approaches vary depending on the chosen attitude representation [69]. As proven by Euler in his rotation theorem, arbitrary rotation may be described by only three parameters. However, as pointed out by [74], in order to achieve globally continuous and non-singular representation of the rotation it is necessary to employ at least four components.

There are some attitude determination algorithms based on singular, non redundant rotation representations. Minimal representation EKF based on Euler angles [22], Rodrigues parameters [29], and modified Rodrigues parameters [17] have been proposed. Since Grace Wahba formulated her least squares attitude determination problem (3.25), many algorithms, such as TRIaxial Attitude Determination (TRIAD) [7], unconstrained least-squares [9, 48], Fast Optimal Attitude Matrix (FOAM) [46], Singular Value Decomposition (SVD) [45], and Kalman-based approaches such as Matrix Kalman Filter (MKF) [5, 47] were created to directly estimate the attitude matrix.

As attitude matrix has as many as six redundant components, quaternions became a popular way of representing attitude. Following Davenport's Q-method solution to Wahba's problem, which translated it to quaternion representation, many quaternion algorithms have been proposed. Generally they can be divided into two groups: those that solve the least-squares problem, and those based on minimum variance approach (Kalman filtering). First group includes single frame algorithms, for example: QUaternion ESTimator (QUEST) [70], EStimator of Optimal Quaternion (ESOQ) [55] and other relying on recursive strategy, like Extended QUaternion ESTimator (EQUEST) [62]. Second group includes, but is not limited to: Multiplicative Extended Kalman Filter (MEKF) [37] and Additive Extended Kalman Filter (AEKF) [4]. Additionally, there are some batch algorithms that rely on storing a certain number of past measured samples to improve the present estimate. The example of such an approach can be Backward-Smoothing Extended Kalman Filter (BSEKF) [63]. Short summary of the selection of attitude determination algorithms is presented in Tab. 3.2.

[1]First applied in MAGSAT mission in 1979 is the most commonly used algorithm for solving Wahba problem according to [49].

[2]Filter QUEST and REQUEST are mathematically equivalent, however REQUEST is computationally more expensive.

[3]Wahba problem, see Sec. 3.2.8.

[4]Kalman filter solution of QUEST.

[5]Kalman filtering.

Table 3.2: Classification of spacecraft attitude determination methods

Method	Parametrization	Based on	Type	References
TRIAD	attitude matrix	WP[3]	single frame	[7]
ULS	attitude matrix	WP[3]	single frame	[9],[48],[49]
Q-method	quaternion	WP[3]	single frame	[30][82, pp. 420-428][49]
QUEST[1]	Rodrigues par.	WP[3]	single frame	[70],[49]
ESOQ	quaternion	WP[3]	single frame	[55],[49]
ESOQ2	Euler angle/axis	WP[3]	single frame	[57],[56],[49]
FOAM	attitude matrix	WP[3]	single frame	[46],[49]
SVD	attitude matrix	WP[3]	single frame	[45],[49]
EQUEST	quaternion	unique	recursive	[62]
filter QUEST	quaternion	KFQ[4]	recursive	[68]
REQUEST[2]	quaternion	KFQ[4]	recursive	[3],[14, pp. 160-161]
OPREQ	quaternion	KFQ[4]	recursive	[14, pp. 68-93],[15]
Min. rep. EKF	Euler angles	KF[5]	recursive	[22]
Min. rep. EKF	Rodrigues par.	KF[5]	recursive	[29]
Min. rep. EKF	modified RPs	KF[5]	recursive	[17]
MEKF	quaternion	KF[5]	recursive	[58],[37]
MEKF	attitude matrix	KF[5]	recursive	[47]
AEKF	quaternion	KF[5]	recursive	[4],[16]
AEKF	attitude matrix	KF[5]	recursive	[5]
BSEKF	not defined	KF[5]	batch	[63]

Chapter 4

Reference models

This work aims to verify the proposed attitude estimation scheme in realistic nanosatellite scenario. Therefore, a particular set of sensors is proposed for the verification experiments presented in Ch. 6. In order to perform the necessary simulations it is necessary to use models of the geomagnetic field, Sun position and visibility. Therefore, a short description of the used magnetic model is given in Sec. 4.1 and the Sun related models are presented in Sec. 4.2.

4.1 Geomagnetic field

The geomagnetic field model most commonly used in the aerospace is International Geomagnetic Reference Field model [20]. It describes the scalar potential of the magnetic field V at a selected point around the Earth defined with the spherical coordinates

$$V(r_s, \Theta, \lambda, t) = R_E \sum_{n=1}^{n_{max}} \left(\frac{R_E}{r_s}\right)^{n+1} \sum_{m=0}^{n} \left(g_n^m(t) \cos m\lambda + h_n^m(t) \sin m\lambda\right) P_n^m(cos\Theta), \quad (4.1)$$

where R_E is the mean equatorial radius of the Earth, r_s is the distance from the Earth centre, Θ is co-latitude and λ is longitude positive East. Terms $P_n^m(\cdot)$ represent the Schmidt quasi-normalized Legendre associated functions. From this scalar potential model the ${}^{\perp}\boldsymbol{B}$ vector of the magnetic field can be derived according to the equation (4.2). Model is defined by the coefficients g_n^m and h_n^m which are published, together with their time derivatives, by International Association of Geomagnetism and Aeronomy (IAGA) every five years. Magnetic scalar potential can be used to calculate the ${}^{\perp}\boldsymbol{B}$ magnetic vector as follows

$${}^{\perp}\boldsymbol{B} = \nabla V. \quad (4.2)$$

It is worth noting than ${}^{\perp}\boldsymbol{B}$ vector is classically defined in the NED reference frame dependent on the spherical coordinates of the point in space (see Sec. 2.1.6. Neither using spherical coordinates for the model input nor this NED output reference frame is convenient when performing satellite simulations. Therefore, a necessary frame conversions usually need to be applied.

IGRF-11 model is of order $n_{max} = 13$, therefore the calculations necessary to obtain the value if the ${}^{i}\boldsymbol{B}$ vector are relatively computationally expensive. Effort has been undertaken by the author of this thesis to provide a way of reducing the model order while sustaining the information on ${}^{i}\boldsymbol{B}$ direction in the predefined space and time for a specific satellite missions. Results of this research can be found in [86].

4.2 Sun position and visibility

So called Sun vector is a unit vector describing direction of the Sun in satellite body reference frame. It is obviously dependent both on satellite attitude and on the position of the Sun in relationship with the satellite. This position is of course determined by the orbital movement of the Earth around the Sun and of the satellite movement around the Earth. Satellite orbital movement can be described with orbital parameters (see section Sec. 2.3) and the Sun position in relationship to Earth will be described in Sec. 4.2.1. It is important to note that Sun can, and often is eclipsed by the Earth which makes it impossible for the satellite sensors to observe its position. This effect varies with so called *beta angle*, which is defined as the angle between the Sun position vector originating in the centre of the Earth and the orbital plane (see Fig. 4.1). For beta angle of 90° Sun direction vector is perpendicular to the orbital plane, which guarantees that there are no eclipses. Angle of 0° causes the longest possible eclipse time for a particular orbit. Eclipse

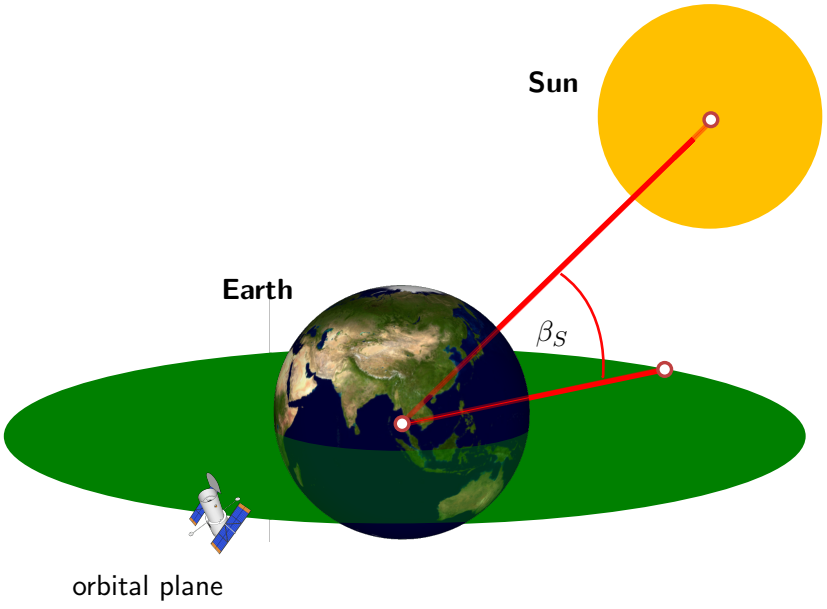

Figure 4.1: Sun beta angle

duration is also dependent on the attitude of the orbit. For circular orbit a contour plot of the eclipse duration depending on those two factors can be drawn, as seen in Fig. 4.2. For most orbits (except for the Sun synchronous orbits) this beta angle changes as the Earth travels around the Sun through the year. This causes the eclipse duration to vary with time. For example for a satellite on a circular orbit of 600 km altitude it can change from 0 to over 35 minutes as shown in Fig. 4.3. It is worth noting that due to the Sun-Earth

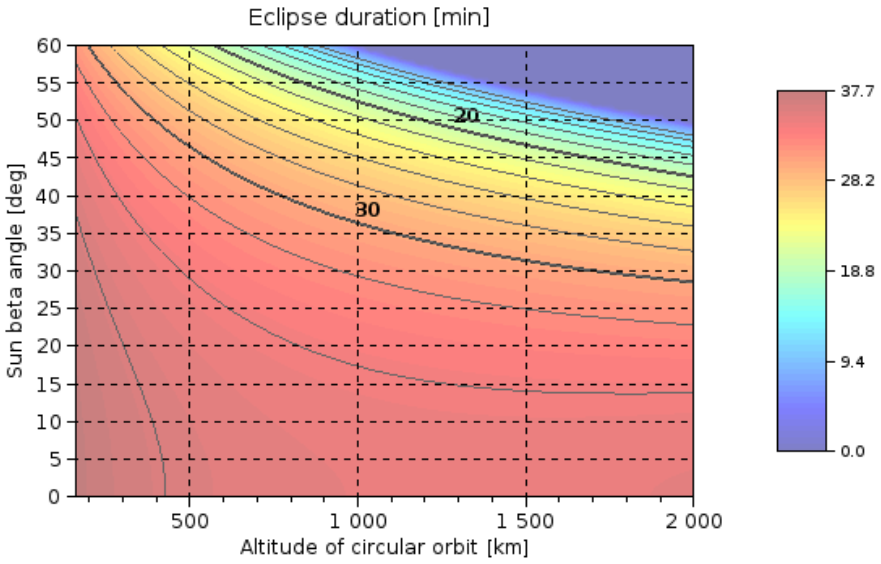

Figure 4.2: Impact of beta angle and satellite altitude on eclipse duration

system geometry full eclipse occurs when satellite travels in umbra region where the Sun is not visible from behind the Earth (see Fig. 4.4c). There is also a penumbra zone where only part of the Sun is hidden behind the Earth (see Fig. 4.4b). As the star is significantly larger than our planet at certain altitude full eclipse becomes impossible because Earth cannot obscure the entire Sun any more (this zone is called antumbra and can be seen in Fig. 4.4d). Those three situations are shown in Fig. 4.4 together with satellite point of view diagrams.

4.2.1 Sun position model

To determine Sun position with respect to Earth one needs to know parameters of the Earth orbit around the Sun represented in EOD reference frame (see section Sec. 2.1.5). Model proposed by J. Meeus in [51] allows calculating orbital elements of Earth-Sun system and will be used as a reference model in this research thesis. It is based on sidereal epoch $t_{mc0} = 2\,451\,545.0$ (12:00 AM, 1st January 2000). Model uses time measured in centuries since the epoch. Therefore, to calculate this time knowing sidereal time t_{jd} one can use the following (4.3):

$$t_{mc} = \frac{t_{jd} - t_{mc0}}{36\,525}, \tag{4.3}$$

where current sidereal time from epoch is divided by number of Julian days constituting a single century. Mean longitude Ω_0^S can be calculated with equation (4.4):

$$\Omega_0^S = l_0 + l_1 t_{mc} + l_2 t_{mc}^2, \tag{4.4}$$

where l_0, l_1 and l_3 are constant model coefficients. Mean anomaly ν_m^S is similarly described by equation (4.5) with constant model coefficients m_0, m_1, and m_2:

$$\nu_m^S = m_0 + m_1 t_{mc} + m_2 t_{mc}^2. \tag{4.5}$$

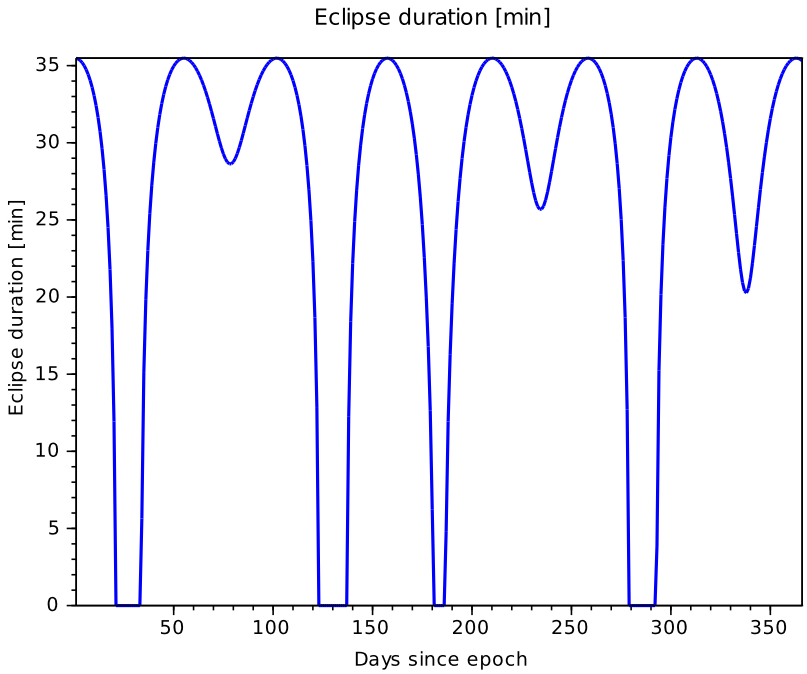

Figure 4.3: Evolution of eclipse duration over period of 365 days for a satellite on a 600 km orbit inclined at 60°

Eccentricity of Earth orbit e^E and Sun centre C are also modelled with respective equations (4.6) and (4.7):

$$e^E = k_0 + k_1 t_{mc} + k_2 t_{mc}^2, \tag{4.6}$$

$$C = (l_0^1 - l_1^1 t_{mc} - l_2^1 t_{mc}^2) \sin \nu_m^S + (l_0^2 - l_1^2 t_{mc}) \sin 2\nu_m^S + l_0^3 \sin 3\nu_m^S. \tag{4.7}$$

As can be seen form (4.4), (4.5), (4.6), and (4.7) parameters of Earth orbit around the Sun change over centuries. Equation (4.8)

$$\Omega^S = \Omega_0^S + C \tag{4.8}$$

allows calculation of the longitude of the ascending node of the Earth Ω^S. True anomaly ν_t^S of this orbit can be calculated with (4.9):

$$\nu_t^S = \nu_m^S + C. \tag{4.9}$$

Equation (4.10) describes the distance between the Sun and the Earth measured in astronomical units

$$r_E = \frac{1.000\,001\,018(1 - (e^E)^2)}{1 + e^E \cos(\nu_t^S)} \tag{4.10}$$

4.2.2 Conical shadow model

In most cases a satellite on LEO occasionally experiences condition where view of the Sun is fully or partially obscured. Eclipse occurs when spacecraft is passing over night side of the planet. Although shadow may be also cast by other bodies, such as the Moon,

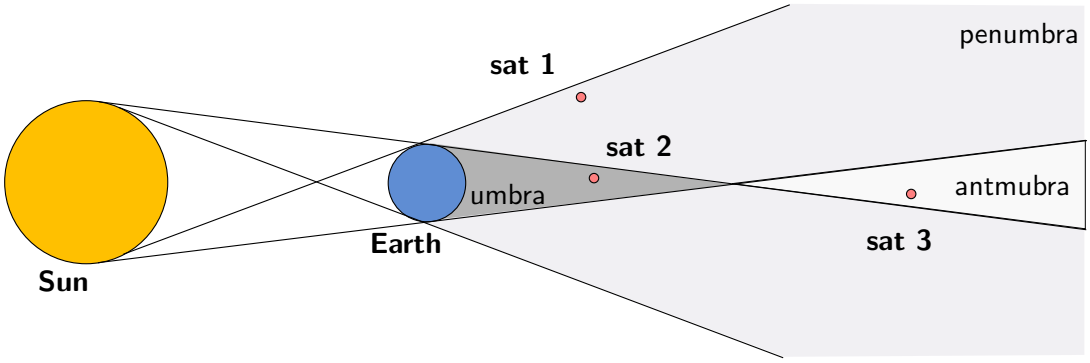

(a) Sun-Earth system

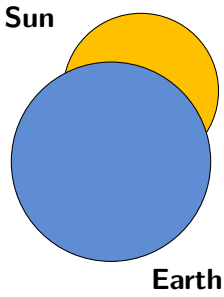

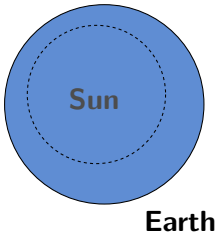

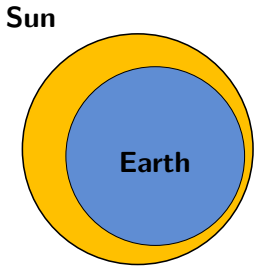

(b) Penumbra (seen by sat 1) (c) Umbra (seen by sat 2) (d) Antumbra (seen by sat 3)

Figure 4.4: Umbra, penumbra and antumbra (not to scale)

those events are less frequent, shorter and more difficult to predict. Detailed analysis of eclipse phenomenon in astronomy can be found in the book [39]. Assuming that Earth atmosphere and oblateness has minimal impact on eclipse occurrence conical shadow model, described in [53, 12] can be used to predict this condition. Diagram in Fig. 4.5 depicts basic geometry of Sun-Earth-Satellite system. Distance from the fundamental plane is described by (4.11)

$$s_0 = \frac{-\boldsymbol{r_s}^\top \boldsymbol{r_E}}{r_E} \tag{4.11}$$

Distance from the satellite to the shadow axis is described by (4.12)

$$l = l_1 + l_2 = \sqrt{r_s^2 - s_0^2} \tag{4.12}$$

Angles of the shadow cones are described by (4.13).

$$\begin{aligned} \sin \alpha_p &= \frac{R_S + R_E}{r_E} \\ \sin \beta_u &= \frac{R_S - R_E}{r_E} \end{aligned} \tag{4.13}$$

Angle α_p is related to the shadow cone of penumbra, and angle β_u is describing shadow cone of umbra. For Sun-Earth system those angles measure 0.264° and 0.269° respectively.

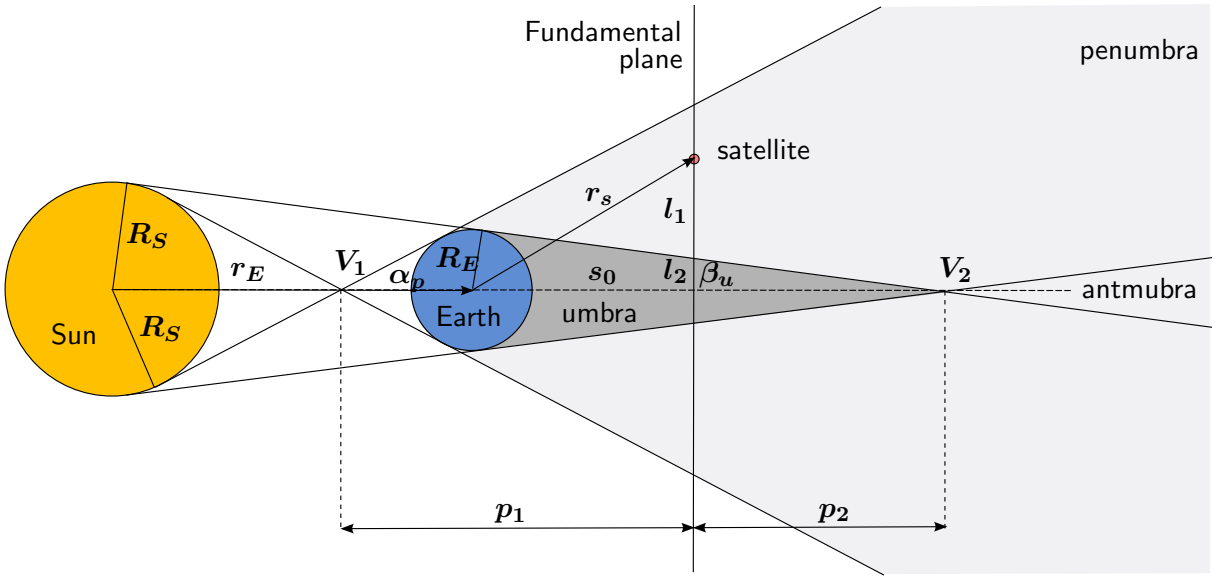

Figure 4.5: Conical shadow model (the Earth and the Sun not to scale)

Distances p_1 and p_2 can be calculated using (4.14):

$$\begin{aligned} p_1 &= \frac{s_0 + R_E}{\sin \alpha_p} \\ p_2 &= \frac{s_0 - R_E}{\sin \beta_u} \end{aligned} \tag{4.14}$$

Radii of both cones in the fundamental plane can therefore be calculated with (4.15):

$$\begin{aligned} l_1 &= p_1 \tan \alpha_p \\ l_2 &= p_2 \tan \beta_u \end{aligned} \tag{4.15}$$

Notice, that l_2 has a positive value between the Earth and the vertex of the umbral cone. Behind the vertex V_2 (which is situated 1.384×10^6 km from the Earth centre) apparent diameter of the Sun becomes larger than this of the Earth making complete eclipse impossible.

Chapter 5

Proposed attitude estimation method

This chapter contains the description of the proposed new SDQAE attitude estimator. Sec. 5.1 contains a generalized description of its structure taking into account a gyroscopic measurement with a bias estimation loop and any number of absolute attitude sensors. In the following Sec. 5.2 a specific case of the observer utilizing only two absolute attitude measurements of the magnetic field vector and Sun vector is outlined. Afterwards, Sec. 5.3 provides remarks on the attitude estimator tuning and Sec. 5.4 talks about its convergence properties. This last section also elaborates on an interesting observation, that despite some configurations with undesirable convergence properties exist for the two-sensor case it is possible to heuristically correct the estimate if it approaches them.

5.1 Attitude observer structure

The algorithm proposed in this section was inspired by the approach presented in [41], although lacks most of the simplifying assumptions that can be made if object does not move around the Earth with significant velocity.

One of the classical formulations of spacecraft attitude estimation is known as Wahba's problem [79]. It is defined as finding the orthonormal matrix ${}^{i}_{b}A$ which minimises the objective function described in Sec. 3.2.8 where orientation of the BCF frame in relation to ECI frame tied to the Earth is denoted by Direction Cosine Matrix ${}^{i}_{b}A$. A set of n direction measurements is considered, each of them is represented by 3×1 normalised vector in the Cartesian space. Those measurements are denoted as ${}^{\boldsymbol{b}}\boldsymbol{b_n}$ and expressed in the BCF. Let us reformulate the problem (see appendix Ch. C), with orientation expressed in terms of quaternion ${}^{b}_{i}\overline{q}$ instead of a matrix.

$$L({}^{b}_{i}\overline{q}) = \frac{1}{2}\sum_{n=1}^{n_{max}} c_n \left(f_n^{\top} f_n\right), \tag{5.1}$$

where:

$$f_n = {}^{\boldsymbol{b}}\overline{\boldsymbol{b}}_{\boldsymbol{n}} - {}^{b}_{i}\overline{q}^{*} \otimes {}^{\boldsymbol{i}}\overline{\boldsymbol{r}}_{\boldsymbol{n}} \otimes {}^{b}_{i}\overline{q}. \tag{5.2}$$

To allow for quaternion operations of vectors ${}^{\boldsymbol{b}}\boldsymbol{b}_{\boldsymbol{n}}$ and ${}^{\boldsymbol{i}}\boldsymbol{r}_{\boldsymbol{n}}$ they have to be extended to 4×1 vectors ${}^{\boldsymbol{b}}\overline{\boldsymbol{b}}_{\boldsymbol{n}}$ and ${}^{\boldsymbol{i}}\overline{\boldsymbol{r}}_{\boldsymbol{n}}$ by normalizing them and introducing additional 0 as the scalar element.

Problem (5.1) can be solved with many known optimisation methods. Perhaps the most effective one is the steepest descent algorithm, where k^{th} estimate ${}^{b}_{i}\hat{q}_k$ of orientation quaternion ${}^{b}_{i}\overline{q}_k$ is recursively improved based on its previous value ${}^{b}_{i}\hat{q}_{k-1}$ according to the equation:

$${}^{b}_{i}\hat{q}_k = \nparallel {}^{b}_{i}\hat{q}_{k-1} - KT_s\nabla L({}^{b}_{i}\hat{q}_{k-1}) \nparallel, \tag{5.3}$$

where $\nparallel \overline{q} \nparallel = \frac{\overline{q}}{\|\overline{q}\|}$. Subscript k refers to iteration number as well as discrete-time instant index ($t_k = kT_s$). The reason is, that only one iteration of optimisation algorithm is performed for each time step. This approach provides measurement noise filtering properties and considerably reduces computational burden. The gradient in (5.3) can be expressed as

$$\nabla L\left({}^{b}_{i}\hat{q}\right) = \frac{\partial L({}^{b}_{i}\hat{q})}{\partial \overline{q}} = \frac{\partial}{\partial \overline{q}}\left(\frac{1}{2}\sum_{n=1}^{n_{max}} c_n\left(f_n^{\top} f_n\right)\right). \tag{5.4}$$

Using the formula for derivative of a product, one can write

$$\frac{\partial}{\partial \overline{q}}\left(\frac{1}{2}\sum_{n=1}^{n_{max}} c_n\left(f_n^{\top} f_n\right)\right) = \frac{1}{2}\sum_{n=1}^{n_{max}} c_n\left(f_n^{\top}\frac{\partial f_n}{\partial \overline{q}} + \frac{\partial f_n}{\partial \overline{q}}^{\top} f_n\right). \tag{5.5}$$

After noticing that

$$f_n^{\top}\frac{\partial f_n}{\partial \overline{q}} = \frac{\partial f_n}{\partial \overline{q}}^{\top} f_n, \tag{5.6}$$

one can simplify the equation (5.4) to:

$$\nabla L({}^{b}_{i}\hat{q}) = \sum_{n=1}^{n_{max}} c_n\left(\frac{\partial f_n}{\partial \overline{q}}^{\top} f_n\right) = \sum_{n=1}^{n_n} c_n J(n)^{\top} f_n, \tag{5.7}$$

where Jacobi matrix is defined as

$$J({}^{b}_{i}\hat{q}) = \begin{bmatrix} \frac{\partial f_{n,1}}{\partial q_1} & \frac{\partial f_{n,1}}{\partial q_2} & \frac{\partial f_{n,1}}{\partial q_3} & \frac{\partial f_{n,1}}{\partial q_4} \\ \frac{\partial f_{n,2}}{\partial q_1} & \frac{\partial f_{n,2}}{\partial q_2} & \frac{\partial f_{n,2}}{\partial q_3} & \frac{\partial f_{n,2}}{\partial q_4} \\ \frac{\partial f_{n,3}}{\partial q_1} & \frac{\partial f_{n,3}}{\partial q_2} & \frac{\partial f_{n,3}}{\partial q_3} & \frac{\partial f_{n,3}}{\partial q_4} \end{bmatrix}. \tag{5.8}$$

Value of gain K is set as a result of a trade-off between noise rejection capabilities (lower values of K) and convergence rate (higher values of K). If the satellite angular velocity equals zero and no noise is present in measurement signals, the estimate converges (with additional provisions – see Sec. 5.4). However, for a rotating satellite (5.3) cannot eliminate the steady-state estimation error. This goal may be achieved if a gyroscopic rate

measurement is available. Equation (5.3) can be then supplemented with a prediction term resulting from a kinematic differential equation

$$ {}^{b}_{i}\dot{\hat{q}} = \frac{1}{2} {}^{b}_{i}\hat{q} \otimes {}^{b}\overline{\boldsymbol{\omega}}, \tag{5.9} $$

yielding the following formula obtained by the Euler discretization of (5.9)

$$ {}^{b}_{i}\hat{q}_k = \nmid {}^{b}_{i}\hat{q}_{k-1} - KT_s \nabla L({}^{b}_{i}\hat{q}_{k-1}) + \frac{1}{2} T_s ({}^{b}_{i}\hat{q}_{k-1} \otimes {}^{b}\overline{\boldsymbol{\omega}}_k) \nmid . \tag{5.10} $$

The presence of the gyroscopic prediction term in (5.10) expands the range of admissible values for gain K. It eliminates the risk of convergence loss due to satellite spinning motion for small values of K.

MEMS rate gyroscope measurements are significantly burdened by the measurement bias. Practical attitude determination algorithm requires compensation of its effect. Gyroscope bias value usually strongly depends on the temperature it is experiencing. This becomes serious problem for small satellites which often have very simple thermal control systems and are not able to stabilise the temperature of the sensors, which are instead subjected to temperature cycles related to thee orbital cycle of the eclipses. Therefore, one solution is to constantly estimate the bias of the gyroscope and subtract this value from the measured angular rate applied to the algorithm

$$ {}^{b}\widehat{\boldsymbol{\omega}}_k = {}^{b}\overline{\boldsymbol{\omega}}_k - {}^{b}\widehat{\boldsymbol{\omega}}_{\boldsymbol{B}k}, \tag{5.11} $$

where ${}^{b}\widehat{\boldsymbol{\omega}}_k$ represents the unbiased rate estimate, and ${}^{b}\widehat{\boldsymbol{\omega}}_{\boldsymbol{B}k}$ is the bias estimate. In Kalman-based approaches (see Tab. 3.2 the bias can be estimated as an additional state in the system model. It is, however, possible to estimate it through the integral feedback of the error in rate of change in orientation as shown by Mahony *et al* [42]. Term $\nabla L({}^{b}_{i}\hat{q}_{k-1})$ present in equation (5.10) represents the error in the rate of change of orientation coming from the gyroscopic measurement. By analogy to (5.9) on can rearrange the rate of change formula to estimate the rate error

$$ {}^{b}\widehat{\boldsymbol{\omega}}_{\boldsymbol{E}k-1} = 2 {}^{b}_{i}\hat{q}^{*}_{k-1} \otimes \nabla L({}^{b}_{i}\hat{q}_{k-1}). \tag{5.12} $$

Bias ${}^{b}\widehat{\boldsymbol{\omega}}_{\boldsymbol{B}k}$ is a low frequency component of (5.12). In order to extract it an integral with gain $K_\omega \ll 1$ can be applied. Let us consider equation

$$ {}^{b}\widehat{\boldsymbol{\omega}}_{\boldsymbol{B},k-1} = K_\omega \sum_{p=0}^{k-1} 2T_s ({}^{b}_{i}\hat{q}^{*}_{p} \otimes \frac{\nabla L({}^{b}_{i}\hat{q}_p)}{\left|\left|\nabla L({}^{b}_{i}\hat{q}_p)\right|\right|}). \tag{5.13} $$

It involves simple integration approximation with Euler method of (5.12) where instead of $\nabla L({}^{b}_{i}\hat{q}_p)$ its normalized value was used and gain coefficient K_ω introduced. Using normalized value of the Wahba objective function instead of the function (5.1) changes convergence properties (quicker convergence), and forces the bias estimate to oscillate around the true value (sliding mode estimation) instead of approaching it asymptotically. Simulation had proved that the other approach also allows for bias estimation, but when minimizing angular orientation error is more important, the method presented in Fig. 5.1 yields slightly better results.

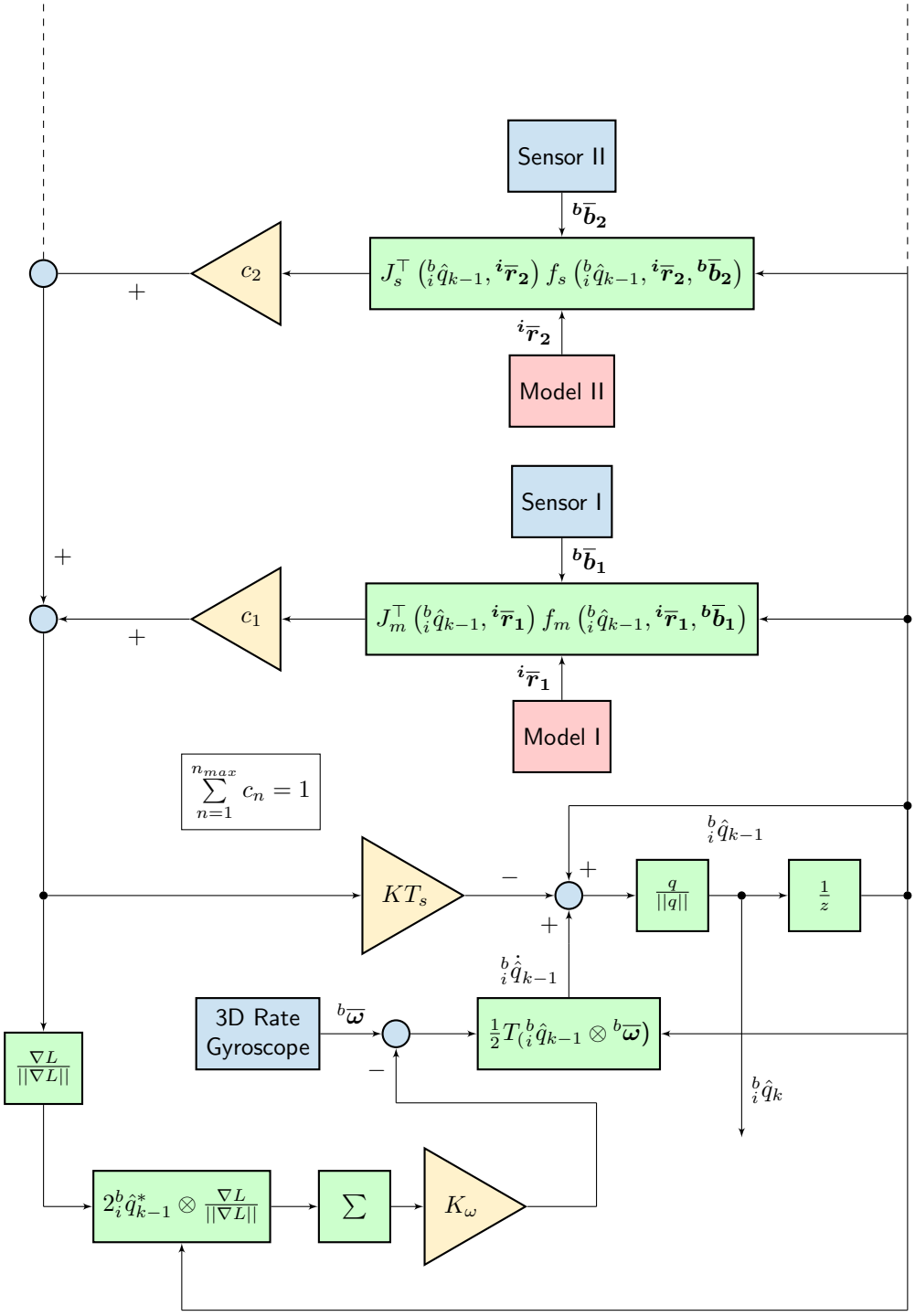

Figure 5.1: Block diagram of the proposed attitude estimator. Measurements from multiple sensors (Sensor I, Sensor II, ...) are compared with the corresponding models of the measured vectors (Model I, Model II, ...). Each of the n_{max} resulting correction terms is taken into account with a weight (c_1, c_2, ...). At each iteration the resulting sum of the weighted correction is applied in a steepest descent scheme with gain K. Prediction term resulting from the gyroscopic measurement is also used taking into account the estimated gyroscope bias.

5.2 The case study

Let us consider attitude determination problem that could be faced while designing very small satellite with strict mass, budget and energy constraints. In such a case the minimal set of sensor and low computational cost become essential. The magnetometer is used as a primary sensor securing an uninterrupted stream of data. It provides a normalised vector ${}^b\overline{\boldsymbol{m}}$. As a secondary sensor the Sun direction measurement system has been selected. It produces intermittent measurement represented by a normalised vector ${}^b\overline{\boldsymbol{s}}$.

Now it is possible to define function f_k in (5.2) for the ${}^b\overline{\boldsymbol{m}}$ vector as follows:

$$f_m\left({}^b_i\hat{q}, {}^i\overline{\boldsymbol{m}}, {}^b\overline{\boldsymbol{m}}\right) = {}^b\overline{\boldsymbol{m}} - {}^b_i\hat{q}^* \otimes {}^i\overline{\boldsymbol{m}} \otimes {}^b_i\hat{q}. \tag{5.14}$$

This problem finds its minimum when direction of the magnetic field vector ${}^i\overline{\boldsymbol{m}}$, modelled in the inertial frame and transformed by the orientation quaternion, is equivalent to magnetic field vector direction ${}^b\overline{\boldsymbol{m}}$, which is measured on board. The ${}^i\overline{\boldsymbol{m}}$ vector varies with time and satellite location but an accurate model of Earth magnetic field is available and can be incorporated into the observer algorithm. This problem of course has infinite number of solutions, as transformation around the direction of the measured magnetic field vector is not bounded in any way. One can make the solution unique by introduction of the second vector ${}^b\overline{\boldsymbol{s}}$ into the set of direction measurements. The corresponding f_k is expressed as:

$$f_s\left({}^b_i\hat{q}, {}^i\overline{\boldsymbol{s}}, {}^b\overline{\boldsymbol{s}}\right) = {}^b\overline{\boldsymbol{s}} - {}^b_i\hat{q}^* \otimes {}^i\overline{\boldsymbol{s}} \otimes {}^b_i\hat{q}, \tag{5.15}$$

where ${}^i\overline{\boldsymbol{s}}$ represents the Sun direction vector expressed in the inertial frame. Its dependence of time and satellite location is accounted for by a precise model. As previously shown the steepest descent optimisation algorithm can be used to solve the optimization problem (5.1). Addends on the right-hand side of (5.7) corresponding to f_m and f_s become:

$$c_m(J_m^\top f_m) = c_m J_m^\top({}^b_i\hat{q}, {}^i\overline{\boldsymbol{m}}) f_m({}^b_i\hat{q}, {}^i\overline{\boldsymbol{m}}, {}^b\overline{\boldsymbol{m}}), \tag{5.16a}$$

$$c_s(J_s^\top f_s) = c_s J_s^\top({}^b_i\hat{q}, {}^i\overline{\boldsymbol{s}}) f_s({}^b_i\hat{q}, {}^i\overline{\boldsymbol{s}}, {}^b\overline{\boldsymbol{s}}). \tag{5.16b}$$

Fig. 5.2 shows structure of the attitude estimator that implements (5.10) for gyroscopic, magnetic and Sun sensors.

Prediction term resulting from (5.9) is utilised by the algorithm shown in Fig. 5.2 by approximating the integral with Euler method. The presence of prediction loop not only allows for smaller values of K for better noise rejection, but is also crucial when the Sun direction measurement is not available. Thus, the availability of gyroscopic measurement makes the algorithm robust to periodic loss of Sun sensor data by limiting the estimator error growth rate.

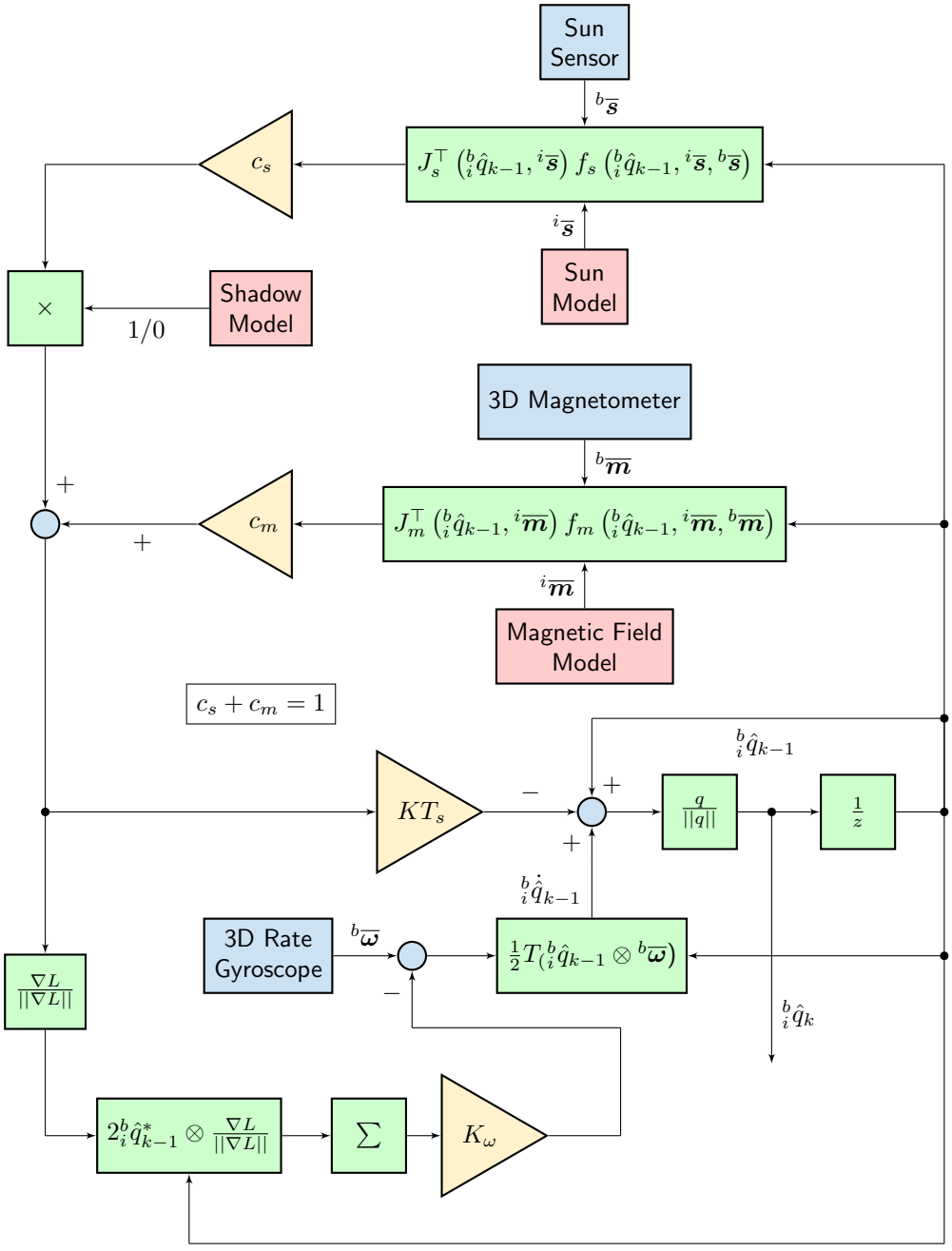

Figure 5.2: Block diagram of the exapmle implementation of the attitude estimator with magnetic, gyroscopic and Sun vector sensor. Measurements from the Sun Sensor ang 3D Magnetometer are compared with the corresponding models of the measured vectors (Magnetic Field Model, Sun Model). Each of the resulting correction terms is taken into account with a weight (c_s, c_m). At each iteration the resulting sum of the weighted correction is applied in a steepest descent scheme with gain K. Prediction term resulting from the gyroscopic measurement is also used taking into account the estimated gyroscope bias.

5.3 Remarks on tuning

5.3.1 Definition of the estimate error

To quantify the performance of the algorithm an angular error of the estimation can be used. Quaternion of rotation between the true and estimated orientation can be calculated as:

$$\delta_i^b\hat{q} = {}_i^b\overline{q}^* \otimes {}_i^b\hat{q}, \tag{5.17}$$

where ${}_i^b\overline{q}^*$ is equal to conjugate of the true orientation quaternion. $\delta_i^b\hat{q}$ represents the rotation that transforms the axes of the estimated body frame onto those of the true body frame. Then, the scalar element ${}_i^b\hat{q}_4$ of $\delta_i^b\hat{q}$ can be used to extract the Euler angle $\delta\theta$ between those two orientations with

$$\delta\theta = 2\arccos(\delta_i^b\hat{q}_4). \tag{5.18}$$

This is a very natural way of interpreting error, as it represents the angle between the real and the estimated orientation. For the Monte Carlo studies presented in Ch. 6 it is necessary to somehow average the error of all the simulation runs for every time index k. Therefore a mean Monte Carlo error is introduced:

$$\delta\theta_{MC}(k) = \sqrt{\frac{1}{r_{max}}\sum_{r=1}^{r_{max}}\delta\theta_{k,r}}, \tag{5.19}$$

where r is the index of the Monte Carlo run. However, if it is necessary to quantify error not at a single point in time, but rather estimate the quality of estimation trough the longer period it is necessary to introduce another quality indicator. In this work a Root Mean Square error (RMS) error is used, defined as

$$\delta\theta_{RMS} = \sqrt{\frac{1}{k_{max}r_{max}}\sum_{k=1}^{k_{max}}\sum_{r=1}^{r_{max}}\delta\theta_{k,r}^2}, \tag{5.20}$$

where k is the sample number. It has been selected, because it allows for comparison between the different attitude determination methods. The error itself has a clear interpretation, as it represents the sample error standard deviation. Additionally, thanks to the fact that it is measured in units of angle (e.g. degrees) it makes it possible to intuitively understand the magnitude of the algorithm error for a particular case. It is possible to calculate the sum in (5.20) not only for a single run of simulation, but for a multiple runs constituting a Monte Carlo experiment.

5.3.2 Gyroscope bias loop gain selection

Looking at (5.13) one can immediately notice that the bias estimate is changing each time by a constant bias magnitude. This is due to the fact that $\frac{\nabla L({}_i^b\hat{q}_p)}{\left\|\nabla L({}_i^b\hat{q}_p)\right\|}$ term is a normalized value of the correction for sample number p. In 3D space this change in bias estimate

is in the direction dictated by $\nabla L({}^{b}_{i}\hat{q}_p)$. Such a scheme was proposed by [42]. The fact that there is an absolute maximum amount of change that can occur each time the bias estimation loop is evaluated puts a constraint on the selection of K_ω. It needs to be large enough to keep with that change in the actual bias. If this value can be estimated by the examination of sensor properties and the conditions at which it operates[1] the $K_\omega^{\min}$ can be evaluated. On the other hand the bias estimator loop is subjected to noise due to the other measurements influence on ${}^{b}_{i}\hat{q}_p$. Smaller values of K_ω obviously provide better noise rejection capabilities. However, K_ω^{min} cannot be used, because not only the estimate has to keep up with the changes in bias, but also reach it relatively quickly even if it is moving away. For this reason a one-dimensional model of attitude estimator was implemented in Simulink in an attempt to gain additional insight into this problem. No analytical solution to gain selection was found, but experiments show that the rule of thumb of $K_\omega = K_\omega^{\min}$ can be generally used with bigger values decreasing the performance slowly, and smaller increasing the risk of the estimate not converging at all. Fig. 5.3 shows an example of the one-dimensional bias estimation scenario with noise removed for clarity of the plot. The blue line represents the true bias, in this example assumed to be a sinusoid. Red line is the bias estimate, black envelope shows the $\pm K_\omega^{\min}$, and green the maximal change of the estimate (roughly two times larger).

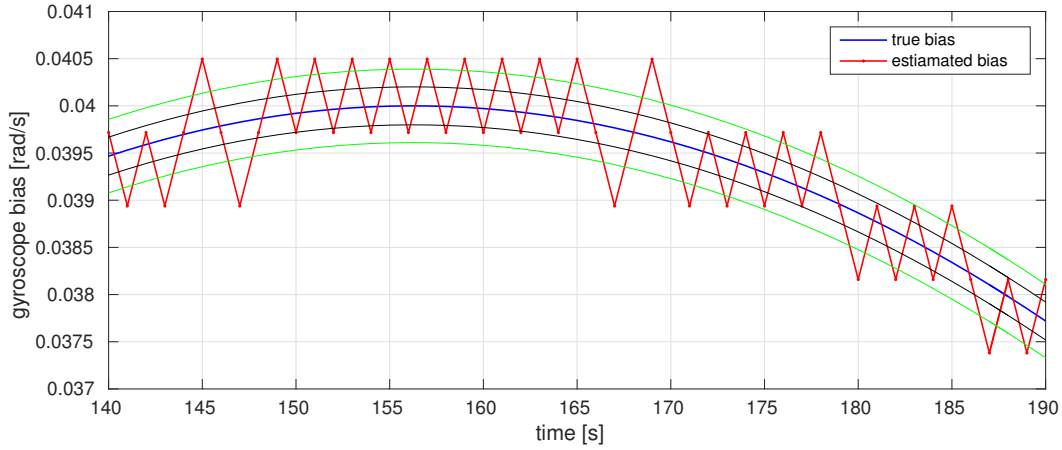

Figure 5.3: Bias estimate evolution example

5.3.3 Sensor weights selection

According to [67] in order to achieve maximum likelyhood estimation in Wahba's problem (3.25) the sensor weights should take form

$$c_n = \frac{1}{\sigma_n^2}, \tag{5.21}$$

where σ_n is the standard deviation of a particular sensor. Because quaternion problem (5.1) is equivalent to (3.25) it follows immediately that the same rule applies. However, one has to remember that SDQAE makes an additional assumption that $\sum c_n = 1$. This

[1] For example the maximum gyroscope temperature deviation from sample to sample.

is not a problem, becuase proper scaling factor can be included in the K parameter. Unfortunately, the condition presented in (5.21) does not apply to the situation where one of the sensors is periodically unavailable or the sampling rates for sensors are different. This is the case for all of the studies presented in this thesis, therefore instead an optimization is used to find appropriate values of sensor weights c_n as well as the algorithm gains.

5.3.4 Optimization based weights and gain tuning

An optimization approach of SDQAE estimator tuning assumes the objective function based on the RMS error described with the equation (5.20). When tuning the algorithm for a specific satellite it would make sense to calculate this objective function for a fragment of the planned orbit of this its particular mission. As such a simulation requires additional inputs, such as: initial orientation estimate, noise and bias values of each of the sensors it is also sensible to calculate the RMS error not over a single run of the simulation, but rather for several runs, with different randomized values of those variables. Optimized parameters are: the estimator gain K, bias loop gain K_ω, and c_n coefficients (one for each of the absolute attitude sensors). This results in size of the optimization problem equal to $n_{max} + 2$, where n_{max} is the number of absolute attitude sensors. A *Nelder-Mead simplex direct search*[2] algorithm was used, which additional provisions to guarantee the $\sum c_n = 1$ criterion.

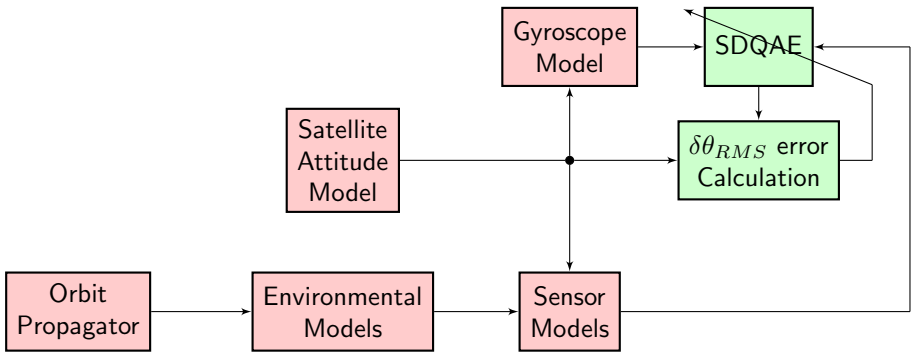

Figure 5.4: The SDQAE observer tuning setup

Obviously, calculating the value of the objective function is far from trivial. The optimization process is depicted in Fig. 5.4. First it is necessary to calculate the satellite position through the simulation with Orbital propagator. This operation takes as inputs the parameters of the orbit and the initial simulation time. Next, the satellite position is fed to the models of the values measured by the corresponding attitude sensors (e.g. Sun vector, magnetic vector, star direction, nadir direction, ...). Afterwards the reference values of the measured vectors are fed to the sensor models. Those take into account the measurement errors. In case of sensors studied in this thesis see Sec. 6.2. The satellite attitude also needs to be modelled and used to rotate the modelled measurements to the satellite body frame. In this work a simple models are used of a satellite rotating with constant velocity around a random (see Sec. 6.4.2 or predefined axis (see Sec. 6.4.1). Both

[2]Standard implementation of Nelder–Mead simplex method[34] algorithm available in MATLAB.

the modelled (an rotated) measurements and the modelled values are fed to the SDQAE estimator. At the same time they are also fed to the Error Calculation block, which calculates the objective function.

5.4 Remarks on convergence properties

Algorithm convergence from any initial quaternion estimate should be guaranteed. Understandably, this property cannot be achieved when one of the ${}^{i}\boldsymbol{s}$ and ${}^{i}\boldsymbol{m}$ measured vectors is unavailable. The same is true when they are collinear. Unfortunately, there are other configurations which, in theory, can prevent the estimate from converging. Fig. 5.5 shows four identified cases, where the steepest descent term described with equation (5.3) does not correct the attitude estimate. This happens because the correction term is either zero or collinear with the estimated attitude quaternion. In case of (a) this is desired as it represents the correct attitude estimate, but the remaining ones correspond to the estimation error of 180°.

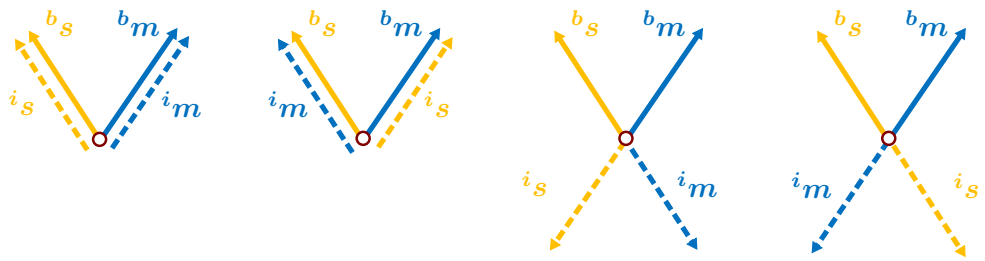

(a) (b) (c) (d)

Figure 5.5: Magnetic (blue) and Sun (yellow) vectors configuration for desirable (a) and undesirable (b, c, d) configurations (solid line – vectors measured in $\mathcal{F}_b$ frame, dash line – vectors obtained from models expressed in $\mathcal{F}_i$ and transformed to $\mathcal{F}_b$ according to ${}^{b}_{i}\hat{q}$ estimate)

In practice there are several factors that prevent this problem from persisting for a prolonged period of time:

- dependence of ${}^{i}\boldsymbol{s}$ and ${}^{i}\boldsymbol{m}$ vectors on time,
- sensor bias and noise,
- gyroscope bias estimation term,
- differential equation discretisation error,
- numerical errors due to the finite representation precision.

If none of those factors was present, the estimate error $\delta\theta$ could remain at 180° indefinitely. However, simulations show that setting the estimate in one of those spurious configurations

and eliminating previously mentioned factors except for the numerical and discretisation errors still causes the estimate to converge.

Interestingly, situations shown in Fig. 5.5 can be detected on board the satellite without the knowledge of the true attitude. The objective function $L({}_i^b\hat{q}_k)$ in (5.1) and the rate of its change in time $\Delta L({}_i^b\hat{q}_k) = L({}_i^b\hat{q}_k) - L({}_i^b\hat{q}_{k-1})$ can be monitored as an undesirable configuration indicator (see Tab. 5.1). Alternatively ${}_i^b\hat{q}$ and $\nabla L({}_i^b\hat{q}_k)$ can be used. For undesirable configurations $\nabla L({}_i^b\hat{q}_k)$ is large and almost collinear with orientation estimate while for the correct attitude estimate it almost vanishes. Values of f_s, f_m, ${}^b\boldsymbol{m}$, and ${}^b\boldsymbol{s}$ can be used to distinguish between them. Furthermore, if desired, it is even possible to apply a heuristic attitude estimate correction algorithm, by rotating the estimate by 180° around the predetermined axis and thus bringing the estimate near the correct value. Values of those corrections for each of the undesirable configurations are presented in Tab. 5.1 in terms of Euler axis and angle od rotation.

Table 5.1: Criteria for special configurations detection, discrimination and correction

configuration	detection L	detection ΔL	discrimination	correction axis	correction angle
desirable (a)	≈ 0	≈ 0	$f_m \approx f_s \approx 0$	–	–
undesirable (b)	$\gg 0$	≈ 0	$f_m \approx -f_s$	${}^b\boldsymbol{m} + {}^b\boldsymbol{s}$	180°
undesirable (c)	$\gg 0$	≈ 0	$f_m \approx f_s$	${}^b\boldsymbol{m} - {}^b\boldsymbol{s}$	180°
undesirable (d)	$\gg 0$	≈ 0	$f_m \approx 2^b\boldsymbol{m}$ $f_s \approx 2^b\boldsymbol{s}$	${}^b\boldsymbol{m} \times {}^b\boldsymbol{s}$	180°

Another consideration that needs to be taken into account is the angle between the measured vectors ${}^b\boldsymbol{m}$ and ${}^b\boldsymbol{s}$. As shown in study Sec. 6.4.1 when only the gyroscopic measurement and one reference vector measurement is available the algorithm is not able to correct the growing error in the rotation around that vector. However, it is also possible that measured vectors are collinear, in which case a similar problem arises. In case of two sensors (e.g. the Sun sensor and magnetometer) this situation occurs when the magnetic field lines are parallel to the sun direction vector. If we assume that magnetic field around the Earth can be approximated with this of a magnetic dipole (see Sec. 4.1) this situation only occurs at certain points in the plane containing the Sun centre and the line connecting the magnetic poles of the Earth. Even if the satellite orbit lies in that plane it will reach points of collinearity only four times per one cycle as shown in Fig. 5.6. As those configurations are infrequent and of short duration, they do not pose significant problems in practice.

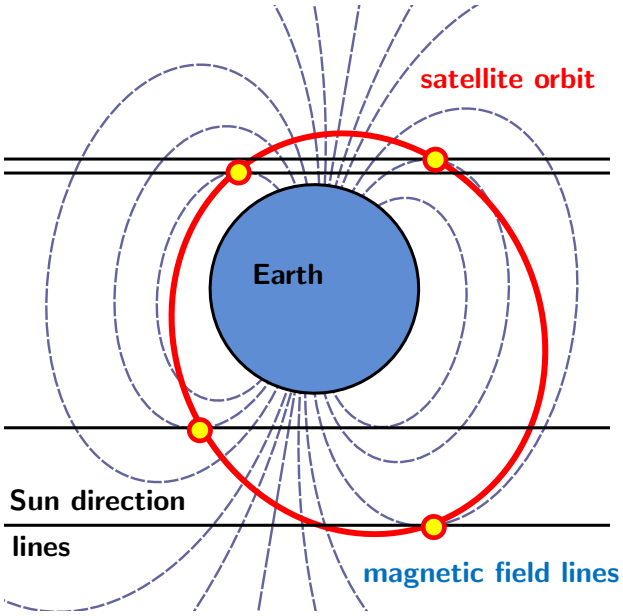

Figure 5.6: Magnetic field is parallel to the Sun direction only in four points even for an in-plane orbit

Chapter 6

Verification of the solution

While designing attitude estimator it is obviously impractical or even impossible to conduct its on-orbit verification experiments. On the other hand, it is necessary to ensure its reliability and high performance under diverse environmental conditions. Hence, computer simulations and hardware-in-the-loop testing are often employed as a part of the development process. In the following chapter the former approach is addressed.

Sec. 6.1 presents a complete heterogeneous and flexible verification platform. The environment provides a comprehensive set of tools including environmental models, trajectory propagators, satellite attitude dynamics simulators and data analysis and visualisation interfaces. The tool set combines advantages of various software packages including MATLAB/Simulink [90], Scilab [93], Aerospace Blockset (AB) for Xcos [87], and CelestLab [88] to present the researcher with a complete, versatile and scalable solution.

On-board sensor models used for the simulation studies are presented in Sec. 6.2. The magnetometer, gyroscope, and Sun sensor are implemented in Simulink environment. Sec. 6.3 briefly points out the necessity to tune the sensors and identify their parameters. It also provides descriptions of procedures that can be used to accomplish that.

Finally, Sec. 6.4 presents the simulation experiments performed to verify the SDQAE observer performance. First, the Sec. 6.4.1 describes the case study performed as part of an effort of developing attitude estimation system for Lithuanica SAT-2 satellite that is scheduled to launch in early 2017 as part of QB50 multi-satellite atmospheric study mission [26]. Secondly, in Sec. 6.4.2 the new observer performance is compared against selected known solutions. Finally, Sec. 6.4.3 tests a unique feature of the proposed solution, namely, the ability to operate each of the attitude sensors at different sampling rate.

6.1 Simulation environment

A comprehensive description of the simulation environment used for the purpose of the following study can be found in [85]. It consists of several software tools, most importantly CelestLab and Aerospace Blockset [87] available in the Scilab environment, and in-house developed packages running in Matlab/Simulink environment.

Scilab [11, 27] is a freely available [93] and open source software package for numerical computation providing a powerful and flexible environment for engineering and scientific applications. It is complemented with Xcos, which allows diagrammatic programming and is intended for design and simulation of hybrid (continuous and discrete time) dynamical system models. Those two tools are free alternative to commercial MATLAB/Simulink [64] package. Scilab/Xcos offers many functionalities that can be used for professional purposes. Due to the open source nature Scilab/Xcos also allows adding third party toolboxes. Most of them are also open source and freely available from [92]. Particularly interesting from the perspective of aerospace simulations are CelestLab library and AB for Xcos (see Fig. 6.1). The former consists of a comprehensive set of functions that enable

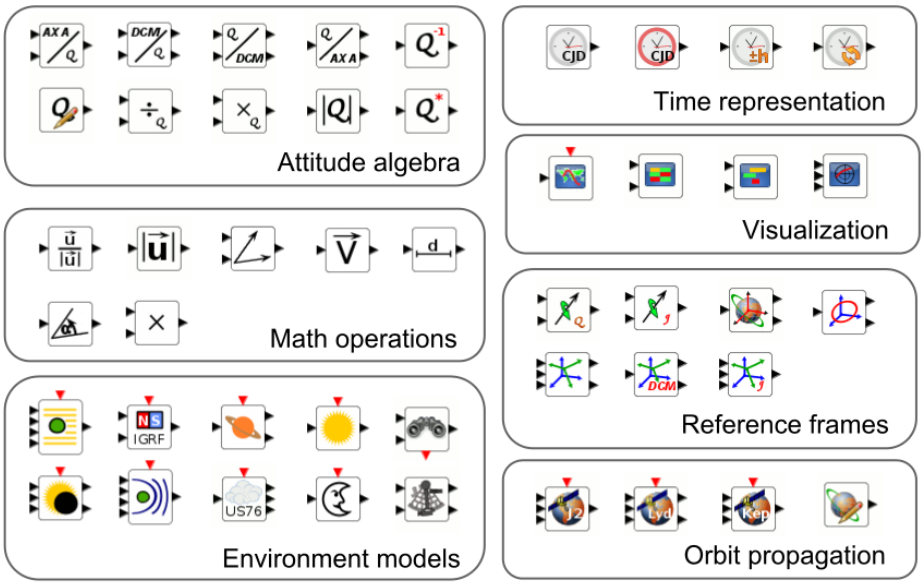

Figure 6.1: Selected Aerospace Blockset blocks grouped by feature

simulation of spacecraft trajectories and space environment. The library is developed by the Centre National d'Etudes Spatiales (the French Space Agency) and is tested against commercial software as well as real data gathered by space missions. The latter is a toolbox developed by the author of this thesis that encapsulates CelestLab functionalities into a user friendly set of Xcos blocks. Apart from ease of use it also provides input validation, both of which reduce the chance of human error while preparing the simulation.

All mentioned tools were used as important part of the proposed hybrid simulation environment. Orbital data for a given scenario were generated by propagating the satellite location and utilizing models of the Sun position, eclipsing and geomagnetic field. An example of such a scenario implemented in Aerospace Blockset is presented in Fig. 6.2.

Generated data were then stored in a file and used as an input for subsequent attitude observer tests. Despite the fact that Scilab, CelestLab and Aerospace Blockset provide

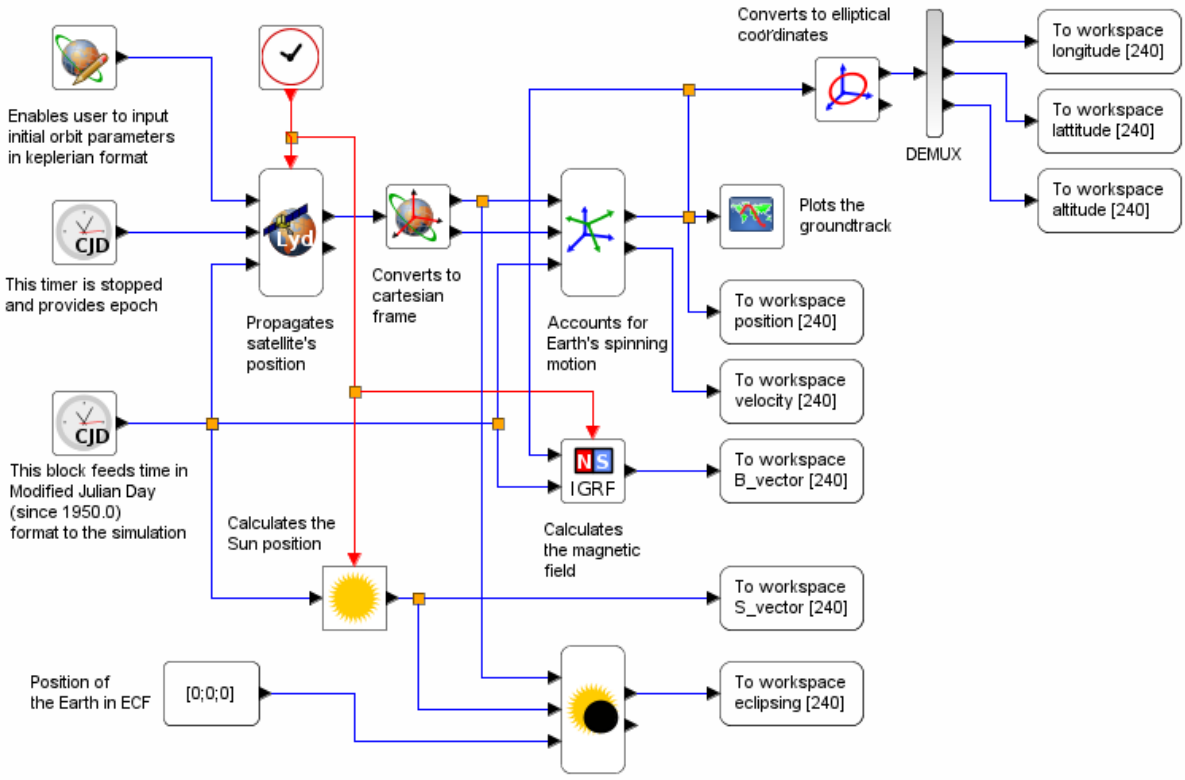

Figure 6.2: Aerospace Blockset diagram used to generate the orbital environment data

a very reliable ways of performing aerospace calculations they do not offer a necessary level of flexibility and computational performance when it comes to performing attitude estimation testing. Therefore, this task was performed within MATLAB and Simulink environment (see Fig. 6.3). Simulink was used for satellite attitude dynamics modelling and attitude observer simulation. MATLAB scripts could then be used to call the Simulink diagram multiple times to statistically asses performance of the investigated attitude estimator and its parameters. Data could be then visualised and used for further tuning as needed. For attitude estimators testing it was usually justifiable to assume that the spacecraft trajectory does not depend on its orientation. In such a case, the simulation could be ran multiple times using orbital environmental data generated only once for each scenario which saved execution time. The simulation environment, apart from the usual plotting capabilities, provided a graphical user interface used to visualize the simulation progress. For example the window shown in Fig. 6.4 was designed to provide overview of current satellite orbit, position, orientation, attitude estimate and measurements status directly from Simulink model. Initial tests showed that such comprehensive knowledge is crucial for prototyping and initial stages, because it allows easy detection of errors in the modelling process and visual assessment of the attitude estimation performance.

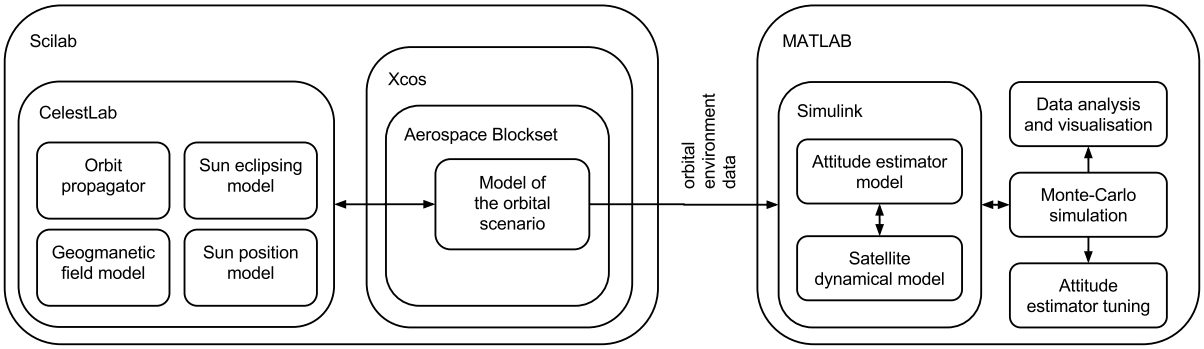

Figure 6.3: Diagram of the hybrid simulation environment

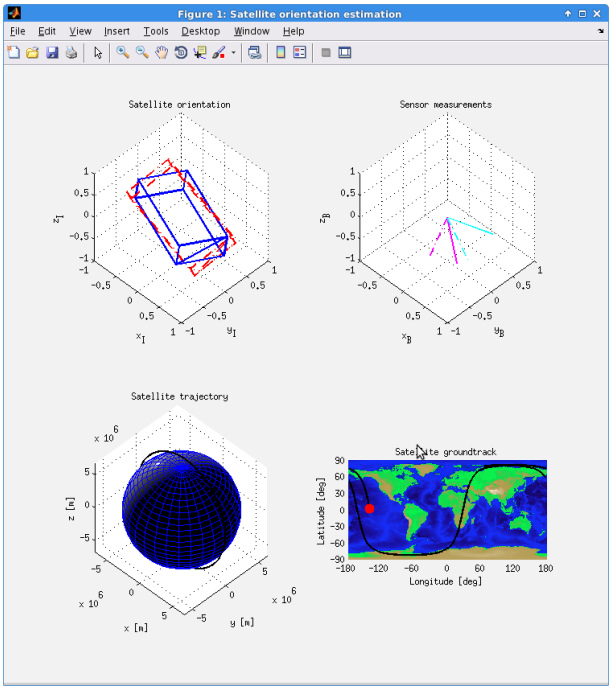

Figure 6.4: Visualisation of the attitude estimator test simulation

6.2 Sensor models

To validate the custom attitude determination algorithms in the simulation testbed adequate models of used sensors are needed. The most common sensors used for estimating attitude on board of nano- and picosatellites are: magnetic field vector sensor, Sun direction vector sensor and angular rate gyroscope. Major factors that have to be taken into account in sensor modelling in order to reflect the real digital sensor parameters are: bias, measurement noise, quantisation effect, sensor dynamics and auxiliary internal digital filter dynamics. Also, the mechanical properties and dimension of certain parts of the sensors need to be identified. A brief description of the calibration challenges is presented in the following sections.

6.3 Sensor calibration and parameters identification

6.3.1 Magnetometer calibration

Methods of calibration of the magnetic field sensors are thoroughly described in [8]. In this thesis the following model is used for the calibration purposes

$$ {}^{b}\boldsymbol{m} = {}^{b}\boldsymbol{m}({}^{s}\boldsymbol{m}, \mathtt{t}_{sens}) = MK(\mathtt{t}_{sens}){}^{s}\boldsymbol{m} + \boldsymbol{b}(\mathtt{t}_{sens}), \tag{6.1} $$

where ${}^{b}\boldsymbol{m}$ is the calibrated measurement vector, M is the sensor axes misalignment matrix, K is the diagonal gain matrix dependent on sesnor temperature $\mathtt{t}_{sens}$ and $\boldsymbol{b}$ is the sensor bias vector. Value of the magnetic field is calculated based on the raw value of the measurement ${}^{s}\boldsymbol{m}$. It is assumed that the measurement is subjected to error mainly due to the gains of the sensor axes slightly differing from the nominal values declared by the sensor manufacturer. For this reason gain matrix has to be applied. Its value has to be determined during the calibration process. Documentation of the magnetoresistive sensors used in the following calibration experiments suggest that it is dependent on the sensor temperature. The HMC5883L [97] sensor uses elaborate internal hardware mechanism to account for the temperature changes. The MAG3110 [99], however, contains an additional temperature sensor and requires temperature compensation in the measurement software. It turns out that a simple linear temperature compensation scheme can be used, hence

$$ K = K(\mathtt{t}_{sens}) = K_{ref} + K_{temp}(\mathtt{t}_{sens} - \mathtt{t}_{ref}). \tag{6.2} $$

A reference temperature $\mathtt{t}_{ref}$ is selected arbitrarily, and additional diagonal matrix K_{temp} of temperature coefficients needs to be found. Similarly, the sensor bias vector is also approximated as being linearly dependent on temperature with the formula

$$ \boldsymbol{b} = \boldsymbol{b}(\mathtt{t}_{sens}) = \boldsymbol{b}_{ref} + \boldsymbol{b}_{temp}(\mathtt{t}_{sens} - \mathtt{t}_{ref}). \tag{6.3} $$

To calibrate the sensor it is necessary to have a reference measurement of the magnitude of the magnetic field m_{ref}. Then a magnitude of the calibrated measurement $\left\|{}^{b}\boldsymbol{m}\right\|$ should be equal to it, regardless of the sensor orientation. If a set of n measurements at different orientations is taken with ideal sensor the measurement cloud in the 3D space should lie on a surface of a sphere with radius m_{ref} and centre at the origin of the reference frame. However, due to the measurement errors it is actually an ellipsoid (not counting the noise into account). An optimization problem can be formulated

$$ L_m(K, \boldsymbol{b}) = \sum_{i=1}^{n} (\|MK{}^{s}\boldsymbol{m} + \boldsymbol{b}\| - m_{ref})^2 \tag{6.4} $$

This optimization can be performed, and example result, without taking into account the temperature compensation, is shown in Fig. 6.5. The values of the magnitude of the raw measurement $\|{}^{s}\boldsymbol{m}\|$ and the calibrated measurement $\left\|{}^{b}\boldsymbol{m}\right\|$ is shown in Fig. 6.6. Comparison of the calibrated value $\left\|{}^{b}\boldsymbol{m}\right\|$ distribution is shown in Fig. 6.7. It is clear that due to the internal temperature compensation scheme the HMC5883L sensor gives a much smaller magnitude noise. If the temperature coefficients K_{temp} and $\boldsymbol{b}_{temp}$ are included into optimized parameters space the optimization for MAG3110 the results, shown in Fig. 6.8

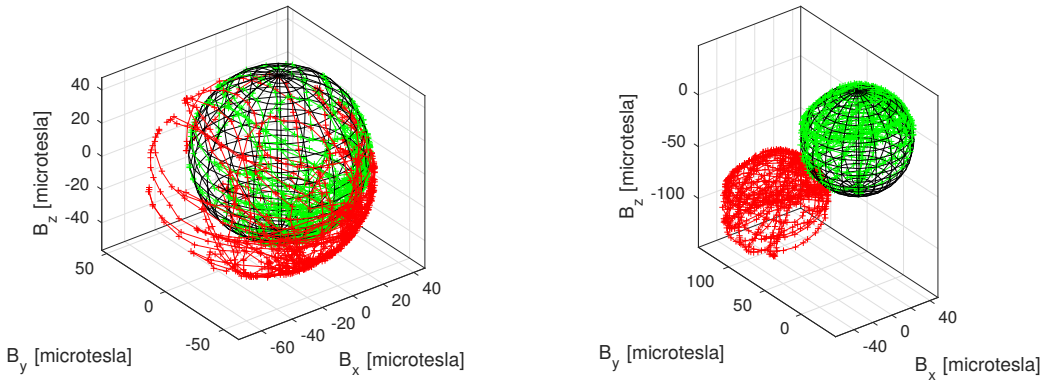

(a) HMC5883L (b) MAG3110

Figure 6.5: Magnetic field measurement points cloud before (red) and after calibration (green)

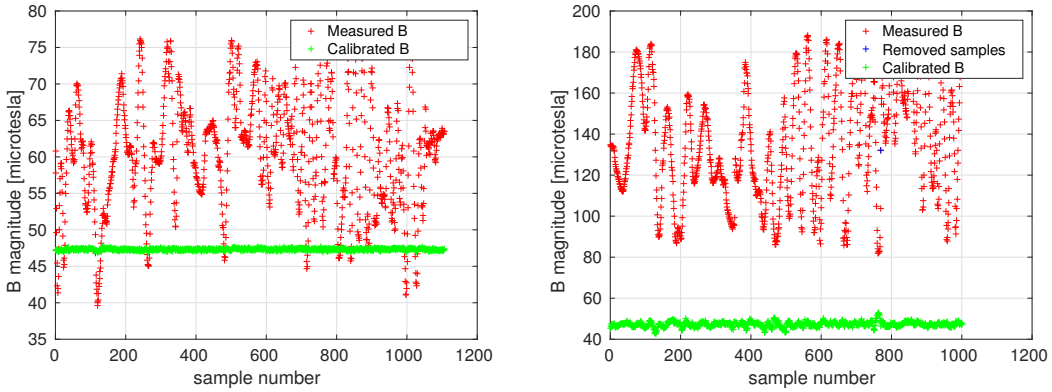

(a) HMC5883L (b) MAG3110

Figure 6.6: Measured magnetic field magnitude before (red) and after calibration (green)

show a significant improvement. Comparison of all three calibration experiments is shown in Tab. 6.1. It is worth noting that MAG3110 sensor noise was significantly reduced by introduction of temperature compensation (see standard deviation σ). However, the compensation mechanism present in HMC5883L sensor yields even better results. Looking at the results of temperature compensation it is apparent that bias drift due to temperature has much larger impact on the measurement that the scaling factor drift. A model of a single magnetometer axis used for the attitude determination experiments presented in Fig. 6.9 was implemented in Simulink.

[1]Sensors have different resolution per count, the presented gain is applied after converting the measurement to microtesla with nominal scaling factor.

[2]Offset is measured in counts, it is not comparable between HMC5883L and MAG3110 sensors.

[3]Two individual sensors of the same model are used in those experiments.

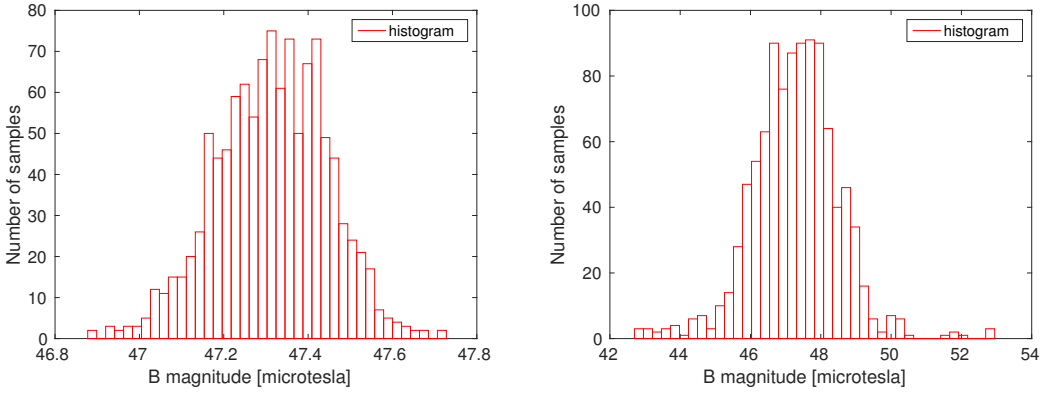

(a) HMC5883L (b) MAG3110

Figure 6.7: Histogram of the measured magnetic field magnitude

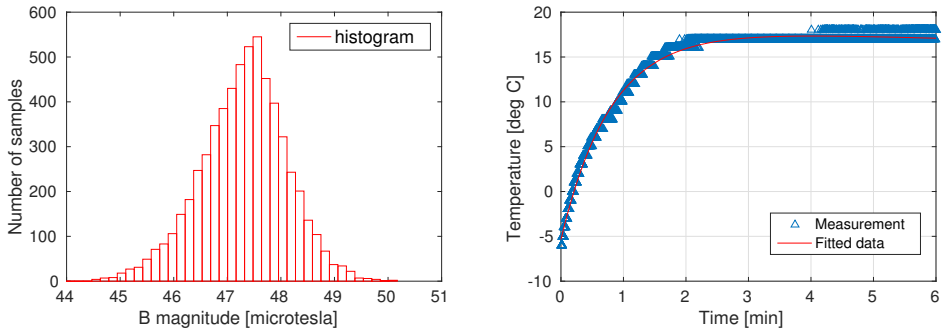

(a) (b)

Figure 6.8: Magnetometer calibration with temperature correction. Histogram (a) shows the MAG3110 sensor calibration results with temperature correctionand plot (b) presents the sensor temperature change during the calibration experiment

6.3.2 Gyroscope calibration

The most difficult element of the angular rate sensor model is related to its internal dynamics. MEMS rate gyroscope sensor consists of a mass suspended on micro springs. Hence, the transfer function describing this mechanical system can be expressed as

$$G_{ms}(s) = \frac{\omega_n^2}{s^2 + 2\zeta\omega_n s + \omega_n^2}, \tag{6.5}$$

where ω_n is a natural frequency and ζ is a damping factor. Magnetometer dynamics can be usually neglected since the lack of mechanical elements results in time constants a few orders of magnitude shorter than in MEMS sensors case. Many methods od dynamical systems identiffication egsist (see e.g. [10]). In this case the sensor is optimized by the manufacturer speciffically to achieve very high natural frequency. Therefore, this part does not play a vital role for this application, and arbitrary values of ω_n and ζ can be used as long as they guarantee a small damping and phase shift for the lower frequencies. Although rate noise density of the gyroscope noise is always given in the sensor datasheet, its value for a particular sensor and low pass filter setting might be slightly different. This

Table 6.1: Calibration results

Device	HMC5883L	MAG3110[3]	MAG3110[3] at 17 °C	Temp. compensation
X gain[1]	1.27	0.92	1.001	-0.000 809 $°C^{-1}$
Y gain[1]	1.25	1.03	1.029	+0.000 235 $°C^{-1}$
Z gain[1]	1.07	1.02	1.079	-0.000 224 $°C^{-1}$
X bias[2]	-15.09	15.25	-53.79	+0.588 $°C^{-1}$
Y bias[2]	-4.16	92.87	121.83	-0.485 $°C^{-1}$
Z bias[2]	-5.87	-99.12	215.44	+0.563 $°C^{-1}$
XY angle	90.29°	93.98°	97.25°	-
YZ angle	90.37°	82.95°	90.86°	-
XZ angle	89.56°	90.53°	90.96°	-
σ	0.13 µT	1.24 µT	0.8 µT	-

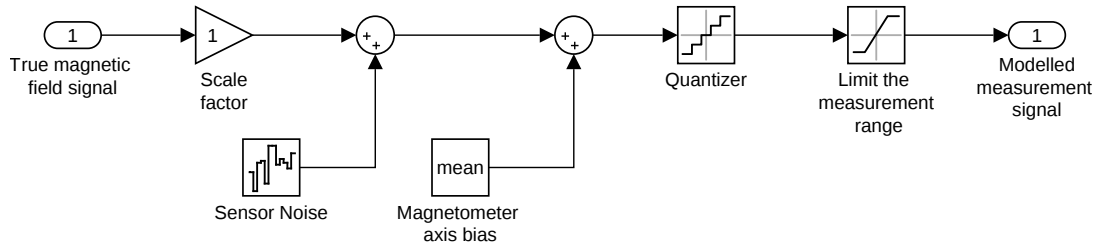

Figure 6.9: Simulink model of a single magnetometer axis. The reference signal of the magnetic field vector axis is scaled, then a noise and offset are applied. Effects of quantization and limited measurement range are also taken into account.

value can be estimated by performing an experiment with the stationary gyroscope[1] and calculating the Allan variance at $\tau = 1\,\mathrm{s}$ (see [102]). Example result of such an experiment for L3G4200D sensor is shown in Fig. 6.10. In case of this particular sensor the nominal rate noise density is declared by the manufacturer as $0.03\,^\circ\,\mathrm{s}^{-1}\,\sqrt{\mathrm{Hz}}^{-1}$ for a 50 Hz filter cut-off, and experimentally estimated to be $0.0187\,^\circ\,\mathrm{s}^{-1}\,\sqrt{\mathrm{Hz}}^{-1}$, $0.0191\,^\circ\,\mathrm{s}^{-1}\,\sqrt{\mathrm{Hz}}^{-1}$ and $0.0231\,^\circ\,\mathrm{s}^{-1}\,\sqrt{\mathrm{Hz}}^{-1}$ for X, Y and Z axes respectively in a presented case. Static experiment is also helpful for determining the gyroscope bias, simply by calculating mean value of the angular rate measured over a long period of time. In this case the bias for each axis has been identified as $0.36\,^\circ\,\mathrm{s}^{-1}$, $-1.36\,^\circ\,\mathrm{s}^{-1}$ and $0.06\,^\circ\,\mathrm{s}^{-1}$. Additionally, an internal hardware low-pas filter is available in case of most MEMS rate gyroscopes. In this case to match the Fourier spectrum of the noise a third order Chebyshev filter was used. It can be modelled with transfer function[2]

$$G_{lp}(s) = \frac{4.53}{s^3 + 114.5s^2 + 119s^{+}4.53}. \tag{6.6}$$

[1]Interestingly, the gyroscope mounted to the ground is in fact slowly revolving together with the Earth spinning motion. Angular rate of this motion is on the order of $4 \times 10^{-3}\,^\circ\,\mathrm{s}^{-1}$, and therefore much smaller than the resolution of the sensor used in this example. However, this movement would have to be taken into account in case of more precise sensors.

[2]Parameters of the filter where found by manipulating the cut-off frequency and ripple ratio until the simulated noise had visually similar characteristic in the frequency domain.

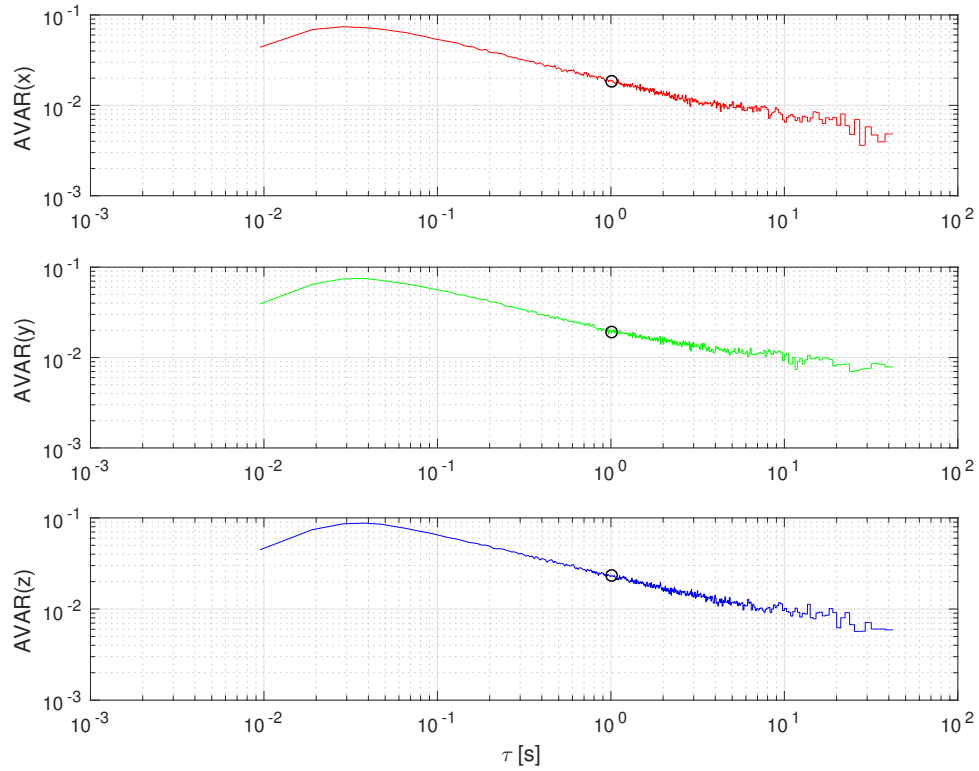

Figure 6.10: Allan variance of the measured gyroscope data in a static experiment

Note, that in reality the filter implemented in the gyroscope chip is discrete (z domain). However, for the relatively low sampling frequencies used in satellite attitude estimation the difference between analogue and digital model is not significant and it is more convenient to use the 's' domain filter in Simulink model. At the end it is necessary to take into account the quantization and saturation effects. Quantization is caused by the finite number of bits representing the data and described by a resolution parameter in sensor documentation. In case of the L3G4200D it is equal to $8.75\,\mathrm{m}^\circ\,\mathrm{s}^{-1}$ when the saturation limits are set to $\pm 250\,^\circ\,\mathrm{s}^{-1}$. Comparison of the angular rate measured with the stationary sensor and simulated with all the mentioned effects is shown in Fig. 6.11. Although time domains allows for visual comparison of the noise variance and bias, the frequency domain is more convenient to observe the effects of the internal dynamics. Such a comparison is given in Fig. 6.12. Note that plots show a decrease in noise at the low-pass filter cut off, but the decrease stops at around 13 Hz due to the quantization noise. The Simulink model of a gyroscope axis shown in Fig. 6.13 was used to generate both the Fig. 6.11 and Fig. 6.12 simulated characteristic. Similarly to the magnetic field sensor the rate gyroscope measurement is also affected by axis misalignment, scale errors and temperature drift. Accounting for those effects requires a precise calibration stand with fixture allowing for precise rotation of the sensor. The gyroscope bias ${}^b\boldsymbol{\omega_B}$ is also susceptible to temperature[3], which is an important factor in case of the picosatellites. In this thesis the proposed attitude estimator deals with this problem by dynamically estimating the bias (see section (5.13)).

[3]There is also a strong dependency on acceleration as described in [80], but in the microgravity conditions placing the gyroscope near the mass centre of the satellite allows to gracefully avoid this problem.

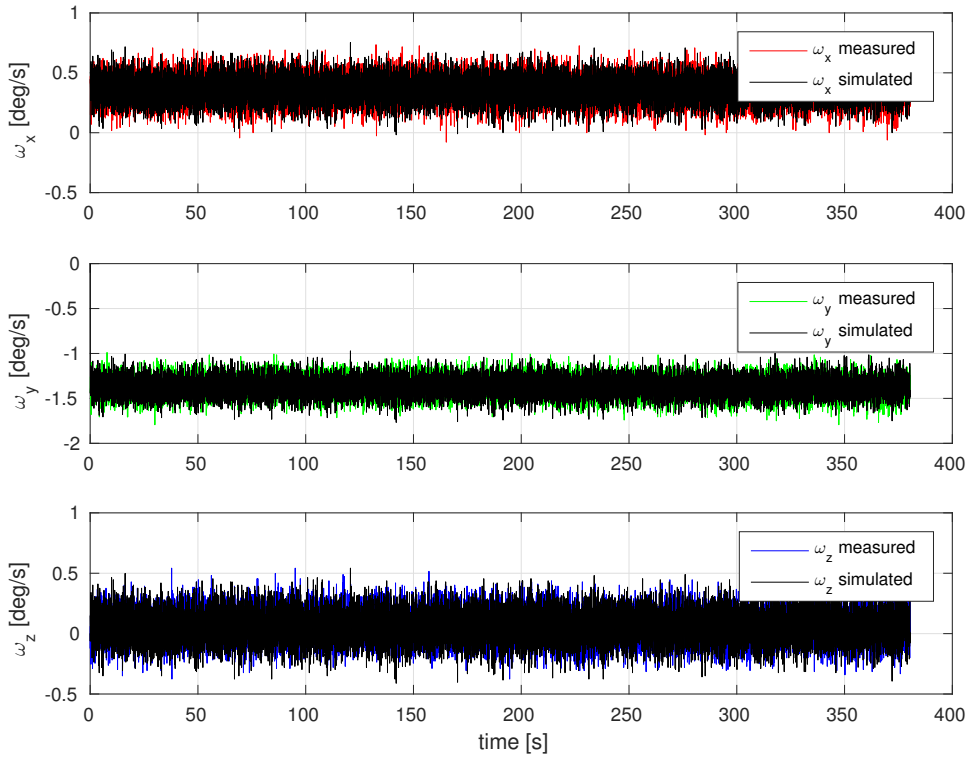

Figure 6.11: Measured and simulated gyroscope data in a static experiment

6.3.3 Sun sensor calibration

Several types of sun sensor exist. For nanosatellites two types are dominant. First of them are the coarse sun sensors, relying on a light intensity measurement performed in several locations on the satellite surface[4]. Those measurements can then be fused to estimate the Sun vector measurements. A set of pinhole sensors with CMOS arrays are the second, more precise solution. Calibrating such a Sun sensor setup is a complex task, due to a several reasons. First of all a few sensors are needed to provide the full field of view. Those must be placed precisely, an their orientation in the satellite body frame needs to be carefully measured. Secondly all they contain a simple optical pinhole setup, which is subjected to mechanical imperfections that need to be identified. Finally, CMOS array is a complex sensor in itself, and the measurements of the light intensity illuminating all pixels need to be fused to generate the Sun vector angle estimate. An example of the equipment and procedures used to perform such a calibration is described in [23]. Below some outline is given on the parameters that need to be identified.

The Sun sensor consists of a CMOS array covered by an elevated opaque thin film with a pinhole. Rays shining on the film are absorbed, and only some portion of light is passed to the sensing device as shown in 6.14a. The location of the place at which the CMOS array is illuminated depends on the angle of the sun rays with relationship to the sensor surface. Unfortunately, the distance between the pinhole and the sensing array is difficult to arbitrarily manufacture with sufficient precision. Therefore, it needs to be calibrated by shining a light at precisely controlled angle at the fully assembled sensor. Also, the pinhole

[4]It has been attempted to use the solar arrays themselves to perform those measurements to avoid using dedicated sensors.

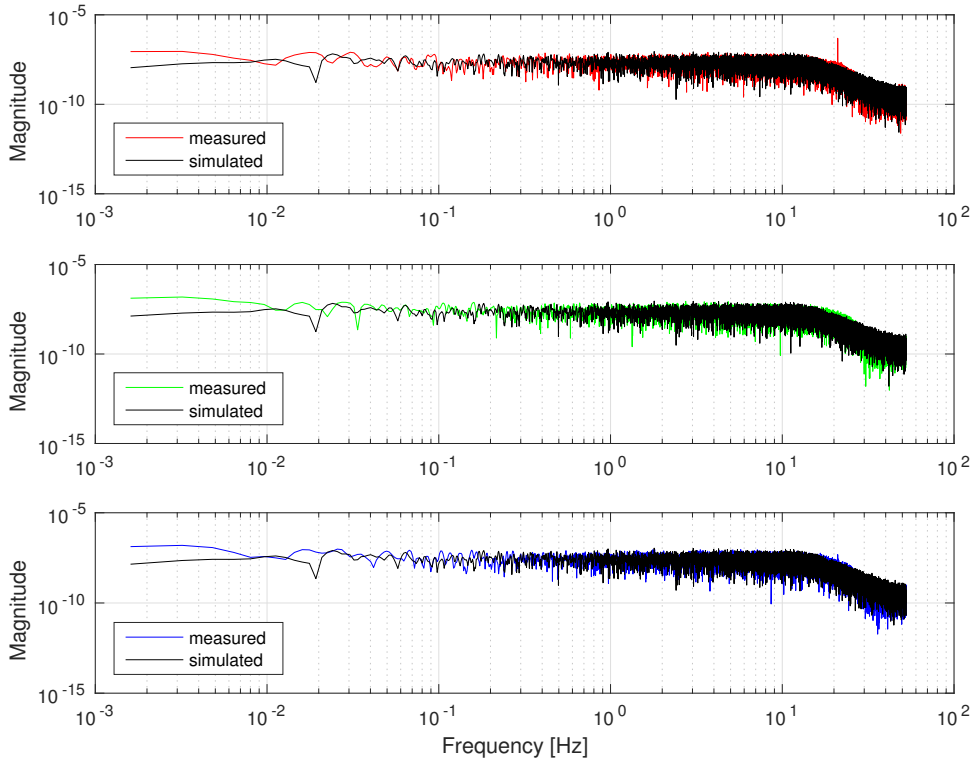

Figure 6.12: Fast Fourier Transform (FFT) of the measured and simulated gyroscope data in a static experiment

width may vary, and it needs to be precisely measured in order to determine the size of the Sun spot illuminating the array. This parameter is required by the sensor internal algorithm. Some Sun sensors work in one axis, but as square CMOS arrays are available it makes sense to measure the sun spot position in two dimensions consecutively as seen in 6.14b. Then the pinhole location with relation to the array needs to be determined, as it is difficult to place it precisely in the centre of the sensor. The pinhole size is selected in such a way that the Sun spot shining on the CMOS array illuminates several pixels. Then, by approximating the Sun spot intensity distribution with a mathematical model[5] one can estimate its centre with a resolution much grater than a single sensor pixel. For

[5]Note that the diffraction and interference occurs if the pinhole is small enough.

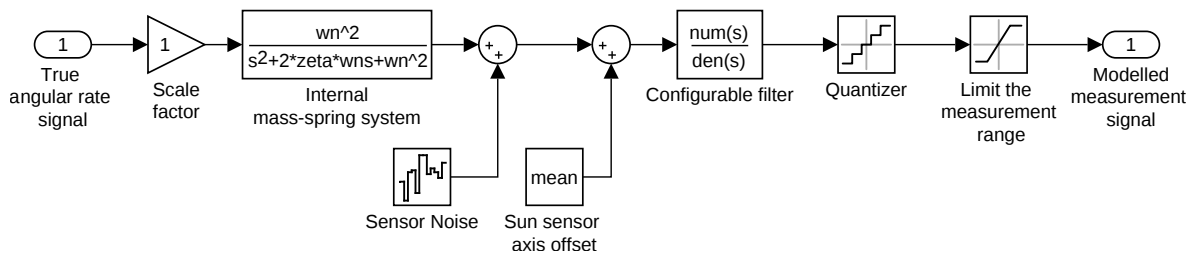

Figure 6.13: Simulink model of a single MEMS gyroscope axis. The reference signal is fed to the model of the miniature mass – spring system, then a noise and bias is added. A configurable digital low pass filter present in most such devices is also modelled, together with the quantization effect and limitation of the measurement range.

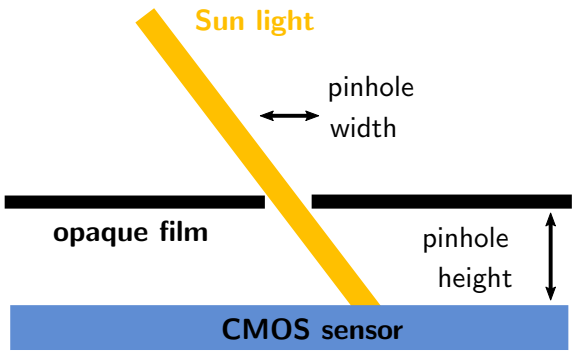

(a) Sun sensor pinhole (side view)

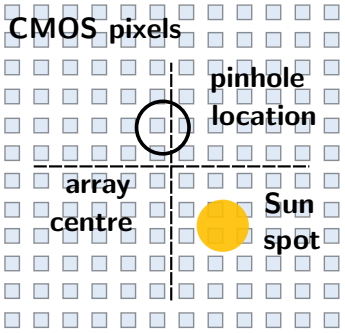

(b) Sun sensor CMOS array (top view)

Figure 6.14: Basic operation principle of a pinhole Sun sensor. Sunlight shines on a CMOS array through a pinhole. Direction of the Sun can be estimated from the location of the spot by a simple trigonometry.

the sake of simplicity this complicated behaviour is not modelled in this thesis, and a simplified model, similar to this decribing the magnetometer behaviour is used as shown in Fig. 6.15.

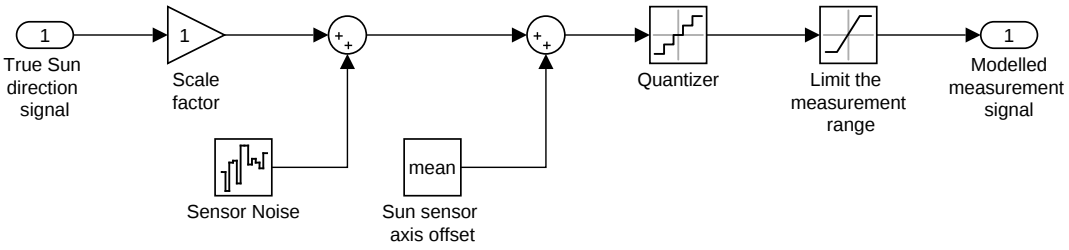

Figure 6.15: Simulink model of a single Sun sensor axis. The reference signal of the Sun direction vector axis is scaled, then a noise and offset are applied. Effects of quantization and limited measurement range are also taken into account.

6.4 Evaluation of the attitude observer quality

6.4.1 Lithuanica SAT-2 example

Let us consider a case study that can be conducted in order to investigate the SDQAE algorithm performance in a challenging real scenario. Lithuanica SAT-2 mission scheduled to launch in 2017 as a part of the QB50 initiative [26] is an interesting example of a scientific nanosatellite programme. The satellite consists of a spacecraft bus and an atmospheric sensor package designed to investigate the upper layers of the Earth atmosphere. Due to the character of the measurement the instrument needs to be oriented towards the direction of the satellite motion. An attitude stabilization scheme is used

where deployable solar panels move the centre of atmospheric pressure behind the satellite centre of mass creating stable attitude configuration. Additionally, magnetic torquers are used to actively dump the oscillations and introduce slow rotation of the spacecraft along the velocity axis to further stabilize the attitude. Interestingly, complete attitude knowledge is not required for this system to work, and scientific package only requires the measurement of the angle of attack of the sensor. Regardless, an attitude determination system still needs to estimate the attitude quaternion. For orientation knowledge a MEMS gyroscope, Anizotropic MagnetoResitive (AMR) magnetometer and four Sun sensors are used. Field of view of each of the solar sensors is limited to a cone section and each of them is placed on a panel that is parallel to the direction of satellite motion as shown in Fig. 6.16. As predicted orbit for Lithuanica SAT-2 is highly inclined LEO the

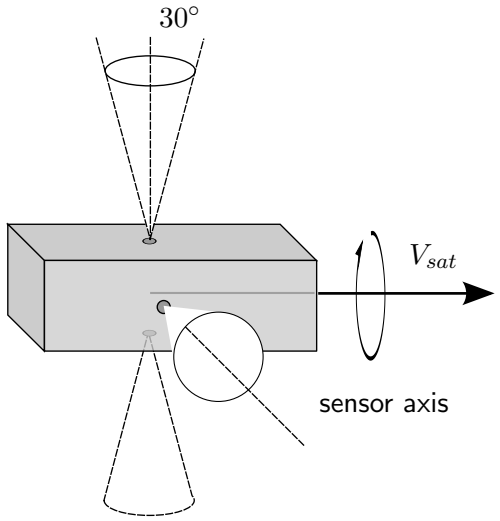

Figure 6.16: Lithuanica SAT-2 configuration. The satellite is aerodynamically oriented to face the direction of motion with the sensor panel and put in a slow spin around the axis for stabilization. Sun sensors are located on four panels with their optical axes perpendicular to the spin axis.

worst case scenario for the Sun vactor availability has to be considered. There are two limitations which prevent Sun sensors from performing the measurement. First is when the Sun is eclipsed by the Earth. Secondly, even if the Sun illuminates the satellite it also needs to be in the field of view of one of the sensors. Attitude estimator depicted in Fig. 5.2 was employed, as the set of sensors matches the Lithuanica SAT-2 configuration.

The simulation experiment was performed in three phases:

1. Generation of orbital data.
2. Tuning of the algorithm.
3. Monte Carlo study.

The orbital data has been generated with the environment described in Sec. 6.1. Three orbital trajectories were used as seen in Tab. 6.2. One of them was used for tuning the

Table 6.2: Details of the orbits, initial orientation and rate of rotation used in the experiment. One set is used for estimator tuning, other in optimistic scenario simulations, and the last one is the pessimistic case with the worst conditions for Sun sensors operation.

Symbol	Unit	Name	Tuning	Pessimistic	Optimistic
e	[-]	orbit eccentricity	0	0	0
i	[°]	orbital inclination	98	98.18	98.18
a	[km]	semi-major axis	6768	6771	6771
Ω	[°]	longitude of ascending node	177.8	177.8	87.8
T_{max}	[s]	Duration of the simulation	13000	13000	13000
ω_s	[$^\circ\,\mathrm{s}^{-1}$]	satellite rotation rate	10	3	3
–	[°]	initial estimation error	1	180	180

algorithm, one represents the worst case scenario with longest possible eclipses, and the last on represents the optimistic scenario, were satellite is constantly in sunlight. All of those trajectories last for 13 000 s of simulated time which represents more than two revolutions of the satellite around the Earth. All of those data sets represent a circular orbit with parameters close to those projected for Lithuanica SAT-2 satellite. Slight differences in inclination and semi-major axis where introduced between the tuning and the verification datasets to account for imprecise orbit insertion manoeuvre. Difference in the longitude of the ascending node causes the difference in the eclipsing conditions. Satellite spin around its linear velocity vector of $10\,^\circ\,\mathrm{s}^{-1}$ was assumed for the tuning and $3\,^\circ\,\mathrm{s}^{-1}$ for verification orbits. Tuning assumed the initial orientation estimate within 1° of the actual one, but the Monte Carlo experiments accounted for the worst possible initial estimate error of 180°. Sensors were modelled as described in Sec. 6.2. Values of the measurement range, resolution, bias and noise were set as described in Tab. 6.3.

Table 6.3: Sensor models parameters assumed in the simulations

Sensor	Measurement range	Resolution	Noise mean	Noise variance
rate gyroscope[1]	$250\,^\circ\,\mathrm{s}^{-1}$	$1/131\,^\circ\,\mathrm{s}^{-1}$	variable	$0.0025(^\circ s^{-1})^2$
magnetometer[1]	88 µT	73 nT	0 nT[3]	0.4 nT[2]
Sun sensor[2]	1	0.0001	0.000 016 04	0.000 846

Algorithm tuning is necessary to find the suitable values of the weights c_m and c_s. Estimator gains K and K_ω also need to be determined in this manner. As the sum of weights is constrained to be equal to one, this gives total number of three independent optimization parameters. Tuning was performed as described in Sec. 5.3.4. SDQAE estimator was run for the tuning orbit data set and the value of objective function was calculated. The objective function represented root mean square error $\delta\theta_{RMS}$ (see Sec. 5.3.1) over 50 runs of the algorithm. Each run was 13000 samples long and employed a distinct randomized set of sensor noise values. As mentioned before initial orientation error was fixed, and equal to 1°, but the initial orientation was also randomized for each of the 50 experiments

[1]Performance declared by the manufacturer.

[2]Projected performance. Sensor returns normalized direction vector, so each axis returns the maximum of 1 unit. Norm of the vector is slightly affected by the quantization error.

[3]Assuming perfect bias calibration.

with that constraint in mind. The generalized optimization process depicted in Fig. 5.4 applied for the case of Sun and magnetic field sensor is shown in Fig. 6.17. As a result of

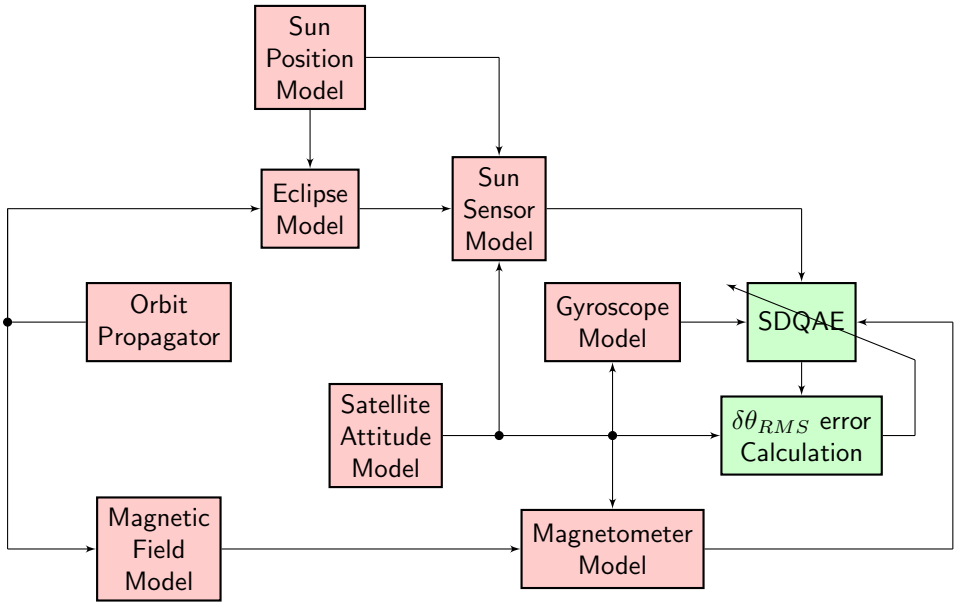

Figure 6.17: The SDQAE observer tuning setup for Magnetic and Sun sensor case

this procedure a following set of parameters was determined:

$$\begin{bmatrix} K \\ K_\omega \\ c_m \\ c_s \end{bmatrix} = \begin{bmatrix} 8.7 \times 10^{-2} \\ 9.3 \times 10^{-6} \\ 4.1 \times 10^{-1} \\ 5.1 \times 10^{-1} \end{bmatrix} \tag{6.7}$$

Monte Carlo verification experiments consisted of 200 iterations. For each of them a different set of sensor random noise values were generated (see Sec. 6.2). Also, the initial orientation estimate was randomly generated each time, with additional constrain to start from maximal orientation error of 180°. All the resulting attitude estimation error were gathered and their mean value $\delta\theta_{MC}$ (see Sec. 5.3.1) and standard deviation were calculated for each of the time steps. Fig. 6.18 presents the result of the verification performed for the pessimistic orbit. The black and white bar at the top indicates if the Sun sensor provided the Sun direction data at the time. This happens when satellite is not eclipsed by the Earth and the Sun is in field of view of one of the four sensors. Due to the satellite spin and shape of the highly inclined orbit the group of closely separated Sun visibility periods occurs once every orbit. Solid line on the plot represents the mean error value, and is enclosed with two dashed lines at $\pm\sigma$ distance representing the noise standard deviation. Providing all sensor readings are available, it is apparent that the SDQAE converges within 100 second of the simulated time.

As Lithuanica SAT-2 mission requires precise estimation of the angle of attack of the atmospheric sensor suite rather than the full attitude estimation it is necessary to calculate the angle of attack indication as well. Mean of this angle $\delta\eta_{MC}$ is presented in Fig. 6.19 in a similar fashion to the previous plots. Obviously, this value is always smaller or equal to the total angular error. It is apparent that relatively large attitude estimation

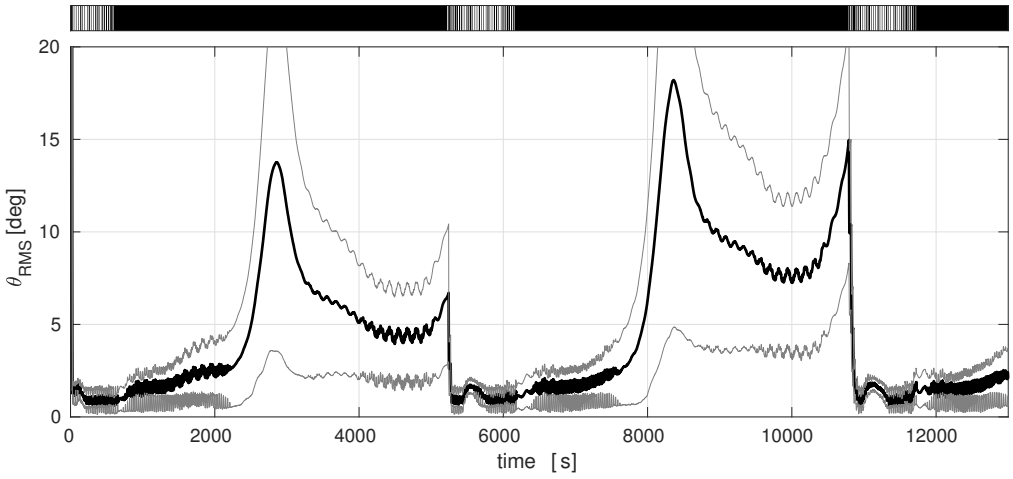

Figure 6.18: Mean angular error of the attitude estimation $\delta\theta_{MC}$ enclosed in $\pm\sigma$ envelope for pessimistic orbit (200 Monte Carlo iterations). Horizontal axis represents the simulation time. In the presented case evaluation of the algorithm occurs once every simulated second.

errors occur starting roughly from the middle of the eclipse periods, around 3000 and 8500 second of the simulation respectively. To understand the reason of this phenomenon it is necessary to realize that during that time satellite is crossing equatorial plane while travelling in nearly perpendicular direction to this surface. Due to the fact that magnetic field of the Earth is also aligned in a similar direction it becomes nearly parallel (or anti-parallel) to the satellite velocity vector (see Fig. 6.20). As the Sun direction information is unavailable at the time the rotation around the velocity axis of the satellite, which is the main rotation axis, becomes nearly unobservable. The only way the satellite is tracking it is the integrated gyroscope measurement, which due to its nature accumulates angular errors with time. Fig. 6.21, Fig. 6.22 and Fig. 6.23 show the gyroscope bias estimation depicted with black solid lines compared with red green and blue lines representing the true bias. As bias is by definition constant in time it is necessary to explain that in practice MEMS gyroscope bias is strongly dependent on temperature. Small satellite travelling around the Earth experiences significant temperature variations due to the eclipses[6]. Therefore, in this experiment bias is defined as the zero error of the sensor at the time of each measurement. To simulate this effect a sinusoidal bias characteristic with frequency approximating orbital revolutions frequency and amplitude of 0.1° was assumed. Results indicate that this 'variable bias' signal was successfully tracked during the whole simulations, even when the Sun sensor informations were unavailable.

Estimation of the total angular error for similar orbit, but oriented in such a way that satellite is never eclipsed by the Earth yields much better results as seen in Fig. 6.24. This estimation experiments was performed with the same weights and proved to be much easier task as the mean error never exceeds 1° with small standard deviation values. Such result translates in even better estimate of the angle of attack shown in Fig. 6.25

[6]Due to the lack of atmosphere radiation is the only method of temperature transfer between the spacecraft and its environment. For small satellites the temperature cycle during a single orbit on the surface of solar panels can be on the order of many tens of degrees Celcius.

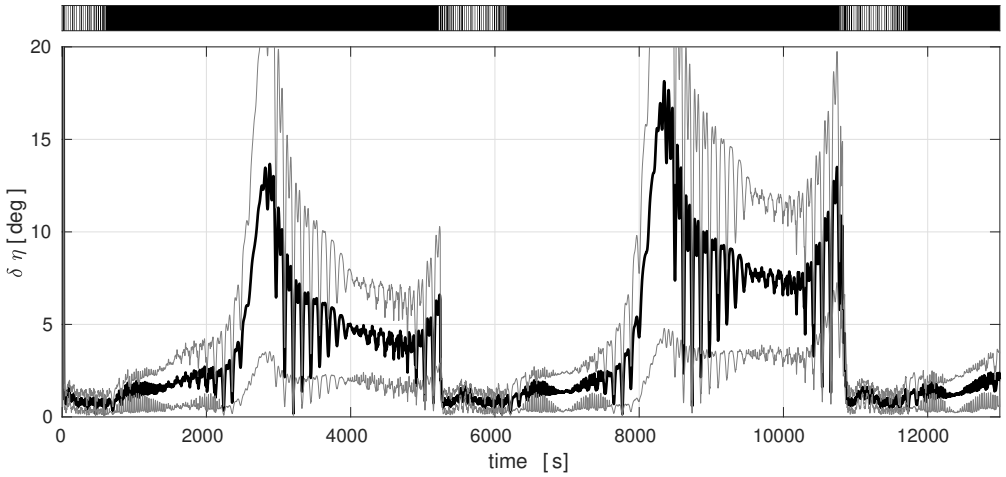

Figure 6.19: Mean angle of attack estimation error $\delta\eta_{MC}$ enclosed in $\pm\sigma$ envelope for pessimistic orbit (200 Monte Carlo iterations). Horizontal axis represents the simulation time. In the presented case evaluation of the algorithm occurs once every simulated second.

6.4.2 Comparison of attitude observers

In order to compare the performance of SDQAE observer to other solutions, selected algorithms described in Tab. 3.2 have been implemented in MATLAB environment. A Monte-Carlo study was undertaken with parameters similar to those described in section Sec. 5.2. The notable difference is that, this time, a full field of view of the Sun sensors was assumed. This assumption was changed in order to verify if full knowledge of the Sun vector (except the eclipses) would improve the system performance to an acceptable level. Also, the initial estimate error was set to 0°[7].

The following attitude observers were selected: SDQAE, TRIAD, FOAM, QUEST and Q-method. Additionally, a simple EKF, with the following state vector has been implemented:

$$\boldsymbol{x} = \begin{bmatrix} {}^{b}_{i}\hat{q} \\ {}^{b}\hat{\boldsymbol{\omega}}_{\boldsymbol{B}} \end{bmatrix}, \tag{6.8}$$

where ${}^{b}\hat{\boldsymbol{\omega}}_{\boldsymbol{B}}$ is a 3×1 vector representing the bias estimate. The filter is more thoroughly described in the appendix Ch. B. An assumption was made that the attitude dynamics model is unavailable. This is due to the fact that attitude forces are difficult to estimate for a small satellite with high surface area to mass ratio. Adequate modelling of those phenomena is beyond the scope of this thesis (short outline is given in Sec. 6.2). It is worth noting that due to the normalization of the magnetic field measurement (see Sec. 6.2) the magnetic sensor error does not conform to the assumption of the EKF inputs being burdened with white Gaussian noise. This can be verified by performing a simulated

[7]Note that the convergence of the SDQAE algorithm from the maximum initial estimate error of 180° has already been shown in Sec. 6.4.1. This time a 0° initial error is selected for two reasons. First, some of the other observers estimate attitude in a single frame, without the effect of initial convergence. This would make a quantitive comparison harder (by favourising them). Aditionally, EKF sometimes has troubles to converge at all, which also randomly distorts the results.

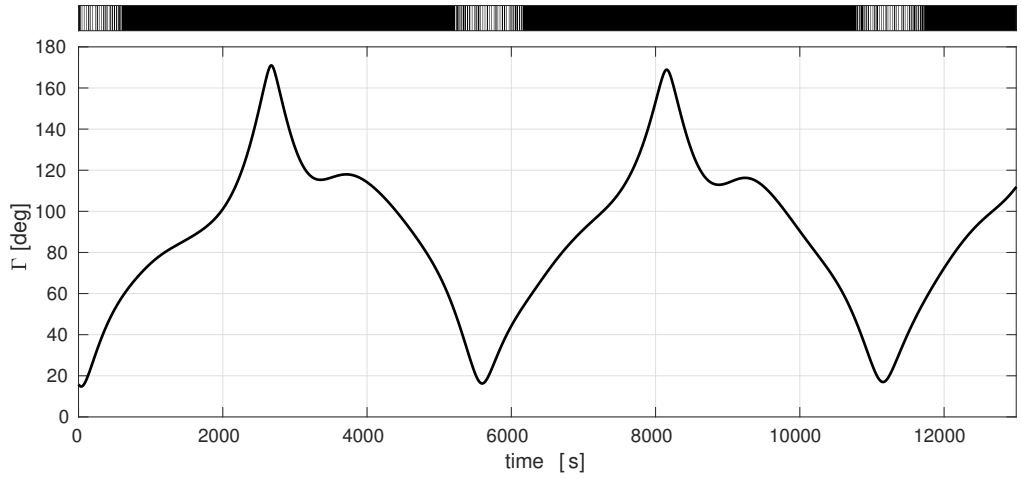

Figure 6.20: Angle Γ between the magnetic field and the rotation axis for pessimistic orbit. Horizontal axis represents the simulation time.

measurement with magnetometer model implemented as shown in Fig. 6.9. This scenario yields error distributions as seen in Fig. 6.26. It is clear that the error distribution presented as bar plots does not correspond to the best Gaussian fit represented with red lines.

A Monte-Carlo study consisting of 200 runs for the pessimistic orbit scenario (see Tab. 6.2) was performed. Mean angular error estimates for all the tested attitude estimators are shown in Fig. 6.27. Note that the black bar above the plot indicates the time at which the Sun sensor measurement is not available. Due to the full field of view of the sensors analysed in this study the measurement is available for the entire period when the satellite is not in the eclipse. This is in contrast to the situation presented in Fig. 6.18. When the Sun sensor measurement is available all of the estimators are able to track the attitude with various errors. The EKF yield a mean error around 3° with standard deviation generally within 1.5°. The Q-method, QUEST, and FOAM produce very similar results with the mean errors around 2° and notably higher standard deviation. The simplest TRIAD algorithm produces errors that are around 0.5° worse with similar standard deviation. Clearly, the best performance is delivered by the SDQAE estimator with the mean angular error $\delta\theta_{MC}$ being under 1° and standard deviation below 0.5°. Due to the fact that only the SDQAE and EKF estimators are capable of processing the angular rate measurement all of the other observers do not provide any attitude information when the Sun vector measurement data is unavailable. Of the two, the EKF clearly does a worse job maintaining small attitude estimate error in the eclipse. The mean error reaches 95° with standard deviation. It is worth noting that in the absence of the Sun Vector data EKF was just fed with zero vector. In reality a separate observers could be designed for eclipse case. Proposed SDQAE observer maintains the mean error within 11° with standard deviation below 7°. To uncover the reason of that performance gap one has to turn to the analysis of the angular rate bias estimation in each of the axes shown in Fig. 6.29, Fig. 6.30 and Fig. 6.31 respectively. Despite the efforts of the author the EKF could not be tuned to track the bias correctly. Except the fact that EKF is not optimal in the sense that Kalman Filter is and the fact of non-Gaussian sensor noise there is another possible reason for that behaviour. It is worth noting that the EKF is effectively fed with zero

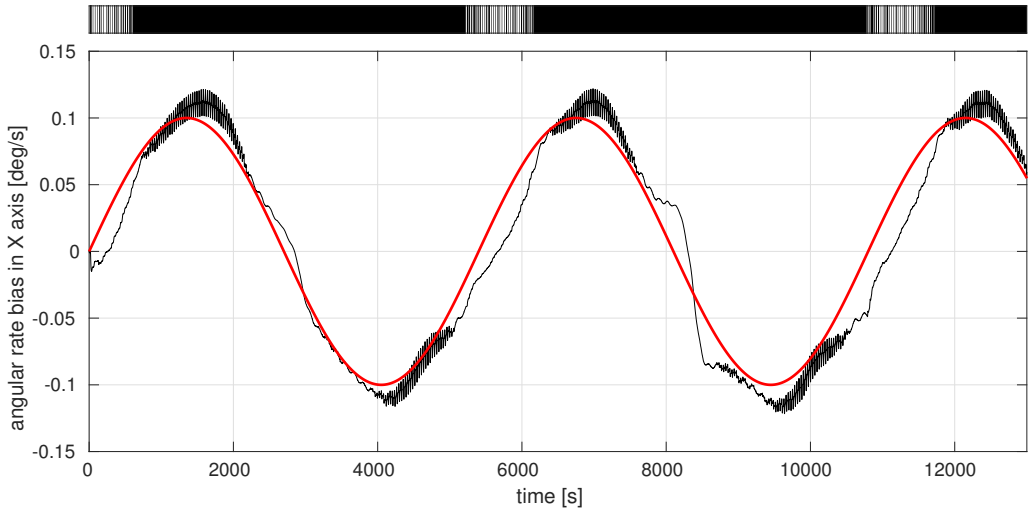

Figure 6.21: Mean X axis bias estimation value (true value in red for comparison). Horizontal axis represents the simulation time. In the presented case evaluation of the algorithm occurs once every simulated second.

measurement of the Sun vector during the eclipse. This of course disrupts the behaviour of the filter. As it turns out the SDQAE is much more robust to the fact that one of the measurements becomes unavailable. The quantified results of the performed tests are visible in Tab. 6.4. The $\delta\theta_{RMS}$ error for each of the tested estimator is given. For the SDQAE and EKF the performance is given both excluding and including the time spent in the eclipse. As other algorithms are unable to provide attitude estimate without the Sun vector measurement only the first value is provided for them.

Table 6.4: Comparison of the attitude determination performance. Only the SDQAE and EKF methods are able to function in the eclipse by utilizing the gyro signal.

Estimator	$\delta\theta_{RMS}$ (without eclipse)	$\delta\theta_{RMS}$ (with eclipse)
SDQAE	0.69°	3.96°
EKF	4.92°	48.54°
Q-method	2.39°	–
QUEST	5.32°	–
FOAM	2.42°	–
TRIAD	2.82°	–

Upgrade of the Sun sensor set-up[8] design in Lithuanica SAT-2 proves to be a plausible solution to the current attitude determination subsystem not meeting the required 1° angle of attack error while the satellite is illuminated by the Sun. However, in the eclipse the error exceeds this threshold around 10 times, which seems to suggest that it is very difficult to provide this kind of precision without resorting to more complex sensing equipment (such as a miniature star tracker).

[8]By extending the sensor field of view to give complete coverage.

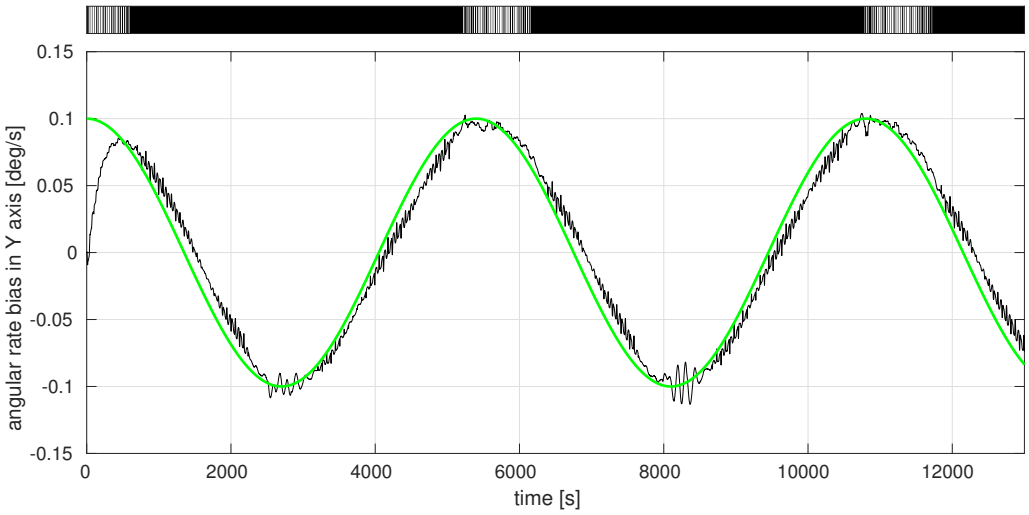

Figure 6.22: Mean Y axis bias estimation value (true value in green for comparison). Horizontal axis represents the simulation time. In the presented case evaluation of the algorithm occurs once every simulated second.

6.4.3 Multi-rate sensor sampling example

The SDQAE algorithm structure shown in Fig. 5.1 assumes that the attitude sensors are sampled with equal sampling period. It is, as it turns out, not a necessary condition for the estimator to work. Let us make a similar assumptions for in Mote-Carlo experiment described in section Sec. 6.4.2, but thus time use different sampling rates for each of the sensors, namely

$$\begin{aligned} T_g &= 1\,\mathrm{s}, \\ T_m &= 2\,\mathrm{s}, \\ T_s &= 3\,\mathrm{s}. \end{aligned} \tag{6.9}$$

Such sampling periods T_g, T_m, and T_s of the gyroscope, magnetometer, and Sun sensor create a situation where one, two or all of them are sampled each second. This is not a problem for the algorithm, with an exception of the bias estimation loop described in equation (5.13). If both the magnetometer and the Sun sensor are not sampled simultaneously the bias correction term $\frac{\nabla L({}^b_i\hat{q}_p)}{\left\|\nabla L({}^b_i\hat{q}_p)\right\|}$ cannot be calculated and needs to be substituted with zero quaternion. Additionally, the initial attitude estimate was chosen in such a way, that $\delta\theta_0 = 180°$. This was done to test, if the multirate sampling does not prevent the algorithm from converging.

The plot in Fig. 6.32 shows the mean angular error enclosed in $\pm\sigma$ standard deviation envelope. Surprisingly, the results are not significantly different from the SDQAE performance depicted in Fig. 6.27. If we measure the $\delta\theta_{RMS}$ by disregarding the first 1000 s to remove the effect of the higher initial error we can compare the results agianst the one presented in Tab. 6.4. In this case we achieve $\delta\theta_{RMS} = 1.03°$ for the period when Sun sensor data is available, and $\delta\theta_{RMS} = 4.72°$ when including the periods when the satelite is in the eclipse. This suggests that decreasing the sampling rate of some sensors can be

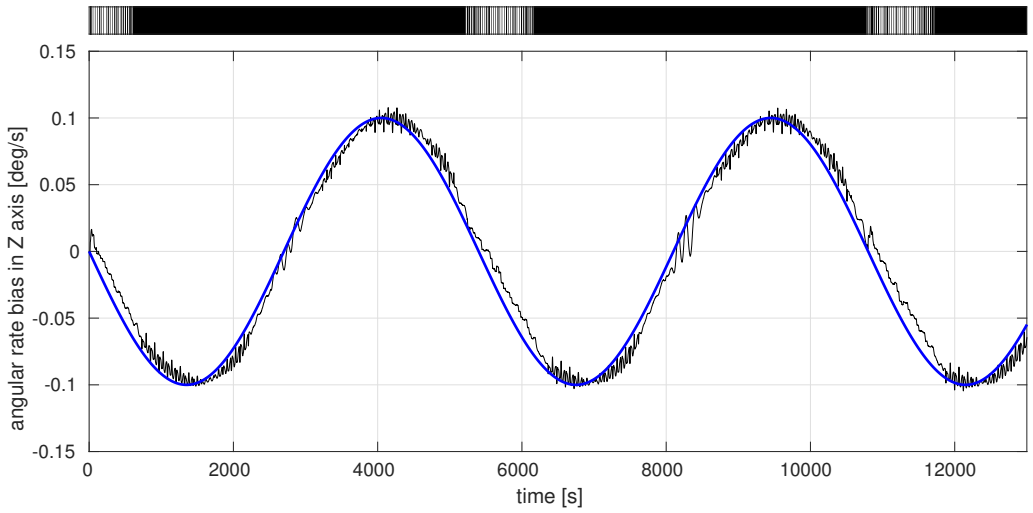

Figure 6.23: Mean Z axis bias estimation value (true value in blue for comparison). Horizontal axis represents the simulation time. In the presented case evaluation of the algorithm occurs once every simulated second.

considered a measure to save the energy[9]. A balance between the energy consumption and estimation precision can be tuned depending on the situation.

Fig. 6.33 shows the mean value of the angular rate sensor bias estimate, which is also similar to the result presented in Fig. 6.29.

Note that sensor tuning gives different values of K and K_ω depending on sensor rates. Therefore, the simulations in this sections were performed with the weights optimized for this case equal

$$\begin{bmatrix} K \\ K_\omega \\ c_m \\ c_s \end{bmatrix} = \begin{bmatrix} 3.6 \times 10^{-2} \\ 1.2 \times 10^{-5} \\ 6.2 \times 10^{-1} \\ 3.8 \times 10^{-1} \end{bmatrix}. \tag{6.10}$$

[9]Note for example the Sun sensor description in section Sec. 6.3.3. It is in fact a set of sensors, commonly based on a CMOS sensors and requiring signifficant computational effort to produce the Sun vector estimate.

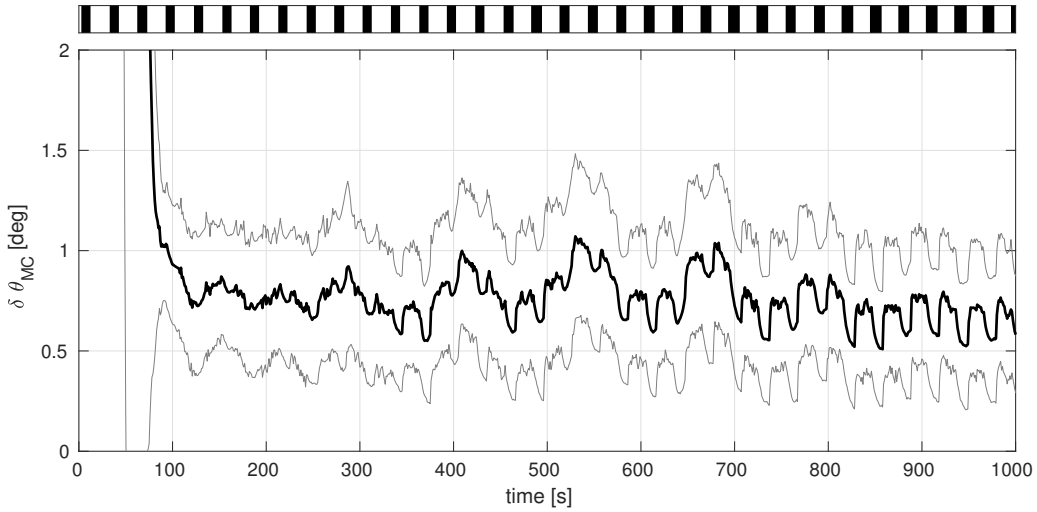

Figure 6.24: Mean angular error of the attitude estimation $\delta\theta_{MC}$ enclosed in $\pm\sigma$ envelope for optimistic orbit (200 Monte Carlo iterations). Horizontal axis represents the simulation time. In the presented case evaluation of the algorithm occurs once every simulated second. Note, that the plot contains only the first 1000 s of the simulation to better show the initial convergence and variations due to the periodical losses of the Sun direction measurement.

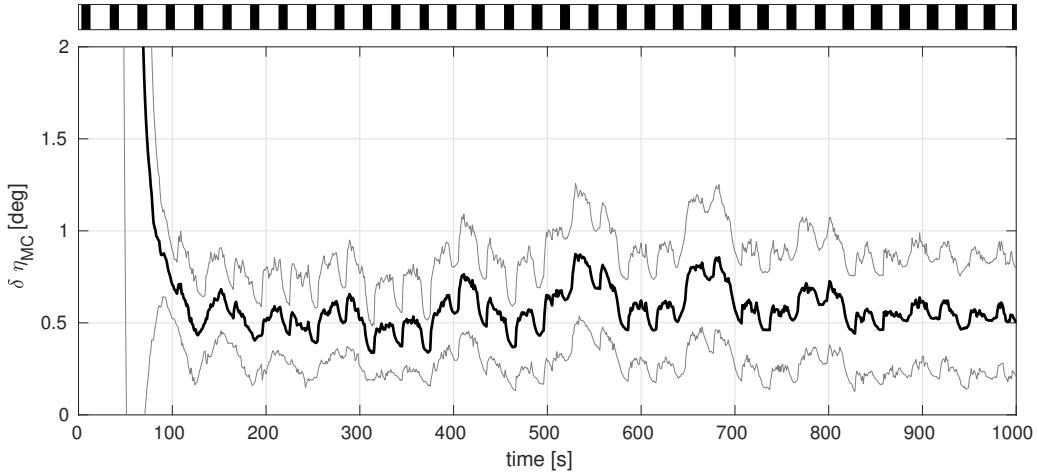

Figure 6.25: Mean angle of attack estimation error $\delta\eta_{MC}$ enclosed in $\pm\sigma$ envelope for optimistic orbit (200 Monte Carlo iterations). Horizontal axis represents the simulation time. In the presented case evaluation of the algorithm occurs once every simulated second. Note, that the plot contains only the first 1000 s of the simulation to better show the initial convergence and variations due to the periodical losses of the Sun direction measurement.

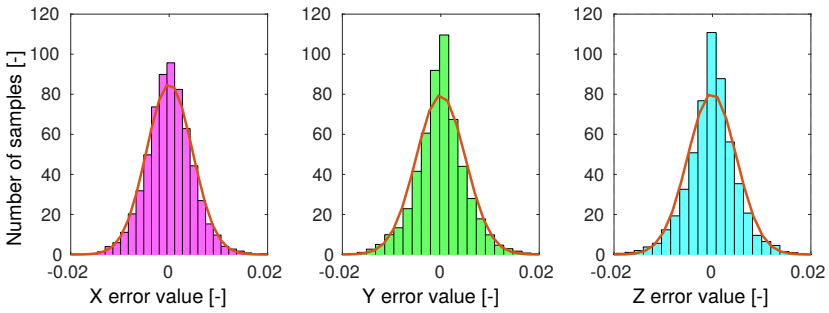

Figure 6.26: Error distribution of simulated normalized magnetic field sensor measurement error. Bars indicate the error histogram as determined with simulation, and the line represents the least square gaussian fit. Note, that the triaxial measurement is always normalized, which vsibly distorts the distribution empesising the smaller error values.

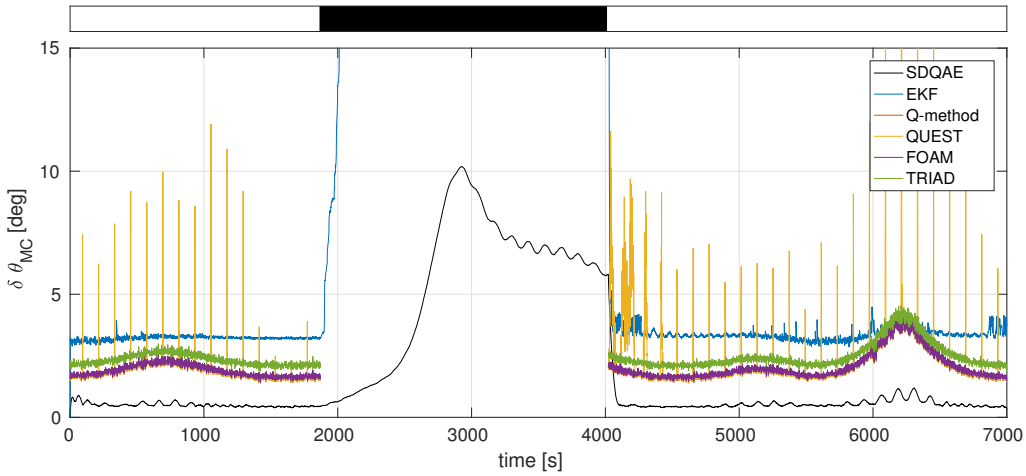

Figure 6.27: Comparison of the mean of the angular error $\delta\theta_{MC}$ estimate for selected attitude estimators. Horizontal axis represents the simulation time. In the presented case evaluation of all of the the algorithms occurs once every simulated second.

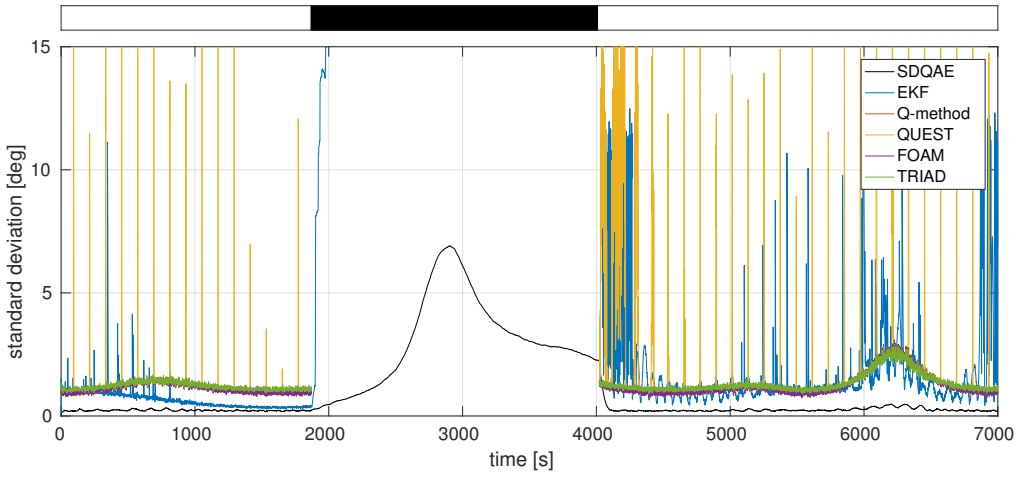

Figure 6.28: Comparison of the angular error estimate standard deviation for selected attitude estimators. Horizontal axis represents the simulation time. In the presented case evaluation of all of the the algorithms occurs once every simulated second.

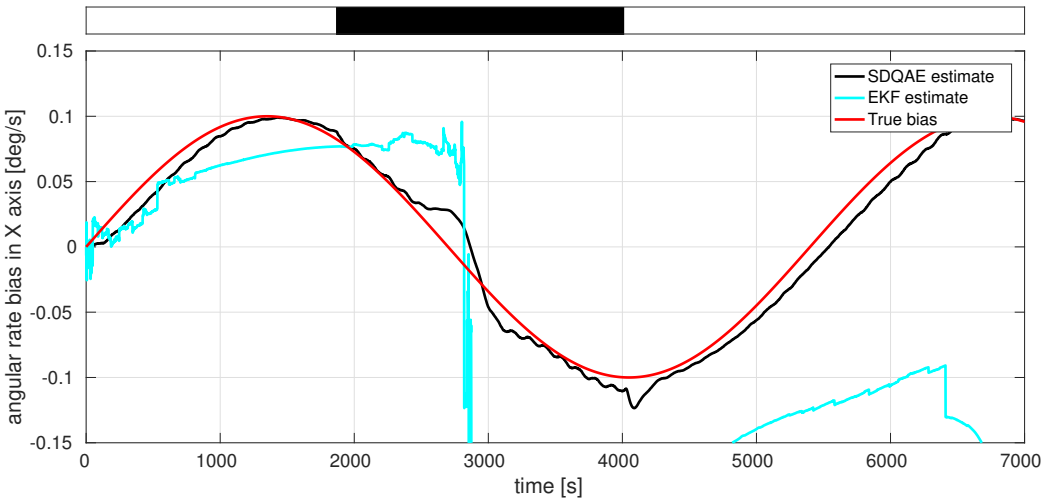

Figure 6.29: Comparison of the X coordinate of the mean angular rate sensor bias estimate. Horizontal axis represents the simulation time. In the presented case evaluation of both algorithms occurs once every simulated second. It is apparent that the SDQAE estimator succesfully tracks the bias even in the eclipse, while EKF does that to some extend only while the satellite is illuminated.

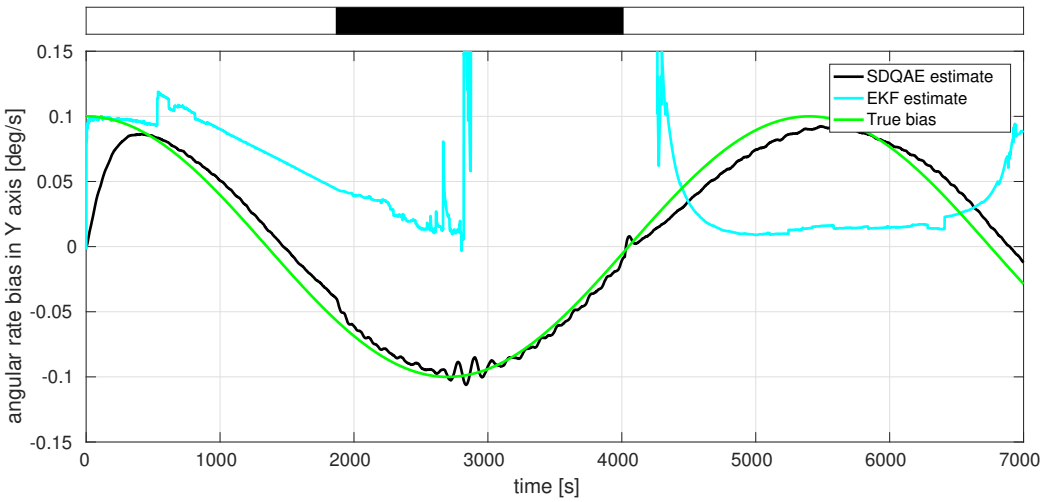

Figure 6.30: Comparison of the Y coordinate of the mean angular rate sensor bias estimate. Horizontal axis represents the simulation time. In the presented case evaluation of both algorithms occurs once every simulated second. It is apparent that the SDQAE estimator succesfully tracks the bias even in the eclipse, while EKF does that to some extend only while the satellite is illuminated.

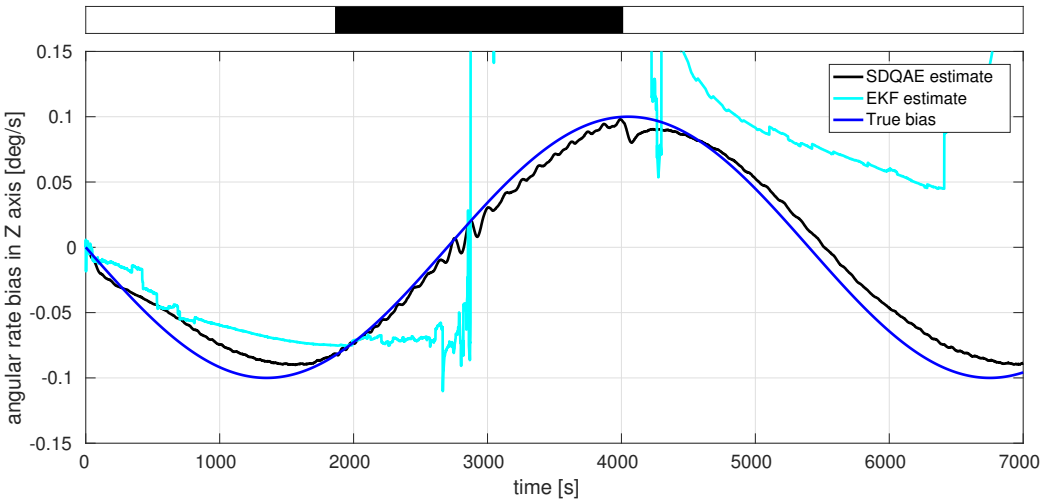

Figure 6.31: Comparison of the Z coordinate of the mean angular rate sensor bias estimate. Horizontal axis represents the simulation time. In the presented case evaluation of both algorithms occurs once every simulated second. It is apparent that the SDQAE estimator succesfully tracks the bias even in the eclipse, while EKF does that to some extend only while the satellite is illuminated.

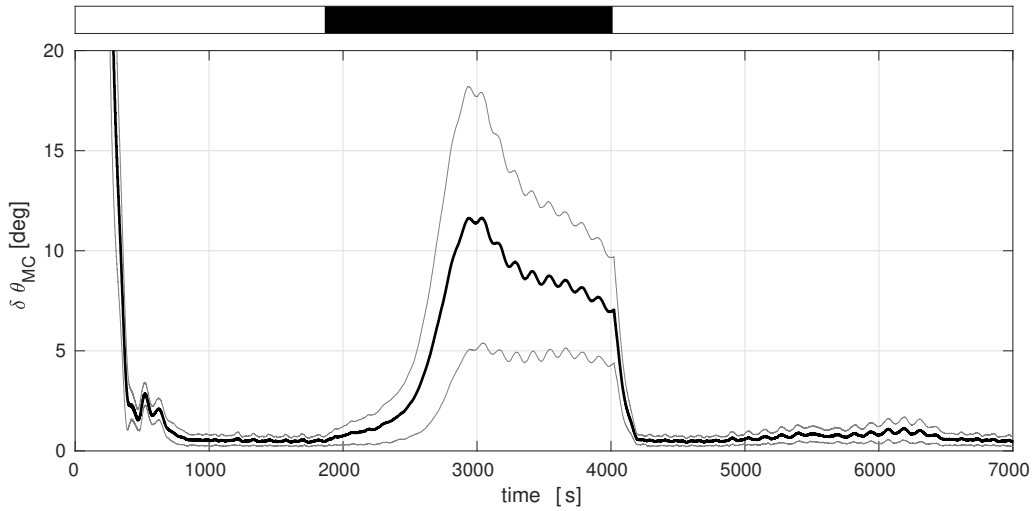

Figure 6.32: Mean of the angular error $\delta\theta_{MC}$ of the attitude estimation enclosed in $\pm\sigma$ envelope for pessimistic orbit and multi-rate sensor sampling case (200 Monte Carlo iterations). Horizontal axis represents the simulation time. In the presented case evaluation of the algorithm occurs once every simulated second.

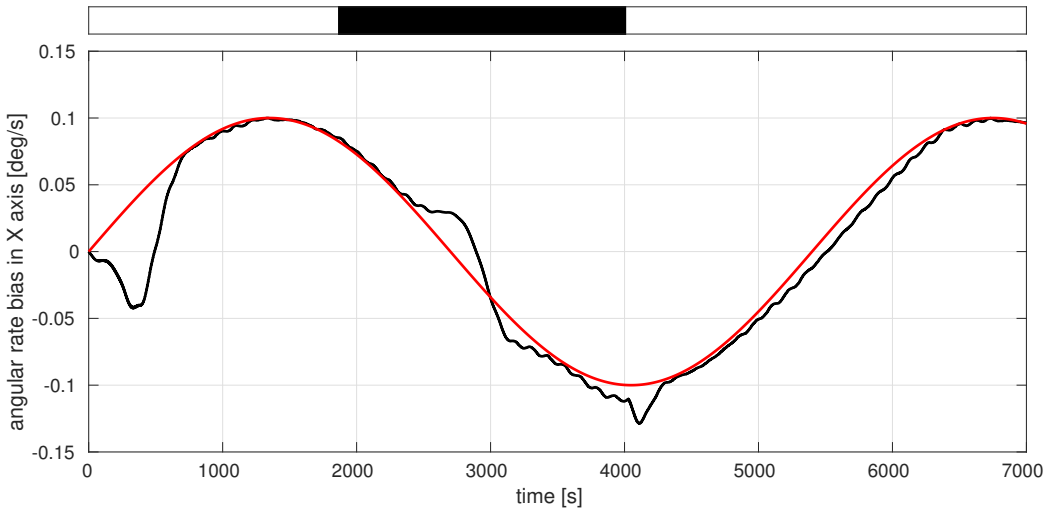

Figure 6.33: The X coordinate of the mean angular rate sensor bias estimate for a multi-rate sensor sampling case (black line) compared with the true bias (red line). Horizontal axis represents the simulation time. In the presented case evaluation of the algorithm occurs once every simulated second. When comparing bias estimation performance with the case of sensors working at the same rate (see Fig. 6.29) a slightly worse performance can be observed. Note, that the larger error in the first 1000 units is mainly due to the substantially less precise initial estimate provided to the algorithm (initial error of 180°).

Chapter 7

Conclusions

The following chapter contains the research conclusions listed in Sec. 7.1 and compared with the thesis proposed at the beginning of this work in Sec. 1.2. Summary of the contributions brought to the research discipline is presented in Sec. 7.3. At the end, some pointers on future directions of work in the presented subject are outlined in Sec. 7.3.

7.1 Research conclusions

Research thesis outlined in Sec. 1.2 have been investigated. Tab. 7.1 summarises the effects of this effort. All the thesis have been proven and the number of research contributions to the domain of the spacecraft attitude determination were made. Sec. 5.1 describes a structure of the proposed attitude estimator. It is based on a solution fo the Wahba problem converted to the quaternion representation. A case study culminating in a set of Monte-Carlo experiments is presented in Sec. 6.4. At the same time it proves that the observer is able to correctly track the attitude and gyroscope bias, and that the sensor quality (mainly the Star tracker field of view) proposed by the Lithuanica Sat-2 team may not be sufficient to fulfil the mission requirements. To verify if the estimator copes with the unavailability of the measurement data on par with other solutions known from the literature a comparison Monte-Carlo study is performed in Sec. 6.4.2. Results are that the new SDQAE observer provides the best precision of all the tested solutions. Of course, this does not prove that it is the best estimator, as number of possibilities, especially in the Kalman filtering realm is large. However, it certainly is worthwhile to consider it for practical applications. At the same time a better Sun sensor configuration with all-around field of view is tested and it seems to fulfil the mission requirements if the satellite is illuminated. On the other hand, performance of all the estimators during the eclipse is many times worse than the required one, putting the feasibility of precise attitude estimation with this sensor suite in question for that particular case. Finally, an interesting result is achieved in Sec. 6.4.3 suggesting that sampling sensor at different rates may not lead to a significant performance drop. This capability of the proposed observer may be a great tool for balancing power requirements and precision of the attitude estimation system. More complicated sensors, such as CMOS Sun sensors could be sampled at much

lower rate, making the overall system more efficient.

Table 7.1: Research thesis summary

Research thesis	Research result	Details
It is possible to develop an attitude estimator dedicated for nanosatellites, which is able to function with small number of relatively simple attitude sensors without the knowledge of torques acting on the satellite	PROVEN	Sec. 5.1, Sec. 6.4
It is possible to develop a single attitude estimator that is able to dynamically cope with periodic unavailability of the measurements from one of the absolute attitude sensors	PROVEN	Sec. 6.4, Sec. 6.4.2
It is possible to achieve comparable levels of precision of attitude estimation with a systems that samples each of the sensors at different rate to use the more energy consuming sensors less frequently	PROVEN	Sec. 6.4.3

7.2 Summary of contributions

This work not only contains survey of existing solutions for attitude estimation, but also includes modest attempt of creating a unique attitude estimator. Solution is unique because it neither utilizes well explored Kalman filtering realm, nor incorporate classical attitude matrix formulation of Wahba problem. Instead, Wahba problem was translated into quaternion attitude representation and optimization theory was iteratively used in a way that allows sensor noise rejection and gyroscope bias estimation. Computer simulation results suggest that this approach is not only capable of relatively precise attitude estimation, but also proves to be relatively easy in implementation, computationally inexpensive and resilient against periodical sensor unavailability. Interest of researchers from Vilnius university, planning to use the algorithm in Lithuanica SAT-2 mission as one of two redundant attitude estimation algorithms, suggests that this solution has high applicability potential for small satellite platforms.

Existing solutions for the satellite attitude estimation where not only classified in Sec. 3.3 but also compared to each other in Sec. 6.4.2. Results of this comparison show that, assuming no knowledge on satellite inertia and attitude torques, none of the single-frame attitude estimators approached the level of precision of SDQAE. Also, with the exception ofEKF, those estimators were unable to utilize MEMS angular rate sensor to sustain the attitude estimation capability during the periods when the Sun sensors were inoperable due to the eclipse condition. Only the simple EKF filter described in appendix Ch. B proved to compete with SDQAE but still performed slightly worse while satellite was in sunlight and much worse during the eclipse. Author is aware that more complex EKF taking into account the model of dynamics, or using different structure of the observer in

the eclipse could yield better results, but a significant effort of developing such a solution lied beyond the scope of this thesis.

In Sec. 6.4.3 an experiment is presented in which a multi-rate scheme of sensor sampling used in SDQAE estimator is used. Each of the three analysed sensor (the angular rate sensor, magnetometer and the Sun sensor) are sampled at different sample times. It turns out that negative effect on precision of decreasing sampling time on some sensors can be negligible, proving that it is justifiable to operate some of them with decreased rate to conserve the energy. Another contribution to the research community is development by

Table 7.2: Summary of contributions

Contibution	Summary	Reference
SDQAE attitude observer	Development of a new attitude determination algorithm based on a steepest descent optimization of Wahba's objective function in quaternion space.	Sec. 5.1
Lithuanica SAT-2	Concept of a practical application of the SDQAE attitude estimator, planning the experiments.	Sec. 6.4.1, Sec. 7.3
Comparison of selected attitude estimators	Comparison of selected attitude estimators in realistic nanosatellite scenario, including only commonly used sensors, taking into account issues such as angle between measured vectors, gaps in the measurements stream, etc.	Sec. 3.3, Sec. 6.4.2
Multi-rate measurement scheme	Proposition and Monte-Carlo study proving the possible application of the algorithm with the sensors working at different rates to allow for improved energy efficiency.	Sec. 6.4.3
Aerospace Blockset for Xcos	Development of the open source aerospace simulation library in the Scilab/Xcos environment.	Sec. 6.1

the author of unique Aerospace Blockset for Xcos [87] software package which is a free, open and extendible software tool for aerospace systems simulations. It is a part of the open source Scilab/Xcos simulation environment. It was envisioned as a tool that fills the gap between the free, single-purpose aerospace software (e.g. Space Trajectory Analysis, etc.), and the very expensive professional tools (e.g. AGI-STK, Matalb/Simulink). The module is a set of 49 functional Xcos blocks (as for version 3.0) encapsulating many of the CelestLab functionalities into Xcos diagrammatic programming tool. All of the developed functional blocks can be connected indicating data flow, and in that way solutions to complex aerospace problems can be found. Additionally, when user is required to input manually numerical parameters it is possible in many cases to do that using a dedicated

dialogue box. Explanations of the parameters unit, meaning and allowable range further decreases the risk of error. Blockset makes it possible to perform complicated simulations. Its diverse functionalities include but is not limited to: propagating orbits of celestial bodies and artificial satellites, conversions of reference and time frames, environmental models (Earth magnetic field, solar pressure, atmospheric drag, etc...), ground station visibility, unit conversions, attitude dynamics and quaternion algebra. As of November 2016 this package was downloaded over 25 thousand times. It is hard to estimate how many researchers and students worldwide uses the package as the direct feedback from users is nearly non-existent. However, it has been mentioned in some scientific papers [77], [78].

All of the significant contributions present in this thesis are outlined in Tab. 7.2.

7.3 Future research

Future work on the SDQAE will focus on preparing the practical implementation for the Lithuanica SAT-2 satellite. Satellite onboard software must include many additional safeguards and features in comparison with the models used on the ground for scientific purposes. Significant effort has already been undertaken to design such an implementation. Many of the additional features focus on diagnostic capabilities and are not interfering with the algorithm itself. In this section only the necessary algorithm redesigns will be briefly mentioned.

Research outlined in this thesis assumed that the satellite has three sensors: rate gyroscope, magnetometer and Sun sensor. Only two cases were analysed. First, when the satellite was in sunlight and all three measurements were available, and second when satellite was in the eclipse and Sun sensor did not produce any useful data. In those two cases the same sensor weights were used. To allow for wide range of tuning capabilities after the satellite is launched into orbit total number of eight possibilities should be analysed, where some sensors are active and some are not. It should be possible to configure the weights and algorithm gains differently for each of those cases in case some failure modes require special handling. Also, despite the fact that using the same sensor weights for correction step and for the bias estimation it should be possible to configure them separately.

Let us assume that c_m and c_s weights are used for weighting the algorithm correction term and b_m together with b_s for the bias estimation term. Notice that gains K and K_ω are not necessary if we remove the $c_m + c_s = 1$ constraint. Additionally, it should be possible to disable the gyroscope bias estimation altogether in cases when there is not enough information available. Theoretically with the right weight values the bias estimation term could also be used to coarsely estimate the angular rate in case of the gyroscope sensor. Therefore, a c_w parameter is introduced which can be used to control this behaviour (1 – bias estimation, 0 – term disabled, -1 – angular rate estimation). Summary of possible configuration options all the available sensor modes is outlined in Tab. 7.3.

This scheme allows for the satellite to use predefined tuning parameters for each of the

Table 7.3: Description of tuning parameters in different input configurations

Mode	SS	Mag	Gyro	c_m	c_m	b_s	b_m	c_ω	Description
1	on	on	on	c_{m1}	c_{m1}	b_{s1}	b_{m1}	1	nominal
2	off	on	on	0	c_{m2}	0	b_{m2}	1	eclipse or failed SS
3	on	off	on	c_{m3}	0	b_{s3}	0	1	failed mag
4	on	on	off	c_{m4}	c_{m4}	b_{s4}	b_{m4}	-1	failed gyro
5	off	off	ok	0	0	0	0	0	failed mag + eclipse
6	off	on	off	0	c_{m6}	0	b_{m6}	0	failed gyro + eclipse
7	on	off	off	c_{m7}	0	b_{s7}	0	0	failed gyro and mag
8	off	off	off	0	0	0	0	0	all sensor unavailable

possible sensor availability states. Example of the mode switching can be seen in Fig. 7.1 In this example satellite initially uses all the sensors to track the attitude and gyroscope

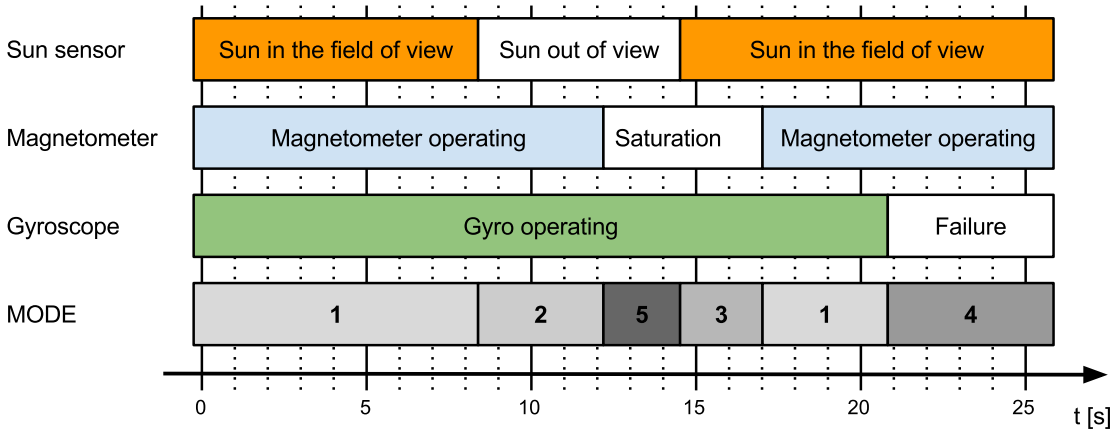

Figure 7.1: Example of autonomous sensing mode switching

bias, goes into eclipse and experiences short magnetometer malfunction that causes it to go into mode when attitude is propagated solely based on the gyroscope reading. In this mode estimation of the bias becomes impossible due to the lack of usable data. After a short period of full sensor availability, the gyroscope fails and the weights can be adjusted more aggressively to provide attitude determination with limited precision.

All the currently considered interfaces and configuration parameters are shown in Fig. 7.2

Another important field of further study is utilizing sensor measurements made on-board the Lithuanica SAT-2 for analysing the algorithm performance under the realistic conditions of space flight.

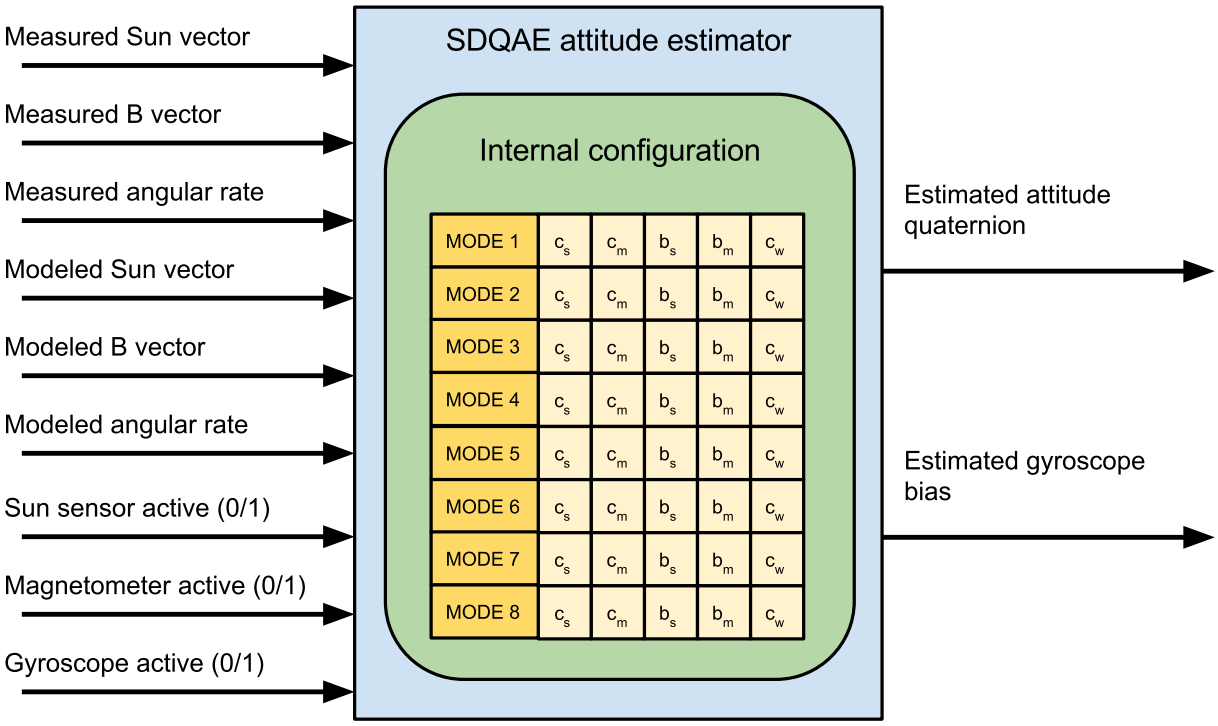

Figure 7.2: SDQAE algorithm interfaces

Bibliography

[1] Alfriend, K. Partially filled viscous ring nutation damper. *Journal of Spacecraft and Rockets 11*, 7 (1974).

[2] Arbinger, C., and Lübke-Ossenbeck, B. *Handbook of Space Technology, Attitude Control*. Aerospace Series. Wiley, 2009, ch. 4.5, pp. 351–357.

[3] Bar-Itzhack, I. Y. REQUEST – a recursive QUEST algorithm for sequential attitude determination. *Journal of Guidance, Control, and Dynamics 19*, 5 (1996), 1034–1038.

[4] Bar-Itzhack, I. Y., and Oshman, Y. Attitude determination from vector observations: Quaternion estimation. *Aerospace and Electronic Systems, IEEE Transactions on*, 1 (1985), 128–136.

[5] Bar-Itzhack, I. Y., and Reiner, J. Recursive attitude determination from vector observations: DCM identification. *Journal of Guidance, Control, and Dynamics 7*, 1 (1984), 51–65.

[6] Barnhart, D. J., Vladimirowa, T., Baker, A. M., and Sweeting, M. N. A low–cost femtosatellite to enable distributed space missions. *Acta Astronautica 64* (March 2009).

[7] Black, H. D. A passive system for determining the attitude of a satellite. *AIAA Journal 2*, 7 (1964), 1350–1351.

[8] Bonnet, S., Bassompierre, C., Godin, C., Lesecq, S., and Barraud, A. Calibration methods for inertial and magnetic sensors. *Sensors and Actuators A: Physical 156*, 2 (2009), 302–311.

[9] Brock, J. E. Optimal matrices describing linear systems. *AIAA Journal 6*, 7 (July 1968), 1292–1296.

[10] Byrski, W. *Obserwacja i sterowanie w systemach dynamicznych [in polish]*. Komitet Automatyki i Robotyki Polskiej Akademii Nauk, 2007.

[11] Campbell, S. L., Chancelier, J.-P., and Nikoukhah, R. *Modeling and Simulation in Scilab/Scicos*. Springer New York, 2006.

[12] Carlos, R., Longo, O., and Rickman, S. L. Method for the calculation of spacecraft umbra and penumbra shadow terminator points. Tech. rep., NASA, 1995.

[13] Cavallo, A., De Maria, G., Ferrera, F., and Nistri, P. A sliding manifold approach to satellite attitude control. In *12th World Congress IFAC* (1993).

[14] Choukroun, D. *Novel Methods for Attitude Determination Using Vector Observations*. PhD thesis, The Technion, 2003.

[15] Choukroun, D., and Bar-Itzhack, I. Y. Optimal – REQUEST algorithm for attitude determination. *Journal of Guidance, Control, and Dynamics 27*, 3 (2004), 418–425.

[16] Choukroun, D., and Bar-Itzhack, I. Y. Novel quaternion Kalman filter. *Aerospace and Electronic Systems, IEEE Transactions on 42*, 1 (2006), 174–190.

[17] Crassidis, J. L., and Markiey, F. Attitude estimation using modified rodrigues parameters. *Journal of Guidance, Control, and Dynamics* (1996).

[18] Curtis, D. H. *Orbital Mechanics for Engineering Students*, 2 ed. Elsavier, Daytona Beach FL, USA, 2009.

[19] Darrin, A., and O'Leary, B. L. *Handbook of Space Engineering, Archaeology, and Heritage*. CRC Press, 2010.

[20] Davis, J. Mathematical modeling of Earth's magnetic field. Tech. rep., Virginia Tech, May 2004.

[21] Farrahi, A., and Sanz-Andrés, A. Efficiency of hysteresis rods in small spacecraft attitude stabilization. *The Scientific World Journal 2013* (2013).

[22] Farrell, J. L. Attitude determination by Kalman filtering. *Automatica 6*, 3 (1970), 419–430.

[23] Gavigan, P. *Design, Test, Calibration and Qualification of Satellite Sun Sensors, Power Systems and Supporting Software Development*. PhD thesis, University of Toronto, 2011.

[24] Gerhardt, D. T., and Palo, S. E. Passive magnetic attitude control for CubeSat spacecraft. In *24th Annual AIAA/USU Conference on Small Satellites* (2010).

[25] Giesselmann, J. Development of an active magnetic attitude determination and control system for picosatellites on highly inclined circular low Earth orbits. Master's thesis, RMIT University, June 2006.

[26] Gill, E., Sundaramoorthy, P., Bouwmeester, J., Zandbergen, B., and Reinhard, R. Formation flying within a constellation of nano-satellites: The QB50 mission. *Acta Astronautica 82*, 1 (2013), 110–117.

[27] Gomez, C. *Engineering and Scientific Computing with Scilab*. Springer Science & Business Media, 2012.

[28] Hughes, P. C. *Spacecraft Attitude Dynamics*. John Wiley and Sons, New York, 1986.

[29] Idan, M. Estimation of Rodrigues parameters from vector observations. *Aerospace and Electronic Systems, IEEE Transactions on 32*, 2 (1996), 578–586.

[30] Keat, J. Analysis of least-squares attitude determination routine DOAOP. Tech. Rep. CSC/TM-77/6034, Computer Sciences Corporation, February 1977.

[31] Kim, K. Analysis of hysteresis for attitude control of a microsatellite. Tech. rep., San Jose State University.

[32] Kronhaus, I., Schilling, K., Jayakumar, S., and Kramer, A. Design of the UWE-4 picosatellite orbit control system using vacuum-arc-thrusters. In 33^{rd} *International Electric Propulsion Conference* (2013).

[33] Kulu, E. Nanosatellite database by Eric. `http://www.nanosats.eu/`. Accessed: 2016-29-12.

[34] Lagarias, J. C., Reeds, J. A., Wright, M. H., and Wright, P. E. Convergence properties of the Nelder–Mead simplex method in low dimensions. *SIAM Journal on optimization 9*, 1 (1998), 112–147.

[35] Lam, T. Y. Hamilton's quaternions. Tech. rep., University of California, Berkeley, USA, 2002.

[36] Lee, S., Hutputanasin, A., Toorian, A., Lan, W., and Munakata, R. *CubeSat Design Specification*, rev. 12 ed. Cal Poly, San Luis Obispo, August 2009.

[37] Lefferts, E. J., Markley, F. L., and Shuster, M. D. Kalman filtering for spacecraft attitude estimation. *Journal of Guidance, Control, and Dynamics 5*, 5 (1982), 417–429.

[38] Lerner, G. M. *Spacecraft Attitude Determination and Control*. Springer, 1978, ch. Three-Axis Attitude Determination, pp. 420–429.

[39] Link, F. *Eclipse Phenomena in Astronomy*. Springer, 1969.

[40] Lyle, R., and Stabekis, P. Spacecraft aerodynamic torques. Tech. rep., NASA, 1971.

[41] Madgwick, S. O., Harrison, A. J., and Vaidyanathan, R. Estimation of IMU and MARG orientation using a gradient descent algorithm. In *Rehabilitation Robotics (ICORR), 2011 IEEE International Conference on* (2011), IEEE, pp. 1–7.

[42] Mahony, R., Hamel, T., and Pflimlin, J. M. Nonlinear complementary filters on the special orthogonal group. *Automatic Control, IEEE Transactions on 53*, 5 (2008), 1203 –1218.

[43] Marchese, L. E., Thomas, P., Pope, T. D., Asselin, D., and Jerominek, H. A compact lightweight Earth horizon sensor using an uncooled infrared bolometer. In *Photonics North 2007* (2007), J. Armitage, Ed., vol. 6796.

[44] Markley, F. L. *Spacecraft Attitude Determination and Control*. Springer, 1978, ch. Three Axis Attitude Determination Methods, pp. 410–420.

[45] Markley, F. L. Attitude determination using vector observations and the singular value decomposition. *The Journal of the Astronautical Sciences 36*, 3 (July-Sept. 1988), 245–258.

[46] Markley, F. L. Attitude determination using vector observations: A fast optimal matrix algorithm. *Journal of the Astronautical Sciences 41*, 2 (1993), 261–280.

[47] Markley, F. L. Attitude error representations for Kalman filtering. *Journal of guidance, control, and dynamics 26*, 2 (2003), 311–317.

[48] Markley, F. L., and Bar-Itzhack, I. Y. Unconstrained optimal transformation matrix. *IEEE Transactions on Aerospace and Electronic Systems 34*, 1 (January 1998), 338–340.

[49] Markley, F. L., and Mortari, D. How to estimate attitude from vector observations. In *Proceedings of the AAS/AIAA Astrodynamics Specialist Conference* (1999), vol. 103, pp. 1979–1996.

[50] Markley, F. L., and Mortari, D. Quaternion attitude estimation using vector observations. *Journal of the Astronautical Sciences 48*, 2 (2000), 359–380.

[51] Meeus, J. H. *Astronomical Algorithms*, 2 ed. Willmann-Bell, Incorporated, Richmond VA, USA, 1998.

[52] Mills, S. A., and Smith, R. E. Models of Earth's atmosphere. Tech. rep., NASA, 1973.

[53] Montenbruck, O., and Gill, E. *Satellite Orbits – Models, Methods, Applications*. Springer, Berlin, 2000.

[54] MOOG Bradfort. *Coarse Sun Sensor*, 2014.

[55] Mortari, D. A closed-form solution to the Wahba problem. *Journal of the Astronautical Sciences 45*, 2 (April-June 1997), 195–204.

[56] Mortari, D. ESOQ2 Single-point algorithm for fast optimal spacecraft attitude determination. *Advances in the Astronautical Sciences 95* (1997), 817–826.

[57] Mortari, D. Second estimator of the optimal quaternion. *Journal of Guidance, Control, and Dynamics 23*, 5 (September-October 2000), 885–888.

[58] Murrell, J. W. Precision Attitude Determination for Multimission Spacecraft. *AIAA paper 78* (Aug 1978), 1248.

[59] Musser, K. L., and Ward, L. E. Autonomous spacecraft attitude control using magnetic torquing only. In *Flight Mechanics Estmation Theory Symposium* (1989).

[60] Ousaloo, H. S. Hysteresis nutation damper for spin satellite. *The Open Aerospace Engineering Journal 6* (2013), 1.

[61] Palais, B., and Palais, R. Euler's Fixed Point Theorem: The Axis of a Rotation. *Journal of Fixed Point Theory and Applications 2* (2007), 215–220.

[62] Psiaki, M. L. Attitude-determination filtering via extended quaternion estimation. *Journal of Guidance, Control, and Dynamics 23*, 2 (2000), 206–214.

[63] Psiaki, M. L. Backward-smoothing extended Kalman filter. *Journal of guidance, control, and dynamics 28*, 5 (2005), 885–894.

[64] Quarteroni, A., and Saleri, F. *Scientific Computing with MATLAB*. Springer Science & Business Media, 2012.

[65] Reyhanoglu, M. Modeling and control of space vehicles with fuel slosh dynamics. Tech. rep., Emry-Riddle Aeronautical University, 2009.

[66] Shilov, G. E. *Linear Algebra*. Dover Publications, 1977.

[67] Shuster, M. D. Maximum likelyhood estimation of spacecraft attitude. *Journal of the Astronautical Sciences 37*, 1 (January-March 1989), 79–88.

[68] Shuster, M. D. A simple Kalman filter and smoother for spacecraft attitude. *Journal of the Astronautical Sciences 37*, 1 (1989), 89–106.

[69] Shuster, M. D. A survey of attitude representations. *Navigation 8*, 9 (1993).

[70] Shuster, M. D., and Oh, S. D. Three-axis attitude determination from vector observations. *Journal of Guidance, Control, and Dynamics 4*, 1 (1981), 70–77.

[71] Steyn, W. H. Comparison of low-Earth orbiting satellite orbiting controllers submitted to controllcontrol constraints. *Journal of Guidance, Control, and Dynamics 17*, 4 (1994), 795–804.

[72] Stickler, A. C., and Alfriend, K. Elementary magnetic attitude control system. *Journal of Spacecraft and Rockets 13*, 5 (1976), 282–287.

[73] Storch, J. Aerodynamic disturbances on spacecraft in free-molecular flow. Tech. rep., DTIC Document, 2002.

[74] Stuelpnagel, J. On the parametrization of the three-dimensional rotation group. *SIAM review 6*, 4 (1964), 422–430.

[75] Trusov, A. A. Overview of MEMS gyroscopes: History, principles of operations, types of measurements. Tech. rep., MicroSystems Laboratory, Mechanical and Aerospace Engineering University of California, 2011.

[76] Tuma, J. J. *Dynamics*. Quantum Publishers, New York, 1974.

[77] Vogeltanz, T. Free software for the modelling and simulation of a mini-UAV. *Mathematics and computers in science and industry* (2014), 13–15.

[78] Vogeltanz, T. A survey of free software for the design, analysis, modelling, and simulation of an unmanned aerial vehicle. *Archives of Computational Methods in Engineering* (2015), 1–66.

[79] Wahba, G. A least-squares estimate of satellite attitude. *SIAM Review 7*, 3 (July 1965), 409.

[80] Weinberg, H. Gyro mechanical performance: The most important parameter. Tech. rep., Analog Devices, Inc, 2011.

[81] Weisstein, E. Euler's rotation theorem. `http://mathworld.wolfram.com/EulersRotationTheorem.html`. Accessed: 2016-12-29.

[82] Wertz, J. *Spacecraft Attitude Determination and Control*. Springer, The Netherlands, 1984.

[83] Wisniewski, R. Three axis attitude control – linear time varying approach. In *IFAC Workshop onControl Applications of Optimization* (1995).

[84] Wiśniewski, R. *Satellite Attitude Control Using Only Electromagnetic Actuation*. PhD thesis, Aalborg University, Fredrik Bajers Vej 7, DK-9220 Aalborg Ø, Denmark., December 1996.

[85] Zagorski, P., Dziwinski, T., and Tutaj, A. Verification procedures and hybrid simulation environment for nano- and picosatellites attitude observers. In *6th European Conference For Aerospace Sciences* (2015).

[86] Zagórski, P. Method for creating Earth's magnetic field model optimized for satellite attitude observer [in polish]. *Prace Instytutu Elektrotechniki* (2012).

[87] Zagórski, P., and Grega, W. Aerospace Blockset for Xcos - Open source tool for aerospace systems numerical computation and simulation. *Measurement Automation Monitoring 61*, 12 (December 2015), 551–554.

[88] CelestLab module webpage. `https://atoms.scilab.org/toolboxes/celestlab`. Accessed: 2016-12-29.

[89] GG1320AN digital laser gyro. Tech. rep., Honeywell Aerospace.

[90] Matlab product webpage. `http://www.mathworks.com/products/matlab/`. Accessed: 2016-12-29.

[91] Nano star trackers. Tech. rep., Blue Canyon Technologies.

[92] Scilab modules repository. `https://atoms.scilab.org/`. Accessed: 2016-12-29.

[93] Scilab official website. `http://www.scilab.org/`. Accessed; 2016-29-12.

[94] Space environment. Tech. Rep. ECSS-E-10-04A, ESA-ESTEC, Noordwijk, The Netherlands, 2000.

[95] STD 15 Earth sensor. Tech. rep., EADS SODERN, 2004.

[96] STD 16 Earth sensor. Tech. rep., EADS SODERN, 2004.

[97] 3-axis digital compass IC HMC5883L. Tech. rep., Honeywell, 2010.

[98] Space GPS receiver — SGR-10. Tech. rep., Surrey Satellite Technology Ltd., 2013.

[99] Xtrinsic MAG3110 three-axis, digital magnetometer. Tech. rep., Freescale Semiconductor, 2013.

[100] 2-axis DMC Sun sensor. Tech. rep., Surrey Satellite Technology Ltd., 2014.

[101] Space GPS receiver — SGR-05P. Tech. rep., Surrey Satellite Technology Ltd., 2014.

[102] Allan variance: Noise analysis for gyroscopes. Tech. Rep. AN5087, Freescale Semiconductor, 2015. Rev. 0, 2/2015.

[103] Fiber optic gyro. Tech. rep., Saab AB, Avionics Systems, 2015.

[104] IRES Infrared Earth sensor. Tech. rep., Selex ES, 2015.

[105] Lithium-niobate fiber optic gyroscope (FOG). Tech. Rep. EMP-1, EMCORE, 2016.

Appendices

Appendix A

Notation conventions

Vectors, quaternions and scalars

Absolute value

Absolute value of a scalar value s will be denoted as:

$$|s| = \begin{cases} s, & \text{if } s \geq 0 \\ -s, & \text{if } s < 0 \end{cases}.$$

Vector norm and normalization

Most common notation of generalized norm of vector $\boldsymbol{v}$ is $\|\boldsymbol{v}\|$. In order to indicate L^1, L^2 and L^∞ norm following convention will be used:

$$L^1(\boldsymbol{v}) = \|\boldsymbol{v}\|_1 = \sum_{i=1}^{n} |v_n|,$$

$$L^2(\boldsymbol{v}) = \|\boldsymbol{v}\| = \|\boldsymbol{v}\|_2 = \sum_{i=1}^{n} \sqrt{|v_n|^2},$$

$$L^\infty(\boldsymbol{v}) = \|\boldsymbol{v}\|_\infty = \max_i |v_n|.$$

To simplify the notation of vector normalization a $\nparallel \cdot \nparallel$ symbol will be used as in the following example:

$$\nparallel \boldsymbol{v} \nparallel = \frac{\boldsymbol{v}}{\|\boldsymbol{v}\|}$$

Vector multiplication

Scalar product of two vectors $\boldsymbol{v}$ and $\boldsymbol{w}$ will be denoted as

$$\boldsymbol{v} \cdot \boldsymbol{w}$$

or

$$\boldsymbol{v}^\top \boldsymbol{w}.$$

On the other hand a vector cross product will be indicated as

$$\boldsymbol{v} \times \boldsymbol{w}.$$

Quaternion norm and normalization

Quaternions will be denoted as $\overline{q}$. Norm of a quaternion is defined similarly to the L^2 vector norm with

$$L^2(\overline{q}) = \|\overline{q}\| = \|\overline{q}\|_2 = \sum_{i=1}^{n} \sqrt{|q_n|^2}.$$

The same symbol $\nmid \cdot \nmid$ used to indicate vector normalization will be used here as well:

$$\nmid \overline{q} \nmid = \frac{\overline{q}}{\|\overline{q}\|}$$

Quaternion (Hamilton) product

Hamilton product of the two quaternions $\overline{q}$ and $\overline{p}$ will be indicated with $\otimes$ sign and calculated with

$$\overline{q} \otimes \overline{p} = (q_1 i + q_2 j + q_3 k + q_4)(p_1 i + p_2 j + p_3 k + p_4),$$

where q_n and p_n are the elements of the quaternions and i, j, k are the imaginary numbers. Interpretation of this product is explained in more detail in Sec. 2.4.3.

Matrices and algebra

Matrix names will be denoted by capital letters, and matrices themselves will be written in box brackets. For example:

$$A = \begin{bmatrix} a_{11} & a_{12} & a_{13} \\ a_{21} & a_{22} & a_{23} \\ a_{31} & a_{32} & a_{33} \end{bmatrix}.$$

In case it is necessary the size of a matrix will be given by subscript $A_{n\times m}$, where n — indicates number of rows, and m — number of columns. Determinant of a matrix will be denoted by det operator or indicated by straight brackets:

$$\det A = \det \begin{bmatrix} a_{11} & a_{12} & a_{13} \\ a_{21} & a_{22} & a_{23} \\ a_{31} & a_{32} & a_{33} \end{bmatrix} = \begin{vmatrix} a_{11} & a_{12} & a_{13} \\ a_{21} & a_{22} & a_{23} \\ a_{31} & a_{32} & a_{33} \end{vmatrix}.$$

Other useful matrix operators include: rank — matrix rank, tr — matrix trace, A^{-1} — matrix inversion, and $A^{\top}$ — matrix transposition.

Derivatives

Leibniz's notation is used for non-time derivatives, as in the following example (chain rule):

$$\frac{dy}{dx} = \frac{dy}{du} \cdot \frac{du}{dx}.$$

Higher derivatives, of n-th order, can be represented by:

$$\frac{d^n y}{dx^n}.$$

Whenever value of derivative in certain point a is needed it will be denoted as:

$$\frac{dy}{dx}|_{x=a}.$$

Time derivatives will be denoted with dots above the variable symbol, according to Newton's notation. For example:

$$\boldsymbol{x} = 3\dddot{\boldsymbol{x}} + 4\ddot{\boldsymbol{x}} - 3\dot{\boldsymbol{x}} - 1,$$

where $\boldsymbol{x}$ is a vector, and:

$$\dot{\boldsymbol{x}} = \frac{d\boldsymbol{x}}{dt},$$
$$\ddot{\boldsymbol{x}} = \frac{d\dot{\boldsymbol{x}}}{dt},$$
$$\dddot{\boldsymbol{x}} = \frac{d\ddot{\boldsymbol{x}}}{dt}.$$

To indicate value of the time derivative at a time t_b the following notation will be used:

$$\dot{\boldsymbol{x}}(t_b) = \boldsymbol{w}.$$

. .

Appendix B

Description of the simple EKF attitude filter

Filter description

A continuous-time EKF has been implemented with the state vector

$$\boldsymbol{x} = \begin{bmatrix} {}^{b}_{i}\overline{q} \\ {}^{b}\boldsymbol{\omega_B} \end{bmatrix}, \tag{B.1}$$

containing the orientation quaternion ${}^{b}_{i}\overline{q}$ and angular rate bias ${}^{b}\boldsymbol{\omega_B}$. System model consists of the orientation quaternion process model

$${}^{b}_{i}\dot{\overline{q}} = \frac{1}{2}{}^{b}_{i}\overline{q} \otimes ({}^{b}\overline{\boldsymbol{\omega}} - {}^{b}\overline{\boldsymbol{\omega}}_{\boldsymbol{B}}), \tag{B.2}$$

relying on the unbiased angular rate measurement (see 5.9). Notice that attitude dynamics is not modelled. One reason for it is that other estimators compared in section Sec. 6.4.2 also lack the knowledge of the attitude dynamics. Furthermore, no insight on satellite inertia tensor and lack of sophisticated models of disturbance torques are assumed. Due to the fact that the attitude is predicted only based on the angular rate measurement the gyro bias is included in the state vector. It is assumed that this bias changes very slowly, yielding

$${}^{b}\dot{\boldsymbol{\omega}}_{\boldsymbol{B}} \approx \begin{bmatrix} 0 \\ 0 \\ 0 \end{bmatrix}, \tag{B.3}$$

where ${}^{b}\boldsymbol{\omega_B}$ is a 3×1 vector, with no the additional zero at the beginning in comparison to ${}^{b}\overline{\boldsymbol{\omega}}_{\boldsymbol{B}}$. Together, this produces the prediction model

$$\dot{\boldsymbol{x}} = f(\boldsymbol{x}) + \boldsymbol{w}(t), \tag{B.4}$$

where $\boldsymbol{w}(t)$ is the process noise approximated with white gaussian noise of covariance matrix Q and

$$f(\boldsymbol{x}) = \begin{bmatrix} {}^{b}_{i}\dot{\overline{q}} \\ {}^{b}\dot{\boldsymbol{\omega}}_{\boldsymbol{B}} \end{bmatrix}. \tag{B.5}$$

State transition matrix F at step n can be represented as

$$F_n = J(f(\boldsymbol{x}), \boldsymbol{x}) = \frac{\partial f(\boldsymbol{x})}{\partial \boldsymbol{x}}|_{\hat{\boldsymbol{x}}_{n|n-1}}, \tag{B.6}$$

where $J(f, \boldsymbol{x})$ is the Jacobi matrix of f with regard to the variable $\boldsymbol{x}$.

$$G_n = J(f(\boldsymbol{x}), {}^b\boldsymbol{\omega}) = \frac{\partial f(\boldsymbol{x})}{\partial {}^b\boldsymbol{\omega}}|_{\hat{\boldsymbol{x}}_{n|n-1}}, \tag{B.7}$$

The measurement vector is defined as

$$\boldsymbol{z}_n = \begin{bmatrix} {}^b\boldsymbol{m}_n \\ {}^b\boldsymbol{s}_n \end{bmatrix}, \tag{B.8}$$

where ${}^b\boldsymbol{m}_n$ and ${}^b\boldsymbol{s}_n$ are the normalized measured values of the magnetic and Sun vectors at step n respectively. Sensor noise is approximated with white Gaussian noise of covariance matrix R. With that in mind the observation matrix can be calculated as

$$H_n = J(\boldsymbol{z}) = \frac{\partial \boldsymbol{z}}{\partial \boldsymbol{x}}|_{\hat{\boldsymbol{x}}_{n|n-1}}. \tag{B.9}$$

The time derivative of the process covariance matrix can be therefore represented as

$$\dot{P}_n = F_n P_{n|n-1} + P_{n|n-1} F_n^\top + G_n Q G_n^\top, \tag{B.10}$$

and the near-optimal Kalman gain as

$$K_n = P_n H_n^\top \left((H_n P_n H_n^\top) + R \right)^{-1}. \tag{B.11}$$

Then the covariance matrix can be updated at each step of the algorithm with

$$P_n = (I - K_n H_n) P_{n|n-1}. \tag{B.12}$$

A posteriori state can be estimated with

$$\hat{\boldsymbol{x}}_{n|n} = \hat{\boldsymbol{x}}_{n|n-1} + K_n(z_n - z_{est,n}), \tag{B.13}$$

where

$$z_{est,n} = \begin{bmatrix} {}^b_i\hat{q}^*({}^i\boldsymbol{m}_n){}^b_i\hat{q} \\ {}^b_i\hat{q}^*({}^i\boldsymbol{s}_n){}^b_i\hat{q} \end{bmatrix}, \tag{B.14}$$

Obviously, orientation quaternion normalization is performed at the end of each step.

Filter tuning

In order to function properly a sensor noise covariance matrix R and process noise covariance matrix Q need to be supplied to the EKF. The sensor noise matrix is assumed to be diagonal with variances equal to the experimentally measured variances for each axis of the magnetometer and sun sensor. This was done with simulation of the sensor models behaviour (see example in Fig. 6.26). The process noise covariance matrix was tuned with optimization over a set of Monte-Carlo experiments as shown in Fig. B.1

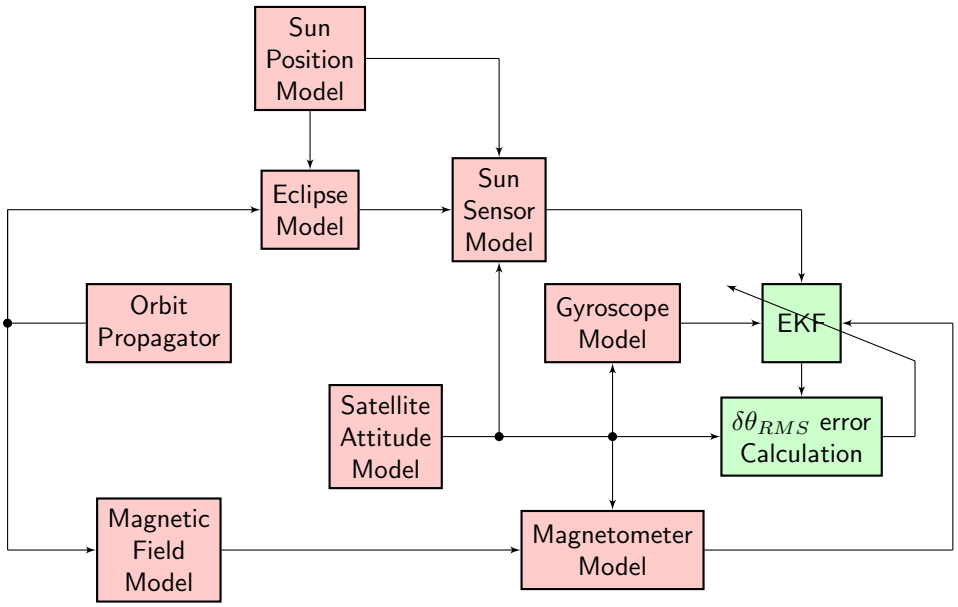

Figure B.1: The EKF observer tuning procedure setup

Appendix C

Quaternion formulation of Wahba problem

Let us examine the problem that is being solved in Sec. 5.1 formulated in terms of objective function

$$L({}^{b}_{i}\overline{q}) = \frac{1}{2}\sum_{n=1}^{n_{max}} c_n \left(f_n^{\top} f_n\right), \tag{C.1}$$

where:

$$f_n = {}^{\boldsymbol{b}}\overline{\boldsymbol{b}}_{\boldsymbol{n}} - {}^{b}_{i}\overline{q}^{*} \otimes {}^{\boldsymbol{i}}\overline{\boldsymbol{r}}_{\boldsymbol{n}} \otimes {}^{b}_{i}\overline{q}. \tag{C.2}$$

In this section it will be shown that C.1 it is in fact equivalent to the well known Wahba problem

$$L({}^{i}_{b}A) = \frac{1}{2}\sum_{n=1}^{n_{max}} c_n \left\| {}^{\boldsymbol{b}}\boldsymbol{b}_{\boldsymbol{n}} - {}^{i}_{b}A\,{}^{\boldsymbol{i}}\boldsymbol{r}_{\boldsymbol{n}} \right\|_2^2, \tag{C.3}$$

which uses an orientation matrix ${}^{i}_{b}A$ as the objective function argument.

It is easy to observe from (C.1) and (C.3) that if for each value of index n the equation

$$f_n^{\top} f_n = \left\| {}^{\boldsymbol{b}}\boldsymbol{b}_{\boldsymbol{n}} - {}^{i}_{b}A\,{}^{\boldsymbol{i}}\boldsymbol{r}_{\boldsymbol{n}} \right\|_2^2 \tag{C.4}$$

holds it follows that the two problems are equivalent. Let us then skip the index n for simplicity of notation and expand both sides of the resulting equation

$$f^{\top} f = \left\| {}^{\boldsymbol{b}}\boldsymbol{b} - {}^{i}_{b}A\,{}^{\boldsymbol{i}}\boldsymbol{r} \right\|_2^2. \tag{C.5}$$

Given a rotation quaternion it is fairly simple to calculate rotation matrix, following the (2.28):

$${}^{i}_{b}A = \begin{bmatrix} q_1^2 - q_2^2 - q_3^2 + q_4^2 & 2(q_1q_2 + q_3q_4) & 2(q_1q_3 - q_2q_4) \\ 2(q_1q_2 - q_3q_4) & -q_1^2 + q_2^2 - q_3^2 + q_4^2 & 2(q_2q_3 + q_1q_4) \\ 2(q_1q_3 + q_2q_4) & 2(q_2q_3 - q_1q_4) & -q_1^2 - q_2^2 + q_3^2 + q_4^2 \end{bmatrix}. \tag{C.6}$$

This way, the right side of C.5 can be expanded as

$$\begin{aligned}\left\|{}^{\boldsymbol{b}}\boldsymbol{b} - {}^{i}_{b}A\,{}^{\boldsymbol{i}}\boldsymbol{r}\right\|_2^2 = &\left(b_1 - r_1(q_1^2 - q_2^2 - q_3^2 + q_4^2) - 2r_2(q_1q_+q_3a_4) - 2r_3(q_1q_3 - q_2q_4)\right)^2 \\ &+ \left(b_2 - 2r_1(q_1q_2 - q_3q_4) - r_2(q_1^2 - q_2^2 + q_3^2 - q_4^2) - 2r_3(q_2q_3 + q_1q_4)\right)^2 \\ &+ \left(b_3 - 2r_1(q_1q_3 + q_2q_4) - 2r_2(q_2q_3 - q_1q_4) - r_3(-q_1^2 - q_2^2 + q_3^2 + q_4^2)\right)^2 .\end{aligned} \tag{C.7}$$

On the other hand quaternion f from the left side of C.5 can be expanded according to C.2. This is done remembering that the product of two quaternions $\overline{a}$ and $\overline{b}$ is calculated according to:

$$\overline{a} \otimes \overline{b} = \begin{bmatrix} a_1b_4 + a_2b_3 - a_3b_2 + a_4b_1 \\ -a_1b_3 - a_2b_4 + a_3b_1 + a_4b_2 \\ a_1b_2 - a_2b_1 + a_3b_4 + a_4b_3 \\ -a_1b_1 - a_2b_2 - a_3b_3 + a_4b_4 \end{bmatrix} . \tag{C.8}$$

After performing some algebraic operations f takes form

$$f = \begin{bmatrix} -r_1q_1^2 - 2r_2q_1q_2 - 2r_3q_1q_3 + r_1q_2^2 + 2r_3q_2q_4 + r_1q_3^2 - 2r_2q_3q_4 - r_1q_4^2 + b_1 \\ r_2q_1^2 - 2r_1q_1q_2 - 2r_3q_1q_4 - r_2q_2^2 - 2r_3q_2q_3 + r_2q_3^2 + 2r_1q_3q_4 - r_2q_4^2 + b_2 \\ r_3q_1^2 - 2r_1q_1q_3 + 2r_2q_1q_4 + r_3q_2^2 - 2r_2q_2q_3 - 2r_1q_2q_4 - r_3q_3^2 - r_3q_4^2 + b_3 \\ 0 \end{bmatrix} , \tag{C.9}$$

which can be further rearranged by factoring out the r_1, r_2 and r_3 terms. The resulting value is given by

$$f = \begin{bmatrix} b_1 - r_1(q_1^2 - q_2^2 - q_3^2 + q_4^2) - 2r_2(q_1q_+q_3a_4) - 2r_3(q_1q_3 - q_2q_4) \\ b_2 - 2r_1(q_1q_2 - q_3q_4) - r_2(q_1^2 - q_2^2 + q_3^2 - q_4^2) - 2r_3(q_2q_3 + q_1q_4) \\ b_3 - 2r_1(q_1q_3 + q_2q_4) - 2r_2(q_2q_3 - q_1q_4) - r_3(-q_1^2 - q_2^2 + q_3^2 + q_4^2 \\ 0 \end{bmatrix} , \tag{C.10}$$

The left side of C.5, namely $f^\top f$, is in fact a squared norm of quaternion given by C.10. Knowing that, it is sufficient to compare C.10 with C.7 and the equation C.5 holds. This means that quaternion that minimizes the objective function $L({}^{b}_{i}\overline{q})$ represents the same spacial orientation as the attitude matrix minimizing $L({}^{i}_{b}A)$, and that C.1 and C.3 are equivalent.